Doctoral Dissertation
Doctoral Program in Electrical, Electronics and Communications Engineering
(34th Cycle)

Innovative Model based on the Irradiance-Temperature Fitting of Equivalent Circuit Parameters for Commercial Photovoltaic Modules towards Accurate Power and Energy Prediction

By

Gabriele Malgaroli

******

Supervisors:
Prof. Filippo Spertino, Supervisor
Prof. Paolo Di Leo, Co-Supervisor

Doctoral Examination Committee:
Prof. Antonio D'Angola, Referee, Università degli studi della Basilicata
Prof. Gustavo Eduardo Nofuentes Garrido, Referee, University of Jaén
Prof. Alessandro Massi Pavan, Università degli Studi di Trieste
Prof. Enrico Pons, Politecnico di Torino
Prof. Angela Russo, Politecnico di Torino

Politecnico di Torino
October 2022

Declaration

I hereby declare that the contents and organization of this dissertation constitute my own original work and does not compromise in any way the rights of third parties, including those relating to the security of personal data.

Gabriele Malgaroli

October 2022

Acknowledgment

Abstract

The knowledge of the equivalent circuit parameters for a PhotoVoltaic (PV) generator permits to deeply study and simulate its performance under any weather condition. Many works in literature present procedures that determine these values starting from experimental data. The best compromise between simplicity and high accuracy is the equivalent circuit including five parameters: however, they are, generally, provided for specific weather conditions. In addition, these parameters are affected by the irradiance and the module temperature, but their dependence on these environmental quantities is studied for a few of these parameters only. Indeed, some works propose trends quantifying the parameters dependence on weather conditions, but they are qualitative, and some coefficients are not provided and, generally, unknown. Therefore, the generated PV energy in any weather condition cannot be predicted using the values of the equivalent circuit parameters. This work proposes an innovative methodology to determine the values of the equivalent circuit parameters using long term experimental campaigns. Moreover, their dependence on weather conditions was investigated, and this information was used to predict the generated energy by PV modules during the experimental campaign. The model was applied to seven commercial PV generators with different technology and rated power. In particular, two experimental campaigns were carried out for the modules under test: one at Politecnico di Torino (Turin, Italy) and one at the Universidad de Jaèn (Jaén, Spain). The effectiveness of the proposed model was investigated by comparing its energy prediction with the experimental energy (set as reference to quantify the deviations), and with the energy estimated by the most common model in literature (the Osterwald model).

Contents

List of Figures

List of Tables

Introduction

In recent years, the energy demand is rapidly increasing due to many factors like the urbanization process and the increase of human population. Despite fossil fuels still supply most of energy demand, one of the actual challenges is reducing pollution by improving the exploitation of Renewable Energy Sources (RES), and, thus, the self-sufficiency [1] and self-consumption [2] by RES-based systems. In this context, the most important and reliable technology is the PhotoVoltaic (PV) one thanks to its low installation, operation and maintenance costs [3], its absence of polluting emissions and its high availability [4]. Researchers in the PV sector are actually focusing on different lines of research, and one of the most important consists in the determination of the parameters in equivalent circuits[5], aiming to fully describe the performance of PV modules. The knowledge of these parameters is fundamental to deeply study and simulate the operation of a PV generator in any weather condition. Indeed, the current–voltage (*I-V*) curve of a PV generator can be traced starting from these quantities. Moreover, this information can be used in many applications such as mismatch studies in complex grid-connected PV systems [6,7] or the performance investigation of Maximum Power Point Trackers (MPPTs) under different weather conditions [8,9]. In this field, many models and algorithms are proposed in literature to extract the equivalent circuit parameters starting from experimental *I-V* curves. However, generally, they refer to specific weather conditions, and their dependence on irradiance and temperature is not investigated. Moreover, a few papers present some equations describing the dependence of each parameter on weather conditions, but some of their coefficients are unknown. Thus, this information cannot be used to predict the generated PV energy. This thesis work aims to propose an innovative model to predict PV energy starting from the knowledge of the equivalent circuit parameters [10]. This method relies on the extraction of the parameters from experiments under variable weather conditions. This information from this experimental campaign is used to estimate the unknow coefficients of equations taken from literature describing the dependence of each parameter on temperature and irradiance. Then, PV energy generated during the

experimental campaign is predicted using these optimized equations. Finally, the effectiveness of the method is investigated by comparing this result with the experimental data and with the same quantity evaluated by the most common model in literature to assess PV energy. In this work, the proposed model is applied to seven PV modules with different technologies and rated power (ranging between 100 W and 370 W).

This thesis is organized as follows: in chapter 1 and chapter 2, an overview of PV technology and of the optimization algorithms generally used in this field is presented. Chapter 3 contains the description of the measurement systems used to carry out two experimental campaigns (one in Italy and one in Spain), while in chapter 4, the detailed steps of the methodology are presented. Chapter 5 contains the most important information regarding the PV modules under test and the experimental campaigns. In chapter 6, the results of the analysis are presented, and chapter 7 contains the conclusions.

Chapter 1

Photovoltaic Technology

1.1 Solar irradiance

The solar irradiance G (measured in W/m^2) is the total power emitted by a radiating source reaching a unitary surface. The behaviour of the sun can be approximated to an ideal radiation emitter (black body), with a temperature $T \approx$ 5800 K. Outside the terrestrial atmosphere, the spectral distribution g_0 (expressed in W·m^2·µm^{-1}) of the emitted electromagnetic radiation extends from ultraviolet to infrared wavelengths, with a maximum value in the visible range at wavelength $\lambda \approx 0.5$ µm. In the terrestrial atmosphere, a part of the electromagnetic radiation is lost due to absorption/scattering/reflection phenomena by clouds, carbon dioxide, ozone, air components, etc. For a unitary surface, which is orthogonal to the sun beams, the "solar irradiance" is the integral of the spectral distribution of irradiance $g(\lambda)$ (W·m^2·nm^{-1}) on the whole wavelength range:

$$G = \int g(\lambda)d\lambda \approx 1367 \ W/m^2 \tag{1-1}$$

Figure 1-1 presents the spectral distribution of solar irradiance in two different conditions (extra-terrestrial and terrestrial atmosphere), as well as the radiation distribution for an ideal emitter (black body).
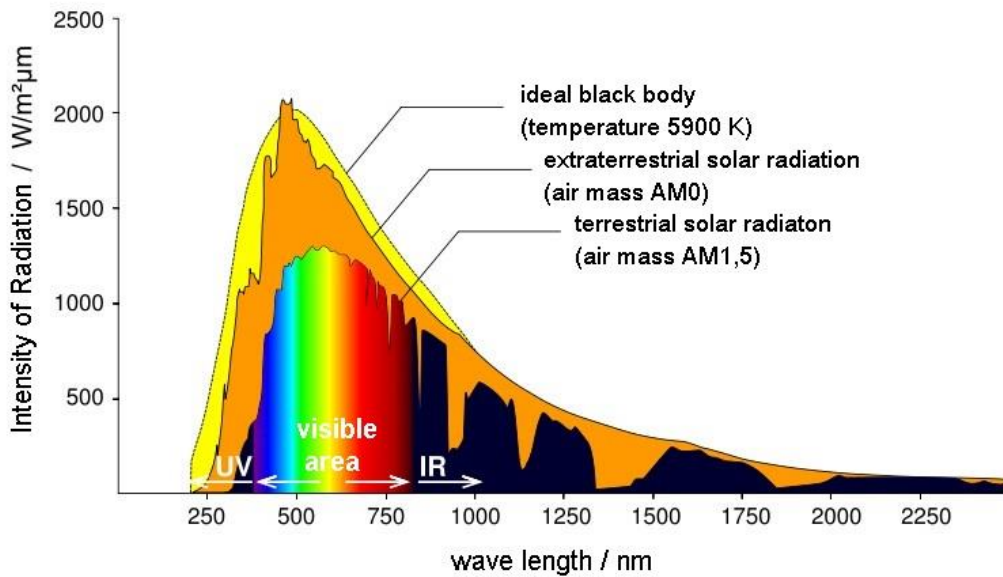
Figure 1-1: Spectral distribution for solar irradiance g(λ) in different conditions [11].

The radiation reaching the Earth surface without being scattered (and, thus, without loss of energy) is called *beam radiation* G_b (W/m²). On the contrary, the *diffuse* term G_d (W/m²) is the part of the electromagnetic radiation reaching the earth surface after being scattered, and this part of solar radiation seems distributed over the sky vault. The partitioning of solar radiation into beam and diffuse contributions is affected by weather conditions: indeed, during clear sky days, solar radiation consists of the beam term mainly (the ratio between diffuse and global radiation is < 20%), while the diffuse contribution is the highest in cloudy days. A third term, called *albedo* G_r (W/m²), is the solar radiation that reaches a receiver after being reflected by the Earth surface. The reflected radiation is quantified by the reflection coefficient ρ, being the ratio between the reflected contribution by a surface in any direction and the global radiation reaching that surface. This coefficient is a function of the light colour and the type of surface (e.g., reflection is maximum on clear surfaces, like snow).

The *global irradiance* (G_g) reaching a receiver consists of these three contributions and can be expressed in the following way:

$$G_g = G_b + G_d + G_r \tag{1-2}$$

Daily or yearly variations due to the apparent motion of the Sun, as well as variations of weather conditions (e.g., clouds) and atmospheric composition, may

affect the intensity of solar radiation reaching the Earth. Thus, the design of a photovoltaic system requires measurements of weather conditions close to the installation site. At ground level, the irradiance reaching a surface is affected by the altitude with respect to the sea level and the inclination of the receiver with respect to the horizontal.

The *Air Mass* (AM) quantifies the effect on irradiance due to transparent atmosphere: actually, the AM is higher or equal to 1 (its minimum value), being the relative length of the solar beams direct path through the atmosphere (Figure 1-2). The unitary AM corresponds to direct radiation coming from the Sun at the Zenith. In other conditions, AM is higher than 1, and it can be approximated to $1/\cos\theta_z$ by ignoring Earth's sphericity (where θ_z is the Zenith angle between the irradiance and the perpendicular to the ground). The efficiency of a solar cell is also affected by the spectrum of the incident radiation. In order to compare the performance between cells subject to different solar spectra, a standard spectrum was defined for the radiation outside the Earth's atmosphere and for the radiation incident on the Earth's surface. The standard spectrum at the Earth's surface is called AM1.5G, (where letter G stands for *global*, including beam and diffuse contributions) or AM1.5D (where letter D stands for *diffuse*, including diffuse contribution only). The standard AM1.5G spectrum has been normalized, and it corresponds to a clear sky day with irradiance $G = 1000$ W/m^2. The extra-atmospheric spectrum (named AM 0 because solar irradiance does not pass through the atmosphere) is important for applications of solar cells on satellites.
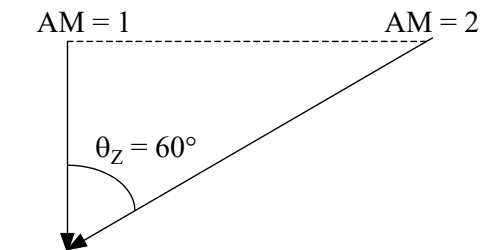
Figure 1-2: Geometrical scheme of air mass.

Figure 1-1 shows the spectrum of solar radiation in which the visible band *b1* ranges from 0.38 to 0.78 μm. The sensitivity of bandwidth depends on the cell type: *b2* refers to crystalline silicon cells (0.4 to 1.1 μm). Figure 1-3 shows in detail the spectral responses of the three most widespread technologies. It should be noted that the integral of the product $\int g(\lambda) \cdot S(\lambda) \cdot d\lambda$ is the *photo-generated current density* J_{ph} (A/m^2), which will be discussed in the next section.

The integral of the irradiance over a time interval is called *radiation* (*H*) measured in kWh/m². The daily radiation H_d (kWh/m²), the monthly radiation H_m (kWh/m²) and the yearly radiation H_y (kWh/m²) are significant for the design of PV systems.
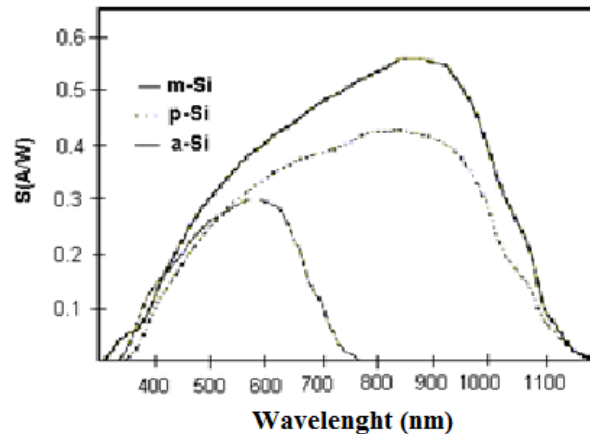
Figure 1-3: Spectral response S(λ) of solar cells in crystalline silicon (mono, poly) and amorphous silicon.

1.2 Solar cell: structure and operation

The "solar cells" or "PV cells" are the major element of PV generators. In case of terrestrial applications, solar cells are made of crystalline silicon ("c-Si", divided into monocrystalline, "m-Si", and polycrystalline, "p-Si") or thin films (amorphous Silicon, "a-Si", Copper Indium-Gallium Selenide, "CI-GS", or Cadmium Telluride, "CdTe").

Solar cells are semiconductor diodes with large section and their shape varies according to their typology: in fact, PV cells can be square (p-Si), pseudo-square or circular (m-Si), or rectangular (a-Si, CI-GS, CdTe). The diode is placed between two electrodes: the first one can be bulky and transparent to solar radiation (thin films), or it may have a grid shape in c-Si technology. On the contrary, the second electrode is on the rear of the cell and has a plate shape. The structure of a typical c-Si cell is shown in Figure 1-4. The thickness of solar cells ranges between ≈1 μm (thin films) and few hundreds of μm (150 – 100 μm for c-Si). The "P-N" junction theory describes the performance of PV cells in dark conditions. In case of typical c-Si, a diode consists of two substrates: a "N-type" layer (with high concentration of pentavalent impurities, such as Phosphorus) is deposited on a "P-type" layer (having high concentration of trivalent impurities, such as Boron). The "N-type"

substrate is shallow to let the solar irradiance pass through the junction area, which is subjected to an electric field. Its generation can be explained starting from the diffusion of mobile carriers in the junction area close to the P-N interface.
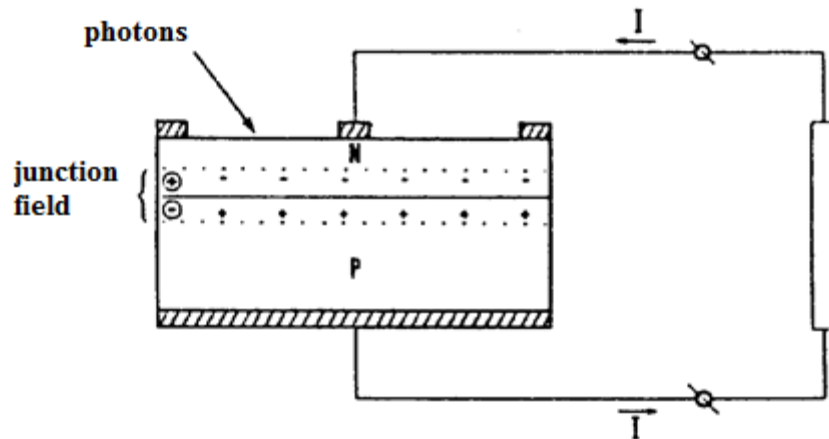
Figure 1-4: Structure of a polycrystalline "p-Si" solar cell.

In this region, the electrons diffuse from the N-type to the P-type layer: as a consequence, a distribution of positive charges occurs in the N region. Similarly, the holes diffuse from the P-type to the N-type layer, creating a distribution of negative charges in the P region. In this process, the carriers move from a region with higher concentration to a region with lower concentration. The interface between the two regions is called "depletion region" or "space-charge region". It does not contain mobile charges: positive charges are on the N side and negative charges are on the P side. This charge distribution creates a potential barrier (junction field) that opposes a further diffusion flow of electrons and holes. In open-circuit conditions, the junction field creates a current (drift current) that counterbalance the diffusion current. When an external voltage is applied to the P-N junction, the balance is perturbed. If a positive voltage is applied to the P region (forward bias), the junction field is reduced. In this condition, the drift current becomes negligible with respect to the diffusion current, which flows though the diode. On the contrary, if a negative voltage is applied to the P side (reverse bias), the junction field increases. In this case, a low current (the drift contribution) flows in the junction. This term is the reverse saturation current (I_0) and it is oriented by the junction field.

The junction acts as a rectifier and its current-voltage (*I-V*) characteristic curve can be described by the Shockley equation. The first term is the diffusion current,

while the second one is the drift current. Without any external voltage, the two contributions are balanced, and current does not flow in the junction.

$$I = I_0 \cdot e^{q \cdot V/n \cdot k_B \cdot T_c} - I_0 \tag{1-3}$$

where I_0 (A) is the saturation current, T_c is junction temperature (K), q is the electron charge ($1.6 \cdot 10^{-19}$ C), n is the quality factor of the junction and ranges between 1 and 2) for most of PV equivalent circuits, and k_B is Boltzmann constant ($1.38 \cdot 10^{-23}$ J/K). In this model, the "breakdown region", due to high negative voltage, is not considered.

According to the light wave-particle duality, the light has the characteristics of waves, as well as the characteristics of particles. The photovoltaic conversion of solar energy is explained considering the latter ones. Indeed, solar energy can be considered as a stream of particles (photons) that carry the following energy:

$$E_{ph}(\lambda) = hc/\lambda \tag{1-4}$$

where h is the Planck's constant ($6.63 \cdot 10^{-34}$ m$^2 \cdot$kg/s), c is the light speed ($3 \cdot 10^8$ m/s), and λ is the wavelength of solar radiation. As an example, during a clear sky day, the number of photons reaching in the time unit a 1 cm^2 surface on the Earth is about $4.4 \cdot 10^{17}$.

However, a fraction of the photons in the solar radiation participate to photovoltaic conversion. In particular, the photons having energy higher than the energy gap E_g (measured in eV) of the semiconductor material, i.e., the energy gap between its valence band and its conduction band, are converted by solar cells only. In such condition, the photon enters the semiconductor, being absorbed and promoting an electron from the valence band to the conduction band. In the absorption process, electron-hole pairs are generated after the electron promotion to the valence band. Since most of the photons involved in the absorption process have higher energy than E_g, this surplus energy is lost in the process. Indeed, most of the electron-hole pairs have surplus energy higher than E_g: in this condition, the electrons and the holes decay into a position close to their band borders. As a consequence, the surplus energy cannot be converted into electrical energy, being lost as heat.

The absolute value of the generated electric power can be estimated by a quantity named "photo-generated current" (I_{ph}). Actually, it is a stream of electrons

representing the light-induced electron motion through the forbidden band. This current is a "drift current" that opposes to diffusion, and it is oriented according to the junction field: in this case, electrons move towards the N region. Its value can be estimated in the following way by neglecting losses:

$$I_{ph} = qNA \qquad\qquad (1\text{-}5)$$

where N is the number of photons ($cm^{-2}s^{-1}$) the semiconductor in the time unit per unit surface, and A is the semiconductor surface reached by solar radiation.

The current density can be evaluated in the following way:

$$J_{ph} = {I_{ph}}/{A} = \int g(\lambda) \cdot S(\lambda) d\lambda \qquad\qquad (1\text{-}6)$$

In case of terrestrial spectrum, this parameter is about 70 mA/cm^2. As previously described, a fraction of this value can be converted by a solar cell. In particular, about 44 out of 70 mA/cm^2 ($\approx 63\%$) can be converted by a crystalline silicon cell, which has a band limit $\lambda_{max} = {hc}/{E_g}$ of about 1.1 eV.

The maximum voltage (in volts) generated by a PV cell can be evaluated starting from the bandgap of the electron-hole pair. Indeed, the electrostatic energy of a generic charge after separation cannot exceed this quantity: thus, the maximum PV voltage of an ideal solar cell is equal to E_g/q. Obviously, real voltage is, generally, lower than this limit. However, semiconductor materials with high energy gaps generate high voltage. As an example, the energy gap of a-Si cells is significantly higher than m-Si cells (1.7 eV and 1.1 eV, respectively); as a consequence, the maximum generated voltage is 0.8 V and 0.6 V, respectively. On the contrary, high voltage corresponds to narrow band in the spectral response (0.75 μm for a-Si, and 1.1 μm for m-Si) and low current density (≈ 13 mA/cm^2 for a-Si and ≈ 35 mA/cm^2 for m-Si under solar irradiance of 1000 W/m^2). The optimal solution maximizes the generated power, thus selecting a compromise between voltage and current generation.

1.2.1 Equivalent circuit of a solar cell

As a first approximation, the electrical performance of a solar cell can be described by an equivalent electric circuit. In literature, many circuits are used, with a variable number of parameters [12]. The simplest circuit consists of an ideal

current source, which is proportional to irradiance, and of an anti-parallel connected diode. On the contrary, one of the most used circuits is presented in Figure 1-5. This model includes other two elements (a parallel connected shunt resistance R_{sh} and a series resistance R_s) and permits to better describe the performance of PV cells. The shunt resistance represents leakage current flowing through the lateral surfaces of the cell, which are insulated ("edge insulation") from the manufacturing.
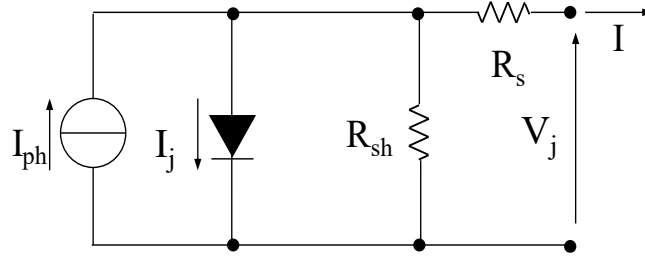
Figure 1-5: Equivalent circuit of a solar cell.

On the contrary, the series resistance consists of different terms, being the sum of the volumetric resistance of the semiconductor, the electrodes resistance and their own contacts. In particular, the most important term is due to the frontal electrode that has a grid shape: it consists of "busbars" (from 2/3 in the older cells to 10 in the most recent ones) and "fingers" (perpendicular to the busbars). The first ones permit to electrically connect the adjacent cells, while the fingers collect the current generated on the whole surface of the cell under sunlight.

The following equations are obtained by applying the Kirchhoff's voltage and current laws to the circuit shown in Figure 1-5:

$$I = I_{ph} - I_j - V_j/R_{sh} \qquad where \ I_j = I_0 \cdot \left(e^{\frac{q \cdot V_j}{n \cdot k_B \cdot T_c}} - 1 \right) \tag{1-7}$$

$$V = V_j - R_s I \tag{1-8}$$

where V is the voltage across the load terminals, and I is the generated PV current. Equation (1-7) describes the I-V characteristic curve of a PV cell: it is implicit, and its extended form is the following [13]:

$$I = I_{ph} - I_0 \cdot \left(e^{\frac{q \cdot V_j}{n \cdot k_B \cdot T_c}} - 1 \right) - (V + R_s \cdot I)/R_{sh} \tag{1-9}$$

For this reason, its solution is complex and numerical methods may be preferred rather than analytical ones.

In this case, the equivalent circuit is defined by 5 parameters: I_{ph}, the reverse saturation current I_0, the non-ideality factor n, R_s and R_{sh}. In specific conditions of irradiance and cell temperature, the *I-V* characteristic curve of a PV generator can be traced starting from the knowledge of these five parameters. Equation (1-9) is transcendental, and it can be solved numerically or with analytical approximation. Moreover, the power curve *P-V* of the generator can be obtained as well. The most important point of the *P-V* curve is its maximum $P_M(V_M, I_M)$ and it lies between the short circuit (0, I_{sc}) and the open-circuit (V_{oc}, 0) points. Another important quantity form the *I-V* curve is the fill factor K_f, which is the ratio between P_M and $V_{oc} \cdot I_{sc}$, and evaluates the deviation from the ideal curve due to the diode and the resistances R_s and R_{sh}. In crystalline silicon cells, K_f ranges between about 0.72 and 0.76. These values correspond to $I_M/I_{sc} \approx 0.90$ - 0.95 and $V_M/V_{oc} \approx 0.8$. Considering these resistances, the following effects occur with respect to the ideal *I-V* curve. When R_{sh} is parallel connected to the current source and the diode, the open-circuit voltage V_{oc} decreases and the slope dI/dV of the *I-V* curve in the region close to short circuit condition increases (in absolute value). Similarly, when Rs is series connected, the short-circuit current I_{sc} decreases and the slope dI/dV of the *I-V* curve in the region close to open-circuit condition decreases (in absolute value).

The complete *I-V* characteristic of a PV cell extends in the second and in the fourth quadrants (Figure 1-6). In these regions, the behaviour of the cell is different: indeed, it operates as a load with reverse voltage ($V<0$, $I>0$) in the second quadrant and with reverse current ($V>0$, $I<0$) in the fourth quadrant. However, operating conditions are dangerous when the working point of the solar cell exceeds the hyperbola of the maximum power dissipated by the cell (P_{dM} in Figure 1-6). Moreover, in case of reverse voltage, if a specific value named *breakdown voltage* V_b is exceeded (generally, a few tens of volts for crystalline silicon cells), the PV cell fails, causing a short-circuit.
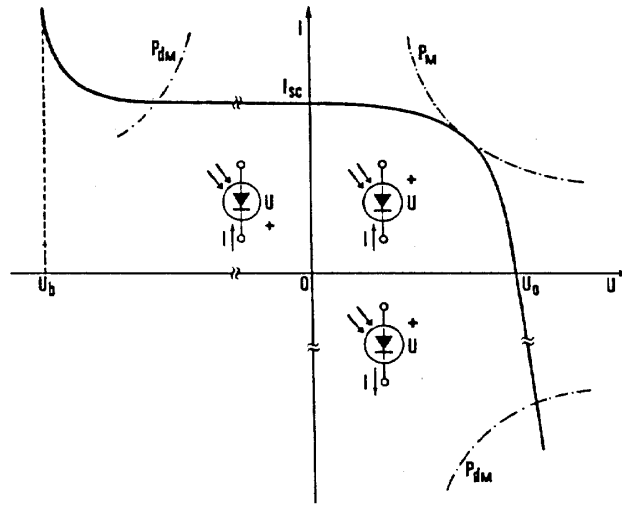
Figure 1-6: Different modes of operation of a solar cell.

1.2.2 Dependence on irradiance and temperature

The *I-V* curve of PV cells is affected by cell temperature (T_c) and irradiance conditions. For a specific temperature value, when irradiance *G* decreases, the following effects occur:

- The short-circuit current I_{sc} proportionally decreases.
- The open-circuit voltage V_{oc} logarithmically decreases according to [14].

In Figure 1-7, the effects of variable *G* on the *I-V* curve are presented, as well as the locus of the maximum power points (dot line). The most evident effect due to variable irradiance is the modification of I_{sc}. Actually, the variation of V_{oc} is almost negligible in a wide range of *G*, and it becomes significant for low *G* values only ($G << 200$ W/m^2). In c-Si cells, the effects on the *I*-V curve due to variable irradiance occur with time constants in the range of about 10—20 µs. On the contrary, for a specific irradiance, the effects on the curve when the cell temperature increases are the following:

- The photovoltaic current I_{ph} (and I_{sc} as well) slightly increases due to a reduction of the bandgap (typical $dJ_{sc}/dT_c =0.01$ mA·cm^{-2}·°C^{-1} for c-Si, while a higher reduction occurs for a-Si).
- The diode current I_j increases, leading to lower V_{oc} (typical $dV_{oc}/dT_c =-2.2$ mV°C^{-1}).

Maximum power increases with increasing irradiance
Maximum power voltage changes little with irradiance
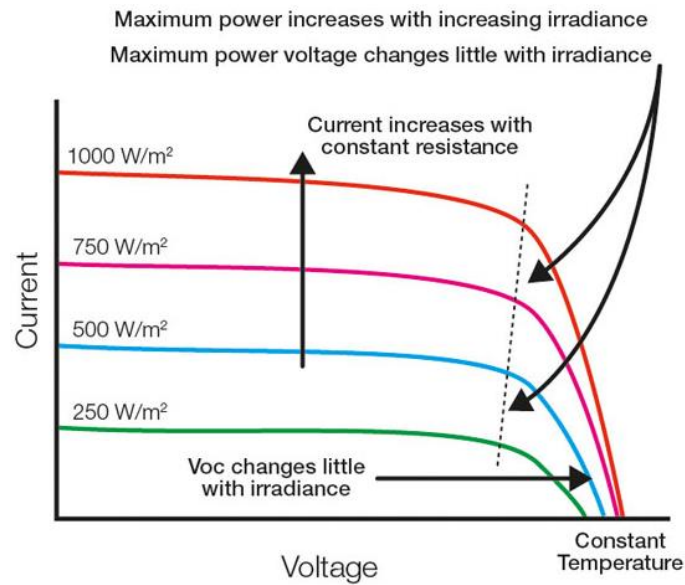
Figure 1-7: $I(V)$ characteristic of a PV generator depending on irradiance.

As a consequence, the thermal gradient of the maximum power with respect to rated conditions (P_{STC}) can be assumed constant. Indeed, typical values for $dP_M/dT_c \cdot 1/P_{STC}$ are in the range -0.38 − -0.35 %°C^{-1} for c-Si, while the value may be lower for a-Si values. In real applications, the current I_{sc} is assumed to be affected by G only and the voltage V_{oc} by T_c only.
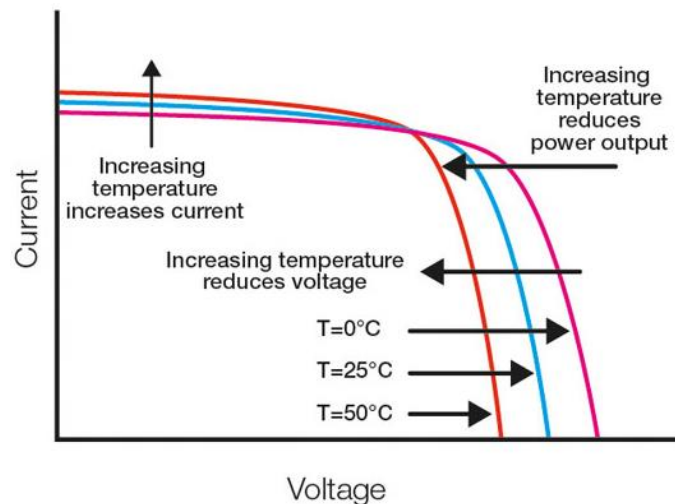
Figure 1-8: $I(V)$ characteristic of a PV generator depending on temperature.

1.2.3 Sources of losses in a photovoltaic cell

The conversion of solar irradiance into electrical power in a PV cell is affected by losses that cannot be avoided completely. The most important sources of losses are the following:

- Reflection and covering of the PV cell surface (up to ≈10%). A low amount of the radiation reaching the cell surface hits the front grid and can be reflected. Antireflection coatings are used to reduce these losses; recently, PV cells can be manufactured with their electrical contacts on the rear surface: this solution permits to minimize the surface of front grid (thus, of reflection losses).

- Energy surplus of the photons reaching PV surface (up to ≈25%). A part of the absorbed energy is converted by the cell into electrical energy only. Actually, if photons energy is higher than the quantity to generate electron-hole pairs, this surplus energy is lost as thermal energy.

- Lack of energy for the incident photons (up to ≈20%). If photons energy is lower than the quantity to generate electron-hole pairs, no conversion is carried out and thus energy is absorbed as heat.

- Recombination factor (up to ≈2%). The junction filed keeps the electron-hole pairs separate; however, some pairs may get recombined, lowering the energy conversion of the cell. Actually, their energy is absorbed as thermal energy, and this loss is affected by the presence of impurities and defects inside the p-n junction material.

- Fill Factor (up to ≈20%). The presence of the diode and resistive effects in the PV cell (R_s and R_{sh}) lowers electrical conversion and modifies the *I-V* curve of the cell. As a consequence, the real characteristic curve of the cell is distorted with respect to the ideal (rectangular) one.

The primary input power of PV generators is not affected by the produced electrical power (or the absorbed power from the connected load), being constant for a specific installation site and in specific weather conditions. The conversion efficiency of a PV cell, i.e., the ratio between the maximum power PM and the solar irradiance reaching its surface in Standard Test Conditions (STC), has significantly increased in the last decade. Nowadays, commercial PV modules may achieve an electrical efficiency up to ≈23% [15]. The PV temperature decreases when load increases; however, this effect is negligible for low conversion efficiencies and the maximum cell temperature is reached in open-circuit condition.

1.3 Connection of photovoltaic cells

1.3.1 Series connection of photovoltaic cells

In order to supply common electric loads, the required PV voltage and current must be higher than the values provided by single cells. Thus, it is required to connect several PV cells in series or in parallel. In this context, a common cause of losses in PV generators with several connected cells is the *mismatch* (or *mismatching*). This is the mutual deviation of the *I-V* curves of the different cells due to manufacturing tolerances, defects or not uniform shading phenomena. Figure 1-9 shows a typical example of mismatch of N_s PV cells connected in series (they are part of a *string*) and the characteristic curve for one of them is different from the others. This can be due to manufacturing defects (curve a in Figure 1-9) or to shading (curve a'). As a consequence, the equivalent *I-V* curve (curve c or curve c') is the sum, for a specific current, of two voltage levels: the voltage of the (N_s-1) identical cells and the voltage of the defective/shaded cell. The dashed curve b in Figure 1-9 is the *I-V* curve of the (N_s-1) identical cells and P is the maximum power point.
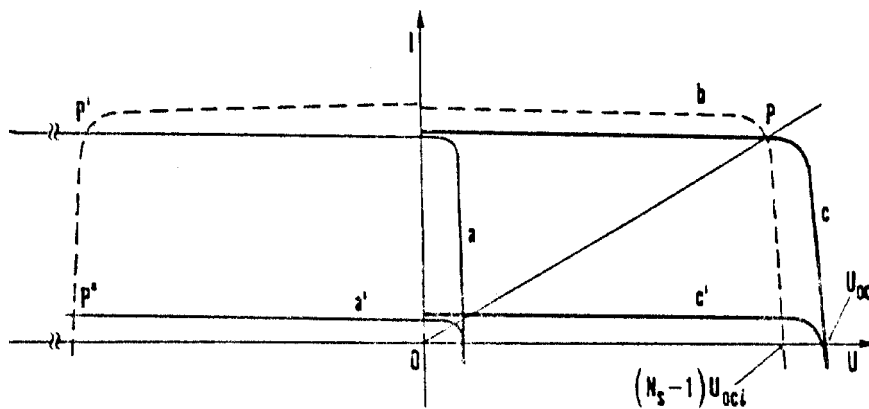
Figure 1-9: *I*(*V*) characteristic of series-connected cells in case of mismatch.

In both configurations (manufacturing defect and shading), the maximum power is always lower than the sum of the maximum powers for the N_s identical cells. However, in case of huge shading (curve c'), the decrease is clear, forcing the entire string to provide low power.

Regarding the equivalent curve of series connected cells, its open-circuit voltage V_{oc} is the sum of the open-circuit voltage for the single cells $V_{oc,i}$. On the

contrary, the equivalent short-circuit current I_{sc} is almost equal to the I_{sc} of the cell with the lowest current:

$$V_{oc} = \sum_i V_{oc,i} \tag{1-10}$$

$$I_{sc} \approx \min(I_{sc,i}) \tag{1-11}$$

In case of a totally shaded cell ($I_{sc} \approx 0$), it should behave in open circuit condition. However, in real applications, a PV cell behaves as a resistor with very high resistance (up to tens or hundreds of ohms). In this case, the cell dissipates thermal power that is affected by the reverse voltage and, thus, by the load (the higher the load, the higher the reverse voltage and the power). The most dangerous condition occurs in short-circuit condition with one shaded cell and N_s-1 irradiated cells. Actually, the voltage generated by the irradiated cells is applied to the shaded one. This case can be displayed in Figure 1-9 applying a symmetry to curve b with respect to the y axis (thus, to the current axis). The intersections in the II quadrant between this symmetric curve and the curves a/a' are the working points of the string. If the shaded cell has to dissipate a too high thermal power, hot spots may originate. Moreover, after a time period that is affected by the duration of the overload and the cooling mode, the PV cell may irreversibly fail. Indeed, if the reverse voltage provided by the N_s-1 irradiated cells exceeds the breakdown voltage, the PV cell fails. The breakdown voltage V_b is in the range 25−50 V for c-Si cells; since each c-Si PV cell usually provides a voltage of $\approx 0.5-0.6$ V, series connections of 50−100 cells may cause the cell failure in case of one shaded cell.

In order to avoid these issues, a diode can be anti-parallel connected to the shaded cell. Actually, in this case, the cell does not behave like a load (thus, with reverse voltage). Moreover, the short-circuit current of the string is not limited to the lowest value: it is the current provided by the other irradiated cells. As a consequence, the power contribution provided by the shaded cell is lost only, while the other cells operate generating their maximum power. This protection device can be connected to each PV cell but one diode is connected to each cell in case of satellite applications only because this solution is too expensive for terrestrial installations. Therefore, one diode is anti-parallel connected to strings of cells connected in series (e.g. groups of 18−24−36).

If a cell is interrupted in a string, the whole string does not provide current (and, thus, power). Moreover, if a short-circuit occurs in a cell, the whole string does not supply power reduced by the cell contribution.

1.3.2 Parallel connection of photovoltaic cells

Considering a parallel connection of N_P cells, if the *I-V* curve of one cell is different from the others (e.g. due to shading), the equivalent curve is the sum, for a specific voltage, of the currents for the N_P-1 irradiated cells and the current of the shaded cell. In particular, the equivalent short-circuit current is the sum of the short-circuit currents of the N_P cells, while the equivalent open-circuit voltage is the lowest open-circuit voltage between the N_P cells:

$$I_{sc} = \sum_i I_{sc,i} \tag{1-12}$$

$$V_{oc} \approx \min(V_{oc,i}) \tag{1-13}$$

In case of one shaded cell, the behaviour is similar to a parallel configuration of N_P-1 cells. The worst condition occurs at the open-circuit condition because the shaded cell is forced to absorb the current from the N_P-1 irradiated cells. In this case, the high-power absorption increases the temperature of the cell and may damage it. Regarding the irradiated cells, their behaviour depends on the shaded cell. Actually, if the shaded cell behaves like an open-circuit, the other cells work in parallel again. On the contrary, their working point is at the short-circuit condition. However, this condition is not conventional because, generally, the parallel connection of individual cells is not performed. Regarding the load, the shading effect on a single cell is less dangerous with respect to the series connection case. A protection device (a diode) can be series-connected to each PV cell in parallel in order to avoid a shaded cell to work as a load, absorbing current from the others.

However, the voltage drop across the terminals of each diode is almost equal to the voltage provided by one PV cell. Thus, this protection device is, generally, connected to strings with several tens of series-connected cells.

In conclusion, in case of series or parallel connection of PV cells, the installation of devices with *I-V* curve as similar as possible is strongly preferable to guarantee the "matching" of the cells. To reach this goal, PV cells are subject to a careful selection ("sorting") during the manufacturing process of a module. The most important criteria during the selection cells consists of identifying PV cells with the same electrical behaviour, i.e. having their most important parameters (I_{sc}, V_{oc} and P_M) as similar as possible. Obviously, the sorting cannot avoid feasible power losses like the term due to the connection of PV cells in a module, i.e. the

maximum power of a PV module is lower than the sum of maximum powers for the cells. These losses can be up to 2-3% of the rated power and cannot be avoided. Nevertheless, the sorting does not exclude the occurrence of mismatch phenomena due to external sources (e.g. shading phenomena of some PV cells of a module).

1.3.3 Photovoltaic module

A PV module is an environmentally protected assembly of PV cells and generates electrical energy when exposed to solar irradiance. It may consist of a variable number of cells (e.g. from 36 to 96). Different manufacturing techniques permit to assemble the module protected from the environmental agents (humidity, hail, wind, dust, etc.) while keeping its temperature in a safety range (generally, 45−75 °C). Regarding c-Si technology, monocrystalline cells are manufactured with the crystal growth technique and have a round shape. However, the efficiency of PV modules with round shaped cells is limited due to poor space exploitation. Monocrystalline cells can be furtherly subject to processes to assume a square shape by cutting the borders: in this case, a part of material is wasted, being recycled in another step. On the contrary, polycrystalline cells are square shaped, having a better exploitation of the module surface. The PV cells are electrically welded, being, then, enclosed between two flat layers. The front layer consists of a glass layer with high transmittance as it must be transparent to light. The rear cover is made of a glass layer or a thin layer of Mylar, Tedlar or PET. A thermoplastic polymer surrounds the cells, and it welds together these two layers, making the structure compact and weatherproof. This polymer (Ethylene Vinyl Acetate, EVA) is transparent to light and durable with time. Moreover, the EVA guarantees electric insulation between the cells, avoiding the penetration of moisture (and, thus, corrosion). However, this polymer is not resistant to high temperatures (> 85 °C).

1.3.4 Main parameters of a photovoltaic module

The most important parameter of a PV module is its global conversion efficiency. This quantity is evaluated at Standard Test Conditions (STC), corresponding to irradiance G = 1000 W/m^2, air mass AM = 1.5 and module temperature $T_{c,STC}$=25°C. These conditions correspond to typical spring or autumn sunny days. The module efficiency is affected by the PV technology, ranging between 7% and 24%. The environmental conditions in summer or in winter are less favourable to solar conversion: actually, reductions up to $\approx$ 2% occur due to lower current density.

Another parameter of PV modules is their peak power (measured in Watt), which is the maximum output power in STC. Common values for PV modules are up to ≈400 W, depending on the technology. Several modules can be connected to achieve higher power, creating more complex structures. The following terms are commonly used to identify such systems:

- PV string. It is a group of modules, or cells, which are mechanically pre-assembled and electrically series connected.
- PV array. It is a group of modules assembled with the support structure.
- PV field or PV system. It is the group of the PV arrays in the plant. Most of systems consist of the parallel connection of PV strings, made of series connected modules.

Moreover, the following electrical quantities are provided at STC: the short-circuit current I_{sc}, the open-circuit voltage V_{oc}, the current and the voltage at the maximum power point (I_M and V_M, respectively).

These test conditions are created in dedicated laboratories and another quantity is provided to better describe the performance pf PV modules (the Nominal Operating Cell Temperature, *NOCT*). This parameter is the module temperature when it operates in open circuit condition, being in thermal equilibrium with the following environmental conditions: $G = 800$ W/m^2, $T_a = 20$°C, and wind speed = 1 m/s. Generally, this quantity is in the range 42–50°C and its knowledge permits to estimate the module temperature in any weather condition. Actually, the temperature difference between T_c and T_a can be assumed linearly dependent on irradiance G. Under this assumption, the PV temperature can be evaluated with the following equation:

$$T_c = T_a + \frac{NOCT - 20°C}{800\ ^W/_{m^2}} \cdot G \qquad (1\text{-}14)$$

The *I-V* curve shape of a PV module is equal to a single cell; however, the voltage scale of the curve is different. Indeed, connecting many PV cells in series increases the generated PV voltage. On the contrary, connecting many strings of PV modules in parallel increases the PV output current. Regarding stand-alone applications, the number of series connected cells in PV modules is in the range 34-40. In this case, PV modules need to be coupled with batteries and, thus, PV voltage has to allow their charge (typically 12 V), even at high temperatures (up to ≈60°C).

1.3.5 Protection of photovoltaic systems

Similarly to individual cells, the electrical mismatch between the *I-V* curves of different PV modules includes power losses and other issues in the system. Hence, proper protection devices are required to lower power reduction due to electrical mismatch. Moreover, in case of shaded modules, temperature peaks may occur, and they may cause modules failure. A bypass diode D_p can be used to protect the modules from reverse voltage in case of shading. Moreover, the string power is reduced to the contribution of the irradiated modules, losing the contribution of the shaded one only. In a PV string with series connected modules, this device is connected to each module of the string (or to a group of cells in the module, generally 18 or 24).

Another diode D_s can be used in parallel connection of PV strings to avoid asymmetric voltages. This device is series connected to each string to permit the flow of string current. However, this diode leads to a voltage drop, thus to a power loss, due to its threshold voltage in the range 0.6−0.8 V. In order to limit this power loss, the voltage drop has to be negligible with respect to the string voltage. If some cells of a PV string are defective, their open-circuit voltages are in mismatch (or in asymmetry) with respect to the healthy strings that are parallel connected. In such case, the diode D_s isolates the defective string, becoming inactive in terms of power generation. In normal operation, the voltage of the working point is significantly lower than the open-circuit voltage, reducing the occurrence probability of this condition. Actually, in PV generators with maximum power point trackers, the voltage of working point is ≈80% of the open-circuit voltage. Moreover, this diode protects the PV strings in case of shading: in this case, a reverse current may flow in the system due to the electromotive force generated from external generators (e.g. storage units, engines).

1.3.6 Configurations of photovoltaic systems

The selection of the proper array configuration is fundamental during the design of a PV system. Actually, the performance and the reliability of PV generators is affected by the selection of the connections between PV modules in the plant. This is a key aspect when working conditions are perturbed and far from the ideal ones, as in case of non-uniformity for cell parameters, shading phenomena, degradation of cell materials, breakdowns, lightning strikes, etc. In this context, different configurations of the PV system can be adopted, and the selection of the optimal configuration is affected by several constraints (e.g., constant voltage to the load,

minimum power losses, etc.). One of the most diffuse configurations is the parallel of series (configuration b in Figure 1-10).
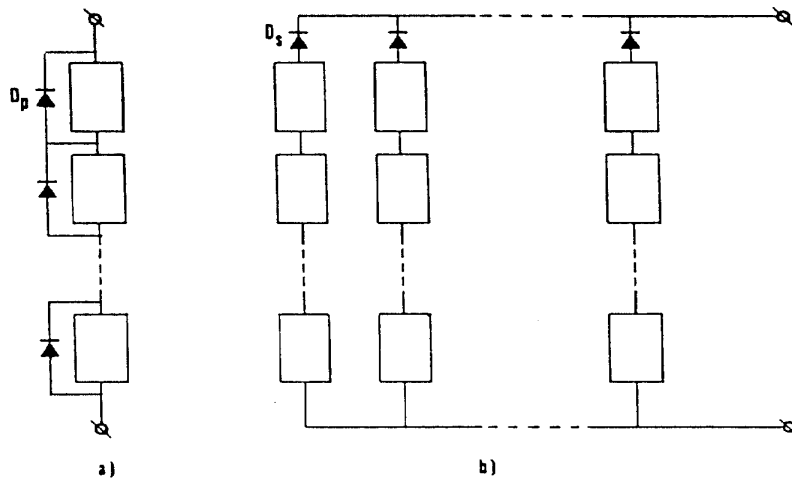
Figure 1-10: Protection diodes connected to PV generators: single string (a) vs parallel of series configuration (b).

In this case, a shaded cell causes a slight reduction of generated voltage, and the power produced by the PV string is lost. Another diffuse configuration is the series of parallel (Figure 1-11). In this case, the required number of diodes D_p is lower with respect to the parallel of series.
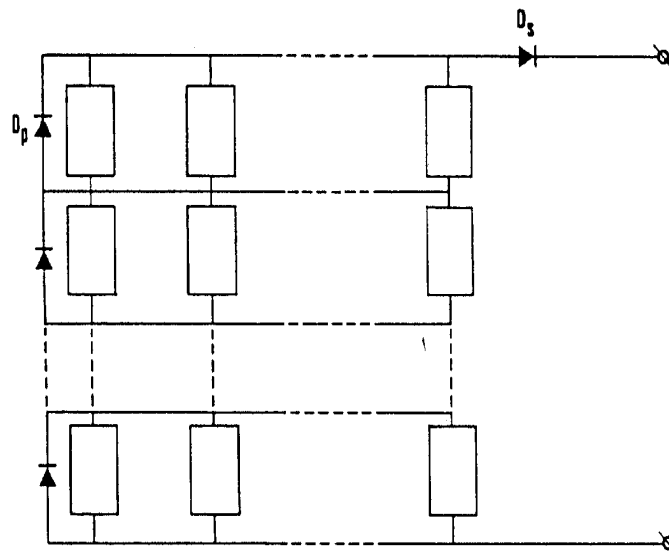
Figure 1-11: Series of parallel configuration.

Actually, one diode is connected in parallel to each string (instead of one diode for each module or groups of modules), but this device is requested to withstand a higher current. However, in this configuration, no protection diodes are series connected to the modules, and shaded cells may danger the corresponding module, especially in open-circuit condition. When a PV generator fulfil a load, the PV operation point is the intersection between the I-V curves of the generator and of the load. This point can be in any part of the PV I-V curve, between the short-circuit and the open-circuit conditions. Finally, the I-V curve of PV generators can be divided into two regions. The first region includes points between the short-circuit condition ($V = 0$ V, $I = I_{sc}$) and the maximum power point (V_M, I_M), while the second region extends between the MPP and the open-circuit condition ($V = V_{oc}$, $I = 0$ A). These two regions can be approximated by two straight lines with different angular coefficient: in particular, the first part can be approximated using a Norton equivalent circuit, while the second one using a Thévenin equivalent circuit.

1.3.7 Connection of photovoltaic generators to loads

At each environmental condition of irradiance and air temperature, PV generators should operate in the neighbourhood of their maximum power point. When a PV system supplies a resistive load, the identification of the maximum power point, for specific weather conditions, permits to determine an optimal resistance R_o. Actually, a straight line can be traced by connecting the origin of the I-V graph and the Maximum Power Point (MPP). Its slope $1/R_o$ permits to identify the optimal resistance value R_o. In order to exploit the maximum power produced by the PV generator, the knowledge of the slope for the generator I-V curve is required. Indeed, to transfer the maximum power from the generator to a generic load, the slope of the generator I-V curve must be equal to the slope of the resistive load, thus $|dI/dV| = 1/R_o$. The input power of PV generators is imposed by solar radiation and, thus, cannot be modified. Adapting the load to solar systems is required in order to extract the maximum PV power. This condition is not acceptable for traditional generators, whose input power can be modified under request.

As previously described, at constant temperature, an increase of irradiance includes a proportional increase of I_{sc} for the PV generator. On the contrary, the V_{oc} can be assumed independent on irradiance modifications. As a consequence, the locus of maximum power points, under different irradiance conditions and constant temperature, is approximated by a vertical line. The coupling between a generator and its load is optimal when the characteristic curve of the load superimoposes the

locus of the maximum power points for the generator. For these reasons, the direct connection of PV generators to resistive loads is not recommended. Actually, this condition occurs with electrochemical batteries, DC motors (thanks to the back electromotive force), or electrolytic processes (e.g. fuels cells performing the water electrolysis to generate the fuel hydrogen) due to the polarization of the electromotive force. In case of low scale PV plants (with rated power up to few kW), PV generators can be connected directly to DC motors for water pumping, drying or ventilation systems. This configuration is quite simple, improving the reliability of the PV system.

1.3.8 Components of photovoltaic systems

PV systems consist of many components in order to use the output electrical energy other than PV modules:

- Maximum Power Point Tracker (MPPT). The input energy of PV generators is the solar irradiation, which is affected by sun condition. In order to extract the maximum PV power, DC/DC converters are commonly used to set the working point of PV generators in the neighbourhood of the maximum power point.

- DC/AC converters. PV generators provide electrical energy in Direct Current (DC). However, most of users are fed with electrical energy Alternating Current (AC). The DC/AC conversion is performed using DC/AC converters (or inverters). These devices commonly include the hardware and the software to achieve the maximum PV power also under electrical mismatch of PV cells.

- PV connectors. These components consist of a copper core and an external plastic insulation, being resistant to weather (rain, heat and UV light). They permit the link between PV modules, and each PV module is equipped with two connectors (one positive and one negative terminal).

- Fuses. These circuit breakers protect the system against overcurrent phenomena. Indeed, they consist of an internal filament, which interrupts the circuit (i.e., by melting) in case of overcurrent. Each PV string can be equipped with two fuses.

- Blocking diodes. These devices avoid reverse current phenomena in shaded string. In PV arrays with a high number of strings, each string is equipped with a blocking diode.

- DC breaker. This circuit breaker disconnects the PV array from the inverter. The number of installed DC breakers varies according to the PV plant: one unique breaker can be installed for the whole array or several switches (for instance, one for each string) can protect large scale plants.
- Automatic AC circuit breaker. This device protects the system by interrupting two parts of an AC line. In general, each plant is equipped with one or more AC circuit breakers.
- Grid interface. This component checks the voltage source to be within its root mean square and frequency limits.
- General AC breaker. This breaker disconnects the PV plant from the grid. Commonly, it is motorized and coupled with a Residual Current Device (RCD), which is installed before the grid connection.
- Electrochemical energy storage. The profile of solar irradiance is affected by daily and seasonal variability and, thus, the PV generation profile. In case of stand-alone systems, the power supply is required to be interruptible, even with adverse weather condition. In order to guarantee continuous power supply, electrochemical storage is included in the plant. Actually, in case of energy surplus (i.e. PV generation higher than consumption), the additional not consumed energy is used to charge a storage. This component permits to increase the self-sufficiency of the system by consuming that surplus energy at a different time (discharge of the batteries).
- Other electrical safety devices and monitoring systems (Surge Protection Device, SPD, and energy meters).

PV systems can be of two types: "stand-alone" or "grid-connected". The first category includes autonomous plants that are not connected to the electricity grid. On the contrary, the second category includes plants having a connection to the grid and they can be connected as centralized or distributed generators. During the lifetime of PV systems, most of their failures are not due to PV generators. Indeed, most of faults are due to the other components of the plant, commonly named "Balance of System" (BoS). The technology of these components is sufficiently mature to guarantee their correct operation for thousands of working hours. However, PV generators are unconventional, and they may force the devices of the BoS to work in abnormal conditions. In this case, the performance of the BoS components may be worse, leading to more frequent faults and failures.

Chapter 2

Optimization Algorithms

One of the most important lines of research in the PV sector is the determination of the parameters in equivalent circuits. In literature, many models and algorithms are proposed to determine these parameters starting from experimental *I-V* curves [16]. The proposed models can be of three typologies: empirical, analytical [17] or evolutionary [18]. The first type relies on the observation of experimental data: it does not involve complex models, but unrealistic results may be obtained if the experimental datasets are not wide enough. Analytical models are mathematical models providing a closed-form solution, i.e., using systems of analytic functions [19]. The provided solutions are, generally, stable, exact, and are obtained with low computational effort [20]: however, their efficiency significantly drops under certain conditions, e.g., facing nonlinear problems. Finally, evolutionary models permit to investigate efficiently the performance related to the design and optimization of complex problems [21]. They make us of numerical algorithms, and they can be applied to complex geometries and nonlinear problems. However, the identified solutions are approximated, and, in some cases, they require complex solving processes and high computational costs [22]. In the PV context, numerical models are, generally, adopted due to their capability to evaluate the equivalent circuit parameters at any condition. In particular, the most common algorithms are the Levenberg-Marquardt [12], the Simulated Annealing (SA) [23], the Nelder Mead (NM) [24], the Newton-Raphson [25], the genetic [26], and the Particle Swarm Optimization algorithms [27]. In this section, a description of the two algorithms used in this work, as well as the main typologies of numerical algorithms, are presented.

To correctly determine the parameters of the SDM, proper optimization algorithms are used. They aim to identify good approximations to the optimal value of a specific function in a large set of possible solutions. In literature, the algorithms are of two typologies as they can be based on deterministic or probability methods. Regarding deterministic methods, the search strategy does not include a random investigation in the solutions set, but defined rules are applied. The most used search strategies are the following:

- Exhaustive search. This technique is applied when the number of possible solutions is known, and the entire set of solutions is computed. It is used when the time required to compute all the solutions is reasonable.

- Branch and Bound techniques. This strategy is applied when the number of possible solutions is known as well. In particular, the set of candidate solutions are grouped in a rooted tree of solutions (the full set is at the root of the tree) [28]. This search investigates the branches of this tree, i.e., subsets of the solution sets. With respect to the previous technique, this search aims to limit the number of solutions to compute by discarding the branches that cannot lead to better solutions.

- Iterative improvement. In this technique, a trajectory with subsequent changes is followed in the search to identify the optimal solution [29].

- Tabu search. It investigates the solution space by constantly replacing the most recent solution with the best non-visited neighbouring one [30].

On the contrary, the most adopted probability methods are the following:

- Simulated Annealing. This technique simulates the annealing process of a melting metallic structure, which is slowly cooled until the entire structure has solid state (i.e., configuration of minimum energy).

- Genetic algorithms. These techniques consist of evolving a group (or a generation) of candidate solutions (named chromosomes) to a problem at hand, using different operators (e.g., crossover, mutation, or inversion), based on natural selection and evolution theory by Charles Darwin [31].

- Honey bee optimization. This algorithm is based on mating behaviour of honey bees to solve optimization problems [32].

- Plant growth simulation. This technique simulates the rapid growth of plants towards the optimal direction of sunlight. With respect to the other methods, it permits to identify the global optimal solution of an optimization problem [33].

In this thesis work, two methods are selected to solve the optimization problem regarding the parameters extraction from the measurements: the Levenberg-Marquardt (LM) and the Simulated Annealing/Nelder Mead (SA/NM) algorithms.

2.1 Levenberg-Marquardt

The LM algorithm was discovered in 1944 [34,35]. It is an indirect deterministic method to solve nonlinear least squares problems. This algorithm is very effective in curve fitting problems, being preferred to others in such applications. Moreover, it consists of an iterative optimization aiming to minimize the summation of the squares of the error between the reference function and the estimated one. However, the optimization results are strongly affected by the initial values of the variables to optimize, determining the convergence of the method. This method consists of the application of two minimization techniques: the Gradient Descent (GD) and the Gauss-Newton (GN) methods. In particular, for each iteration, the first method modifies the variables in the opposite direction with respect to their gradient. This aims to minimize the objective function of the problem by minimizing the sum of squared values. On the contrary, the second technique applies a linearization of the nonlinear function using a Taylor series expansion [36] around an initial set of variables, named "preliminary estimates".

The LM method uses these two techniques in different moments of the optimization. At the very first steps of the optimization, the GD algorithm is used because initial values of the variables to optimize are far from their optimal values. On the contrary, the GN technique is used after a certain number of iterations, when the variables are close to the optimal results. The characteristic equation of the LM method is the following:

$$[J(p)^T(p) + \lambda I]\delta = J(p)^T \cdot (y - \hat{y}(p)) \qquad (2\text{-}1)$$

where J is the Jacobian matrix, p is the vector of the variables to optimize, δ is the variation of the variables at a certain step, y and $\hat{y}$ are, respectively, the reference function value and the result estimated with the model. The parameter λ (named "damping parameter") is a control quantity of the iterative process that

varies at each step. Actually, in the very first part of the optimization, i.e. the variables to optimize are far from their optimal values, the GD technique is used and high values of λ are generated. This parameter increases if the previous iteration generates a limited reduction in the objective function. On the contrary, if λ decreases, the values of the variables get close to the optimal ones, and the GN method is applied. As a consequence, the quantity λ at the end of the optimization is required to be low in order to obtain proper results from the procedure.

2.2 Simulated Annealing/Nelder Mead

The SA/NM algorithm consists of the application of two techniques: the Simulated Annealing (SA) and the Nelder Mead (NM) methods.

The first takes inspiration from the annealing process of steel and ceramic. In particular, it consists of heating a material and then, slowly cooling it in order to obtain specific physical properties [23]. During the heating process, the energy of the atoms in the metallic/ceramic structure increases, being able to move from their initial position, corresponding to a configuration of minimum local energy. After the heating phase, the structure is slowly cooled: in this condition, it recrystallizes and a final structure with lower energy with respect to the initial one (global minimum of energy) is obtained. The SA method is probabilistic and iterative, consisting of two cycles. The external cycle relies on a control quantity c to check the procedure. At the nth iteration (corresponding to a constant temperature T_n), this quantity c_n is computed starting from its value at the previous step (c_{n-1}) and a parameter named "cooling rate" (α) as $c_n = c_{n-1} \cdot \alpha$. The quantity α varies between 0 and 1, providing indication regarding the speed of cooling process, typical values are between 0.95 and 0.98 in order to guarantee a sufficiently slow cooling.

Regarding the internal cycle, at each iteration, the initial variables correspond to the optimal values from the previous one. Then, the best configuration identified at the end of the internal cycle is set as the reference for the external cycle. The main advantage of this technique consists of the possibility to perform a global optimization avoiding local minima. Actually, this is due to the acceptance criterion of the configurations as solutions leading to worse objective functions may be accepted as well. In some cases, these solutions may lead to a global better objective function: thus, this operation permits to avoid a local minimum and to correctly identify the global one.

At the nth iteration of the external cycle (thus, at each temperature T_n), the set of variables x_i^n identified at the ith step of the internal cycle is accepted according to the value of the objective function f_i^n. Actually, the following conditions may verify: the objective function at the ith step may be lower or higher than the corresponding value at the previous step $(i\text{-}1)^{th}$. In the first case, the newer configuration is accepted, while, in the second case, the probability of acceptance P_A relies on the following probability [37]:

$$P_A = e^{(f_i^n - f_{i-1}^n)/(k_B \cdot T_n)} \tag{2-2}$$

The probability P_A is affected by the temperature of the step. Indeed, at the beginning of the procedure, the search domain of solutions is wide due to the high temperature and probability of acceptance of worsening solutions. As a consequence, the algorithm is capable of avoiding easily local minima. As long as optimization proceeds, the temperature of the metallic/ceramic structure decreases, and the probability P_A gets lower values as well. The stopping criteria of the SA method are, generally, two: the first criterion regards the maximum number of accepted and analysed configurations during the process. The second criterion sets the ending of the technique when the variation of the objective function is lower than a threshold value for a specific number of iterations.

The Nelder-Mead algorithm [38] is known also as the simplex method and it is a direct deterministic optimization method. This technique aims to minimize the objective function in a multidimensional space using the concept of simplex. A simplex is a polytope (i.e., the convex hull of points in a Euclidean space [39]) with $n+1$ vertices in a space with n dimensions. Common simplexes are a segment in a straight line, a triangle in the plane, or a tetrahedron in space.

At the nth iteration of the external cycle, the method investigates the polytope identified in the previous step. In particular, the behaviour of the objective function is assessed in the neighbourhood of the simplex vertices. After this operation, the point of the domain corresponding to the worst objective function is identified and replaced with a new point. The worst point can be replaced by the center of gravity of the remaining points, and the objective function in the new point is evaluated. If it is better than the value in the worst point, the method proceeds in exploring solutions with an exponential trend in the new point direction. On the contrary, directions of a point providing better solutions are selected. The NM algorithm approximates the optimum solution of an optimization problem in n variables when

the objective function is smooth and unimodal. However, the method may get stuck in local minima as other algorithms. In this case, it restarts building a new simplex with the best value identified so far as its initial configuration. The stop criterion of the algorithm is based on the evaluation of the standard deviation for the values of the objective function. Variations of this algorithm can be performed to properly solve many optimization problems. A common variation consists of using a small simplex of constant amplitude following the gradient direction.

Chapter 3

Electronic Measurement Systems

The present work analyses data that are acquired using two different electronic measurement systems, which are periodically calibrated. The first one is at Politecnico di Torino (Turin, Italy), while the second one is at the Universidad de Jaén (Jaèn, Spain). The two measurement systems use the same method to trace the *I-V* curve of PV generators and their scheme is presented in this chapter.

3.1 Charging method of a capacitive load

The method used in the two measurement systems to trace the *I-V* curve of PV generators is the same. Actually, this operation is performed using an Automatic Data Acquisition System (ADAS), which permits to store simultaneously the irradiance G, the air temperature T_a, the module temperature T_{PV}, and the current and voltage signals. The acquisition of these quantities is performed using a capacitive load, which is initially discharged. When the power breaker is closed, the PV generator supplies the capacitor working from the short-circuit to the open-circuit state. The size of the load is selected to have proper durations of the transient charge. According to [40], the duration of the capacitor transient t is a function of its capacitance C, of the short-circuit current I_{sc}, of the open-circuit voltage V_{oc}, of the number of PV strings in parallel N_p, and of the number of PV modules in series per string N_s (consisting of N_c series-connected cells):

$$t = 1.82 \cdot C \cdot \frac{N_s \cdot V_{oc}}{N_p \cdot I_{sc}}$$
(3-1)

However, since the electrical quantities of PV modules are affected by weather conditions (irradiance and air temperature), the duration of the capacitor transient is affected by these factors as well. In the present work, a load with $C = 10$ mF is used, resulting in a t value in the range 0.2 s (under medium and high irradiance) - 1 s (under low irradiance). Finally, the capacitor charging method intrinsically, provides values of maximum power at STC lower than the real quantity. This is due to the internal parasitic capacity of the PV module, which absorbs a certain amount of PV current generated while charging the external capacitor.

The measurement system in Italy consists of the following components [40]:

- A notebook PC runs a LabVIEW software to emulate a digital storage oscilloscope.
- A multifunction data acquisition board with one A/D converter (successive approximation technology, 16 bit-resolution, sampling rate up to 1.25 MSa/s, maximum input of ±10 V, internal amplifier gains for lower ranges) and multiplexer (Figure 3-1a).
- A differential voltage probe with two attenuation ratios 20:1 and 200:1 for voltage levels up to 140 V and 1400 V, respectively (Figure 3-1b).
- Two current probes (Hall effect) with output sensitivity of 100 mV/A for current values up to ±30 A. One of them is used to acquire current signal, while the other is for trigger source (Figure 3-1c).
- A secondary standard pyranometer with typical uncertainty lower than $\pm1\%$ operating up to 4000 W/m^2 (Figure 3-1d).
- A reference solar cell in monocrystalline silicon with typical uncertainty of ±20 W/m^2 (Figure 3-1f).
- A capacitive load with capacitance of 10 mF (Figure 3-1e).
- A calibrated thermometer measures air temperature (Figure 3-1g), and a temperature probe measures the temperature on the rear side of the modules (Figure 3-1h).

In Figure 3-1, the pictures of the equipment are reported. According to the specifications from datasheet, the measurement uncertainties are $\pm0.1\%$ for voltage, $\pm1\%$ for current, $\pm1\%$ for power, $\pm1\%$ or ±20 W/m^2 for the irradiance sensors, ±2 °C for module temperature, and ±0.2 °C for ambient temperature. Regarding the voltage and current probes, their conversion constants were verified in the laboratory by using a calibrated power supply. Initially, higher uncertainties than the values in the datasheets were detected: hence, new adjusted constants were

identified in the laboratory, obtaining comparable uncertainties with the technical specifications by the manufacturer. As a result, the uncertainty of the measurement system, which is the square root of the sum among the squares of each contribution, is ≈±4%.

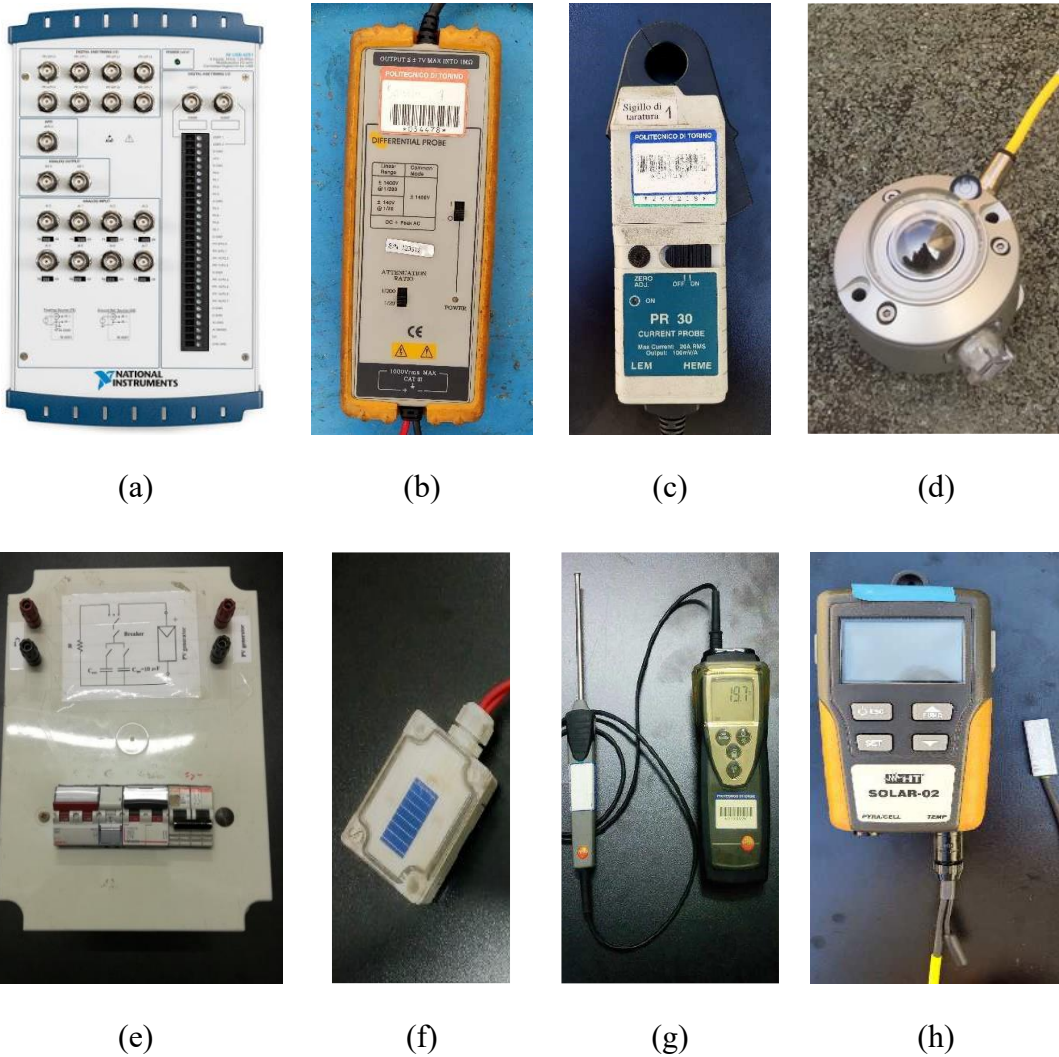| (a) | (b) | (c) | (d) |

| (e) | (f) | (g) | (h) |

Figure 3-1: Equipment of the measurement system used in Italy.

Figure 3-2 presents the scheme of the measurement system, including its different components.
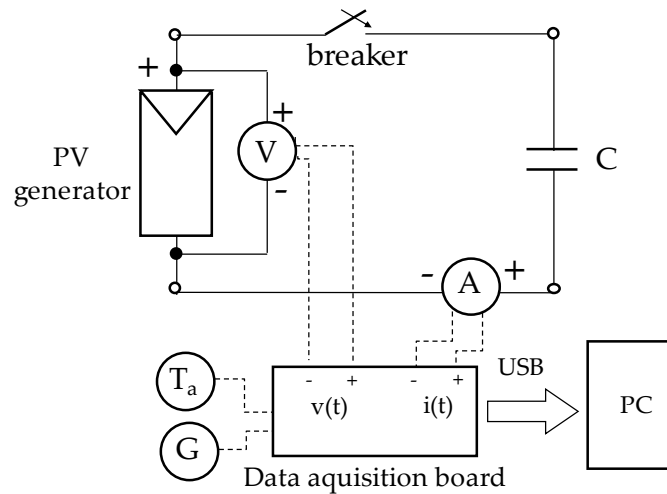
Figure 3-2: Scheme of the measurement system used in Italy.

3.2 Measurement system used in Spain

The ADAS developed in Spain is used in two different systems, which are located on the roof of the laboratory of solar energy in the "Escuela Politécnica Superior - Universidad de Jaén". In this work, they will be referred to as "Tracker System" (TS) and "Fixed System" (FS) because one of their main differences is the integration of a sun tracker. Actually, in the TS, a two-axes tracker is included, while the modules installed in the second system have a fixed installation. The systems permit to periodically acquire the *I-V* curves of up to four PV generators, as well as the main weather quantities. The scheme of the two measurement systems is presented in Figure 3-3. In this figure, the components in blue boxes are common to the systems, while the other components are included in the TS (purple boxes), or in the FS (orange boxes). The components of the systems are located on the roof of the laboratory (left part of Figure 3-3), or in the laboratory (right part of Figure 3-3). Regarding the part of the system on the roof, it includes the PV modules and their metallic support, and the sensors for the acquisition of the main quantities (voltage, current, irradiance, air temperature and cell temperature).

Each PV module includes an electronic board in its junction box, which is designed by the IDEA research group of the Universidad de Jaén. The temperature of the module on its rear surface is acquired with a Pt100 sensor (4-wires resistance measurement). The other instruments of the equipment are located in the laboratory. In particular, two high performance multimeters (resolution of $6^{1/2}$ digits and uncertainty < 1 mV during operating conditions).
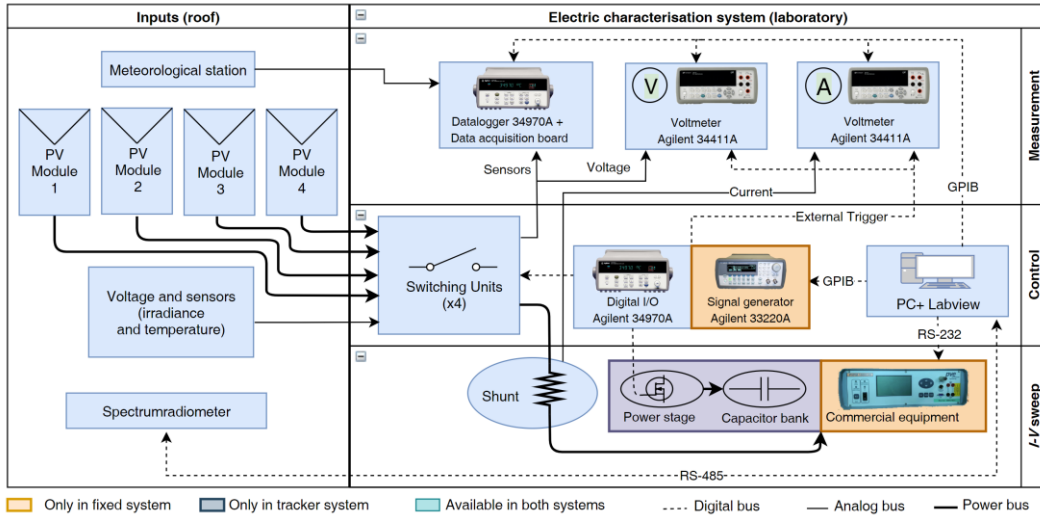
Figure 3-3: Scheme of the measurement systems used in Spain.

These multimeters measure the voltage across the terminals of PV modules, and the voltage drop across a shunt resistor (class 0.5) to determine the corresponding current value. Another difference between the TS and the FS regards the capacitive load and the external trigger used to control the two multimeters. Actually, a handmade capacitor is used in the TS, while a commercial model is used in the FS. Finally, the last difference consists of the external trigger used to synchronize the multimeters: in case of TS, a datalogger working up to 300 V and 1 A is used ($6^{1/2}$ digits and uncertainty = 0.04% on yearly basis), while in the FS a signal generator with 14 bits is included.

Figure 3-4: Multiplex board behind each PV module.

3.3 The electroluminescence test

The ElectroLuminescence test (EL) is one of the most diffused analyses to investigate the degradation in photovoltaic systems. Compared to the other diagnosis methods used to identify defects or failures (InfraRed Thermography, IRT,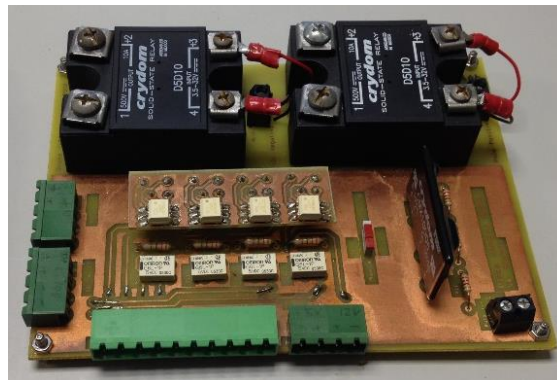 or fluorescence), the EL permits to obtain images of the PV array with noticeably better resolution and level of detail [41] using cost-effective equipment. In most of situations, this test permits to determine the typology of the defects, mainly mechanical, affecting the performance of PV modules. Moreover, this technique has short acquisition times (< 1 min) and it is non-destructive because it does not cause any damage to the modules [42]. One recent field of research consists of obtaining the most important electrical parameters from the EL results only [43,44]. However, the results permit to identify a limited number of defects [45] and a quantitative estimation of the electrical parameters is hard to achieve. For this reason, the tracing of the *I-V* curve and the EL test are, generally, complementary techniques.

3.3.1 Operating principle of the electroluminescence test

The EL test requires the following devices (Figure 3-5):

- A camera captures the InfraRed (IR) radiation emitted by PV generators. In case of on-field inspections, portable devices are suggested.
- A variable power supply forward biases the PV generators under dark conditions.
- A personal computer with a card reader unit acquires the EL images with a post processing software.

PV generators emit electromagnetic radiation under the application of a forward bias (electroluminescence principle), and, during this test, they are placed under a totally shaded condition (a dark room or on-field test can be performed with irradiance < 50-100 W/m^2). In such conditions, they are forward biased, working as Light Emitting Diodes (LED), and they emit radiation with wavelength in the IR region of the spectrum. For crystalline silicon modules, the emission spectrum is in the range 950 – 1350 nm with a peak corresponding to ≈1150 nm (Figure 3-6). The emitted photons can be detected using a sensitive camera equipped with indium gallium arsenide (InGaAs) photodiodes, or silicon devices, i.e., silicon Charge-Coupled Device (CCD) or CMOS.
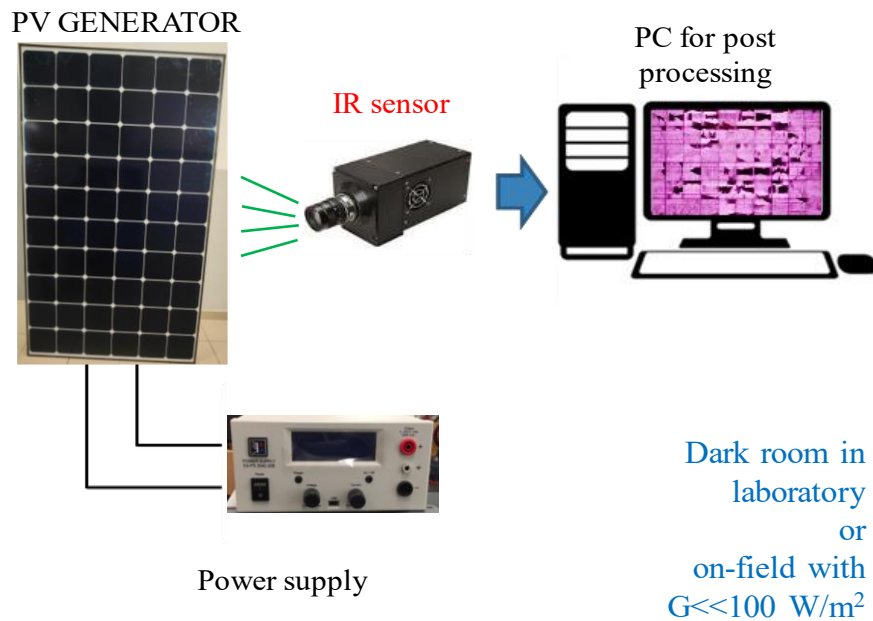
Figure 3-5: Equipment required to perform the EL test on PV modules.

The absorption curve of the InGaAS detectors has a good match with the emission spectrum of c-Si modules (Figure 3-7 reports the quantum efficiency of the InGaAs detector, which is ≈80% in the peak region). InGaAs sensors provide EL images with higher resolution than silicon devices, but they are expensive.
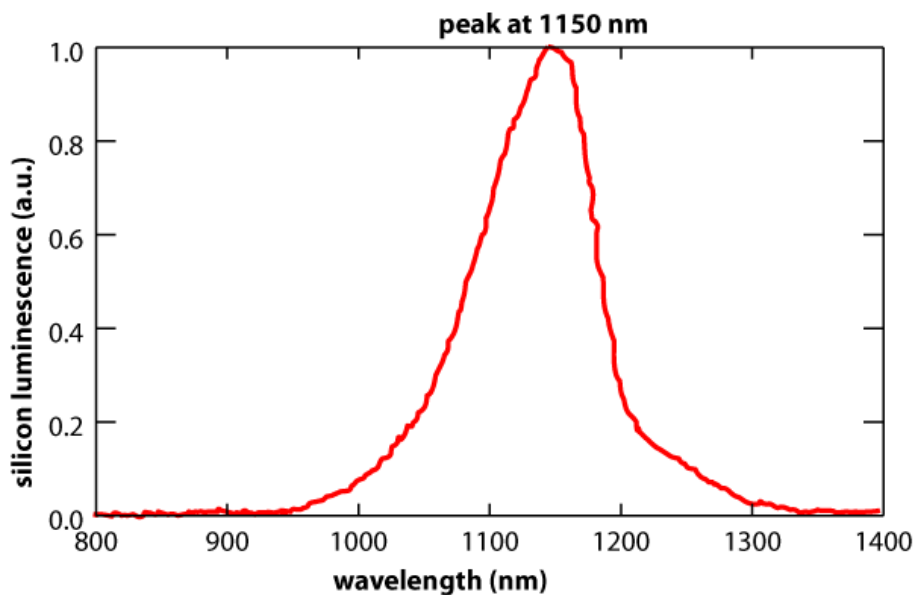
Figure 3-6: Emission spectrum of silicon with its peak at 1150 nm.

On the contrary, the cost of CCD/CMOS sensors is much lower, but their spectral response is poorer in the range between 1000 and 1200 nm, reaching a maximum value of 20% [46]. In this context, many researchers are focusing on maximizing the response of CCD/CMOS sensors, obtaining pictures with comparable quality to InGaAs detectors [47].

Figure 3-7: Quantum efficiency of the InGaAs detectors.

Figure 3-8 presents the pictures of an EL test carried out on a PV module affected by Potential Induced Degradation (PID) using CCD (left) and InGaAs (right) sensors: no noticeable differences can be detected.
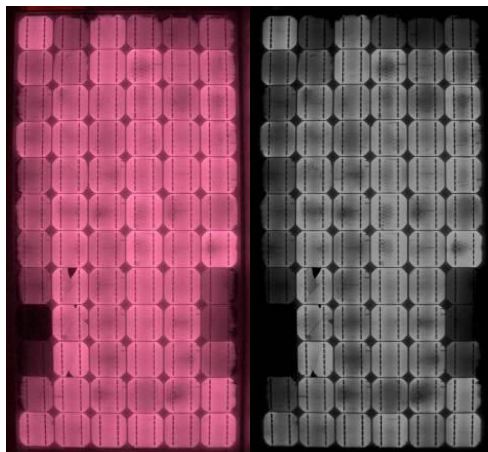
Figure 3-8: EL pictures of a PV module affected by PID using CCD (left) and InGaAs (right) sensors.

In Figure 3-9, the instruments used in this work to perform the EL test on the PV modules under analysis are shown.

(a)

(b)

Figure 3-9: IR camera, tripod (a) and power supply (b) used in the EL test.
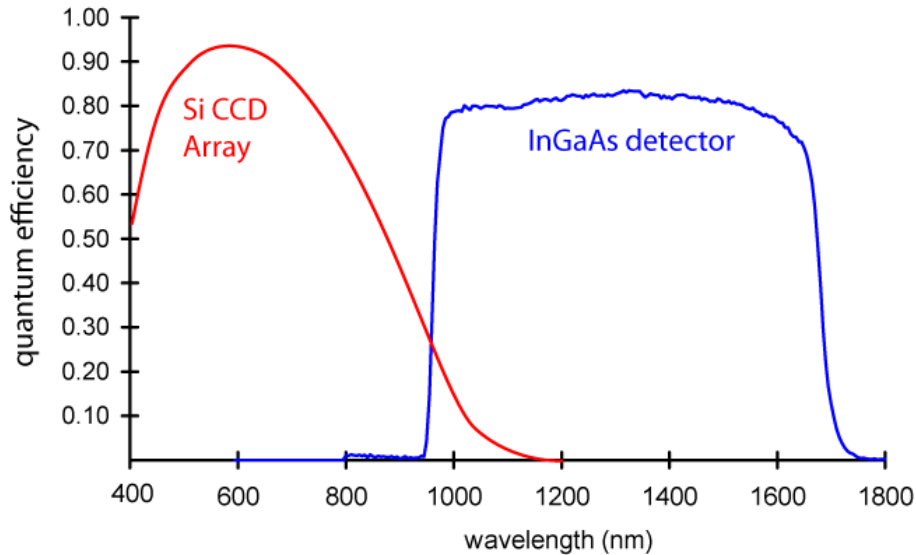
3.3.2 Results from the electroluminescence test

The pictures obtained with an EL analysis permit to detect defects due to issues in different stages of a PV module lifetime: manufacturing or assembly, transportation or installation, operation (external events after the installation), and maintenance. A description of the most common defects that can be detected by the EL test is reported below [47]:

- Micro-cracks can be generated during manufacturing, transportation and operation stages. The identification of the stage generating the cracks is not simple because their shape is similar and energy losses

depend on many factors [48]. However, most of cracks occur during the transportation and operation stages due to human (walkway on PV modules) or environmental causes (thermal stress, hail, storm and lightning).

- Broken cells due to mechanical or thermal stresses. These defects may be generated starting from single micro-cracks. Thus, parts of PV cells may be electrically isolated, reducing the current flowing in the cells.

- Impurities due to low quality manufacturing. A frequent case of impurity consists of non-uniform temperature distribution during the firing of the electric connections. Hence, parts of PV cells may have higher resistance, reducing the circulating current in the module.

- Potential Induced Degradation (PID) is a degradation of the *I-V* curve of the PV generator due to leakage currents in its frame. Generally, this defect is caused by these three driving factors: high voltage with respect to the ground and extreme environmental conditions, i.e., high temperature and high relative humidity. As a result, some PV cells may be electrically isolated, leading to high power losses.
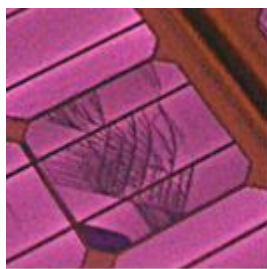
(a)
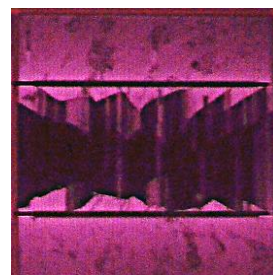
(b)
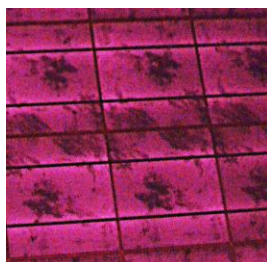
(c)

(d)

Figure 3-10: Most common defects detected by EL test: micro-cracks (a), broken cells (b), impurities (c), and PID (d).

Chapter 4

Innovative Procedure to Estimate PV Performance

In this part of the thesis, an innovative technique to predict the performance of PV modules in different weather conditions is presented. The performance of PV generators can be described using equivalent circuits characterized by a variable number of p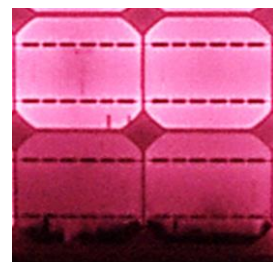arameters. Equivalent circuits may be defined by 3 (simplest circuit [12]), 4 [12], 5 [49], 7 [50] or more [51] parameters. Their knowledge permits to determine the *I-V* curve of PV generators for specific weather conditions. These quantities are affected by irradiance and temperature variations: thus, the knowledge of their dependence on these variables is fundamental to trace the *I-V* curve in any weather condition. The equations describing these dependences are known in literature. However, some of their coefficients are, generally, not provided [52]. This information can be found in some papers, but they refer to single PV cells [53]or to old PV modules [54], being not valid for the most recent generators. This technique aims to identify these coefficients to estimate the equivalent circuit parameters of the modules under test in any weather condition.

In this chapter, the procedure used to identify the coefficients of these optimized equations is presented, and it consists of four steps. First, the input data of the procedure, i.e., sets of acquired *I-V* curves from experimental campaigns, are properly filtered to exclude measurements affected by mismatch phenomena, shading, measurement errors or other issues. In the second step, the parameters of

an equivalent circuit are identified for each *I-V* curve using proper numerical algorithms. In the third step, the coefficients of optimized equations describing the dependence of each parameter on weather conditions are identified using non-linear regressions.

In the fourth step, the optimized equations are used to estimate the PV power and the energy generated in the experimental campaigns. These results are compared with the experiments and with the predictions by the most common model used in literature. In Figure 4-1, the flowchart of the methodology is reported.

Step #1
Data Preprocessing
Removal of measurements affected by mismatch phenomena, shading, measurement errors or other issues

Step #2
Parameters Extraction
Mixed analytical/numerical extraction of parameters for Single Diode Model

Step #3
Nonlinear Regression
Determination of coefficients for optimized equations

Step #4
Power and Energy Estimation
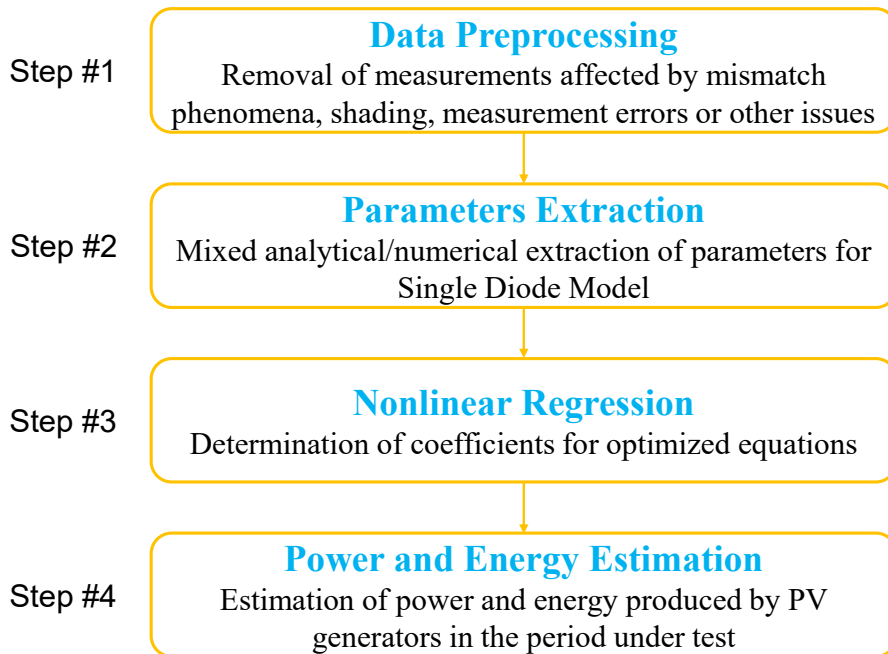Estimation of power and energy produced by PV generators in the period under test

Figure 4-1: Flowchart of the technique.

4.1 Step #1 - Filtering of measurements

In this step, different filters are applied to *I-V* curves from experiments to exclude the measurements affected by mismatch, shading, measurement errors or other issues. The GUI section dedicated to this step is presented in Figure 4-2.
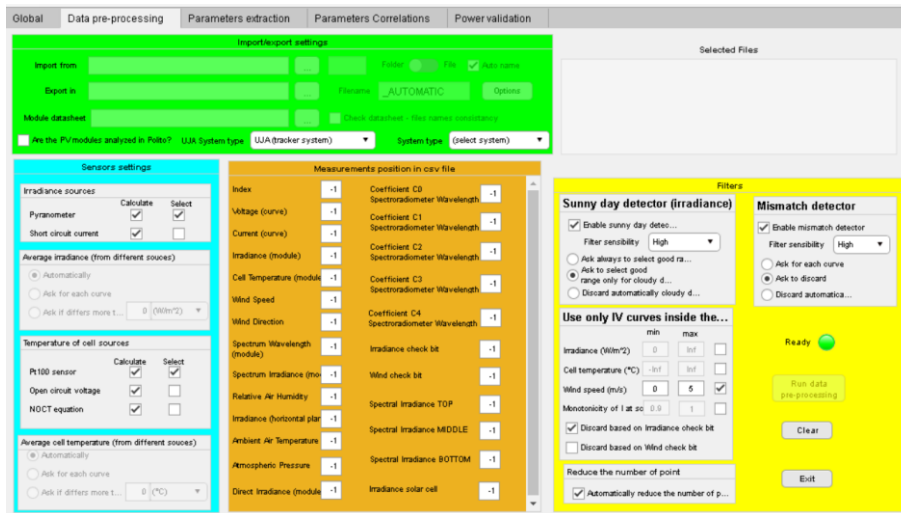
Figure 4-2: Section of the GUI dedicated to data preprocessing.

In particular, the following filters are applied:

1. *Removal of current peaks and fluctuations in the measured I-V curves*.
   In this work, the *I-V* curves of PV modules are traced by charging an external capacitive load. When the breaker of the circuit is closed, the capacitor is charged by the PV array from short-circuit to open-circuit conditions: the current and voltage signals are acquired during the transient. However, after the closing of the circuit, fast current peaks and fluctuations may occur with low voltage across the capacitor terminals due to the presence of parasitic capacitance at the junction of the solar cells. This part of the transient (generally, voltage < 5 V) is commonly excluded by next analyses, losing the information about this part of the *I-V* curve. This loss may be negligible if the capacitor is pre-charged with a negative voltage.
2. *Weighted reduction of experimental points*.
   According to the capacitor charging method, the distribution of experimental points is not uniform in the curve, and the highest density is in the neighbourhood of the open-circuit state. This condition may lower the performance of numerical algorithms processing such data. The algorithms adopted in this work aim to determine the parameters of an equivalent circuit to trace the *I-V* curves of PV modules. These methods may be forced by this points distribution to search for solutions optimized for the curve region with the highest points density (hence, close to the open circuit state). However, this region does not include the operating point of

the generator in normal conditions, i.e., its Maximum Power Point (MPP). Thus, it is suggested to adjust the points' distribution to force the algorithms to find optimal solutions in the neighbourhood of the MPP region. This filter performs this task by reducing the points distribution in the open circuit region. Moreover, the efficiency of the numerical algorithms may be improved by reducing the computational effort required for each curve.

3. *Mismatch filter*.
   This filter aims to remove the *I-V* curves affected by mismatch phenomena. First, the *I-V* and the power-voltage (*P-V*) curves are investigated to identify abrupt variations or multiple peaks, respectively. At a second stage, these curves in ideal conditions are estimated and their deviations from experimental data are quantified with the monotonicity index (I_{mon}), ranging between 0 and 1 (perfectly monotonic curve). The curves with the worst shape (monotonicity index lower than a threshold) are excluded from next analyses. The index I_{mon} is computed according to the following equation:

$$I_{mon} = \left| \sum_{k=1}^{N-1} \frac{f(I_{k+1} - I_k)}{N-1} \right|$$

$$f(I_{k+1} - I_k) = 1 \qquad if\ I_{k+1} > I_k$$

$$f(I_{k+1} - I_k) = 0 \qquad if\ I_{k+1} = I_k$$

$$f(I_{k+1} - I_k) = -1 \qquad if\ I_{k+1} < I_k \qquad (4\text{-}1)$$

where I_k and I_{k+1} are the kth and $(k+1)^{th}$ currents in the *I-V* curve, respectively, and N is the number of *I-V* points that each curve contains.

4. *Irradiance and wind speed filter*.
   This filter checks the variability of irradiance and wind speed during the acquisition. The irradiance is acquired at the beginning (G_{init}) and at the end (G_{end}) of the *I-V* curve measurement: if the difference $\Delta G = G_{init} - G_{end}$ exceeds a threshold (3% in this work), the curve is excluded from next analyses. Regarding wind speed, the curves are excluded in case of too high wind speed ($v_{wind} > 5$ m/s):

$$\Delta G / G_{init} > 3\%, v_{wind} > 5\ m/s \qquad (4\text{-}2)$$

4.2 Step #2 - Extraction of equivalent circuit parameters

The parameter extraction process consists of a numeric optimization to solve the transcendental equation of an equivalent circuit. An ad hoc developed Graphical User Interface (GUI) is adopted in this work to carry out the extraction with up to two different equivalent circuits and up to three different numerical algorithms. In this thesis work, results are obtained considering the Single Diode Model (SDM) and two numerical algorithms (the Levenberg-Marquardt, LM, and the Simulated Annealing/Nelder-Mead, SA-NM, algorithms). The section of the GUI dedicated to parameters extraction is presented in the next sections, as well as the detailed description of procedure.

4.2.1 Parameters extraction section in the GUI

Figure 4-4 shows the GUI section dedicated to the parameters extraction, which permits to define the main settings for the extraction procedure. These settings are grouped in the following six panels:

1. "Select extraction model". This panel permits to select the electrical equivalent circuit describing the performance of PV generators.
2. "Select extraction algorithm". This panel permits to select the optimization algorithms during the determination of the parameters.
3. "Test for the extraction reliability". This panel permits to filter the results according to three indicators, i.e., the maximum accepted error in the maximum power point, the maximum accepted Normalized Root Mean Square Error (*NRMSE*), and the range for acceptable parameters. The acceptance of the identified solutions can be automatic, semi-automatic (for curves not passing the test, a confirmation is asked to the user) or manual (the user decides whether to save the result of each curve). Moreover, a dedicated window displays the most important information related to the parameter extraction (the parameters, the *NRMSE*, and the *I-V* curve) for each measurement. Figure 4-3 presents the outputs for a generic curve: the results are not included in the range for acceptable parameters, and the user can discard or keep the result.
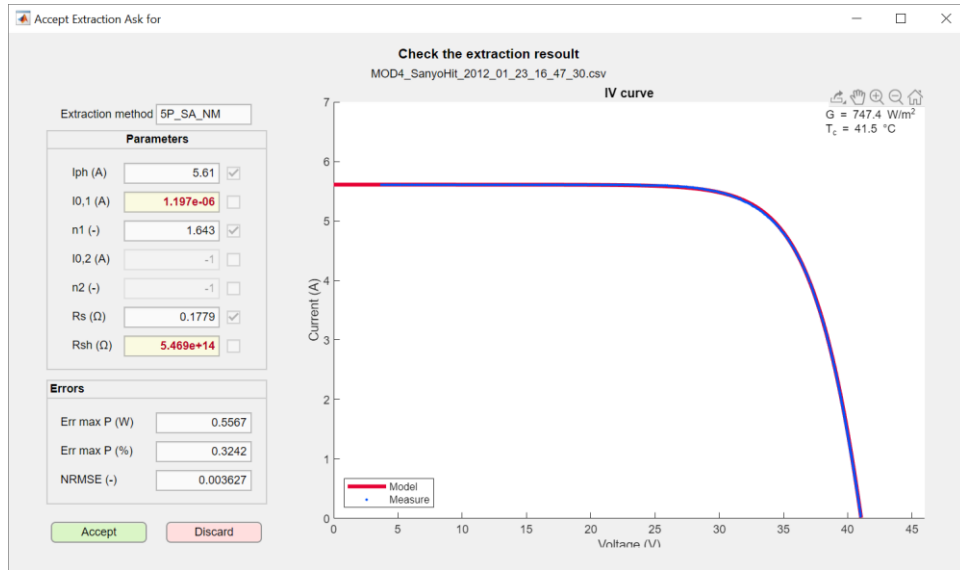
Figure 4-3: Outputs for a generic curve.

4. "Global Settings". In this panel, the most important boundary conditions for the extraction process are selected. The *I-V* curve of PV generators can be furtherly processed by reducing their number of experimental data. This operation may lead to faster convergence of numerical algorithms, as well as more accurate solutions. The GUI allows the user to reduce the number of points in the curves and to select the region of the curve in which it is convenient to carry out this reduction (short circuit, open circuit, or the entire curve). Moreover, a first estimation of the resistances R_s and R_{sh} may be evaluated starting from the *I-V* curve. This may be important to validate the parameters determined by the algorithms. This panel permits also to select the interval of the curve in which this estimation is carried out.

5. "Algorithm Settings". This panel contains the most important settings for the numerical algorithms adopted in the analysis: the maximum number of iterations per extraction and their tolerance.

6. "Model Settings". This panel permits to select, for each parameter and for the equivalent circuits under use, their acceptability range.

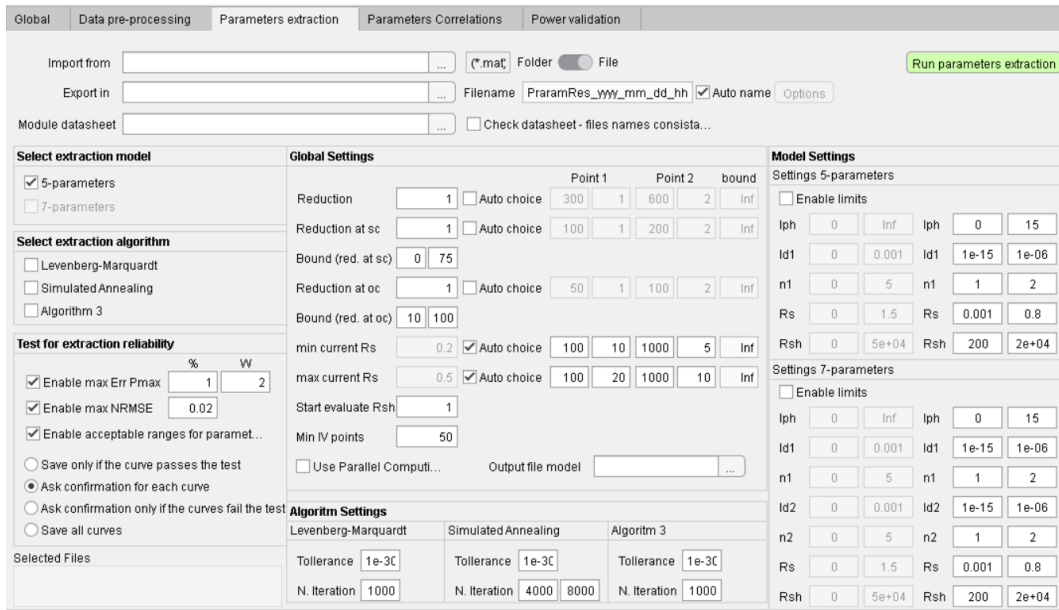Figure 4-4: Section of the GUI dedicated to parameters extraction step.

4.2.2 Procedure for Parameters Extraction

The flowchart in Figure 4-5 shows the procedure used to determine the parameters of the equivalent circuit. First, the acceptable range of the parameters is set. Then, the main constraints of the numerical problem are identified (the maximum number of iterations and the optimization tolerance). Then, the initial values of the parameters are evaluated using an analytical model. Starting from these values, the parameters of the equivalent circuit are identified using a numerical algorithm, and their deviation from measurements is assessed calculating a quadratic error. In case of too high errors, the *I-V* curve is discarded and excluded from next analyses. In this section, the steps 2c-2e will be described in detail.
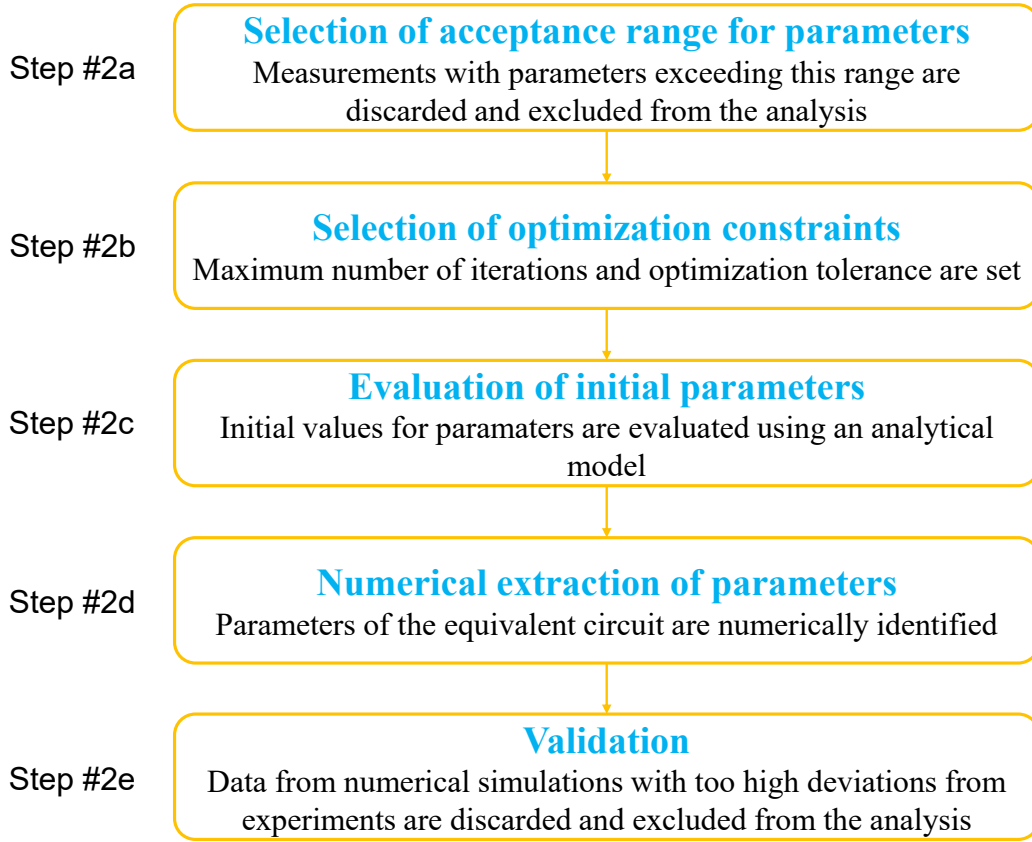
Step #2a	**Selection of acceptance range for parameters** Measurements with parameters exceeding this range are discarded and excluded from the analysis
Step #2b	**Selection of optimization constraints** Maximum number of iterations and optimization tolerance are set
Step #2c	**Evaluation of initial parameters** Initial values for paramaters are evaluated using an analytical model
Step #2d	**Numerical extraction of parameters** Parameters of the equivalent circuit are numerically identified
Step #2e	**Validation** Data from numerical simulations with too high deviations from experiments are discarded and excluded from the analysis

Figure 4-5: Scheme of the parameters extraction procedure.

Evaluation of initial parameters

The convergence of the adopted numerical algorithms is strongly affected by the initial values of the variables: actually, if the initial values of the parameters are far from their optimized value, some numerical methods may diverge, obtaining unrealistic solutions [55,56]. Hence, the evaluation of the initial parameters is fundamental: in this work, they are evaluated using an analytical procedure according to [57] and its scheme is presented in Figure 4-6.

This method is iterative, and it starts from the knowledge of some quantities from the experiments (G, T_c, I_{sc}, V_{oc}, V_M, I_M). The initial photovoltaic current I_{ph} can be derived by the following equations.

In the short-circuit point, i.e. $(V, I) = (0, I_{sc})$:

$$I_{sc} = I_{ph} - I_0 \cdot \left(e^{\left(\frac{R_S \cdot I_{sc}}{V_t \cdot n \cdot N_s} \right)} - 1 \right) - \frac{R_S \cdot I_{sc}}{R_{sh}} \tag{4-3}$$
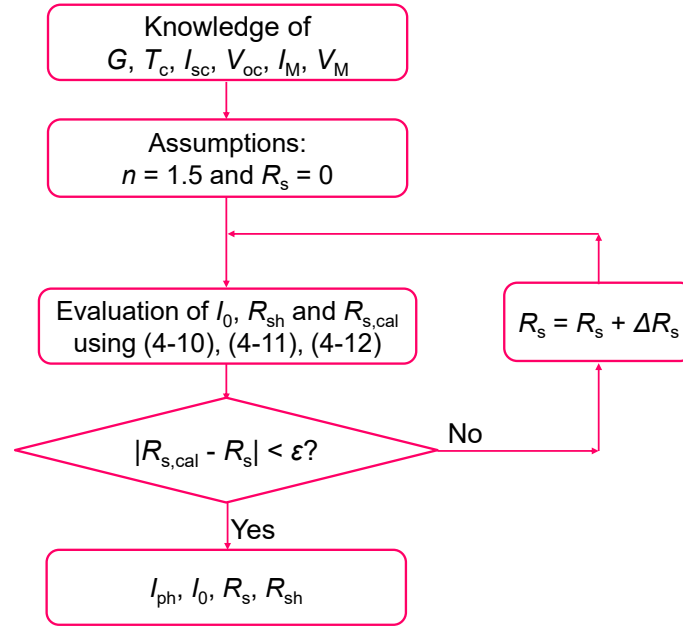
Figure 4-6: Scheme of the analytical procedure to estimate initial parameters.

In the open-circuit point, i.e. $(V, I) = (V_{oc}, 0)$:

$$0 = I_{ph} - I_0 \cdot \left(e^{\left(\frac{V_{oc}}{V_t \cdot n \cdot N_S} \right)} - 1 \right) - \frac{V_{oc}}{R_{sh}} \tag{4-4}$$

In the maximum power point, i.e. $(V, I) = (V_M, I_M)$:

$$I_M = I_{ph} - I_0 \cdot \left(e^{\left(\frac{R_S \cdot I_M + V_M}{V_t \cdot n \cdot N_S} \right)} - 1 \right) - \frac{R_S \cdot I_M + V_M}{R_{sh}} \tag{4-5}$$

where V_t is the thermal voltage, and it is the ratio between two terms: the product between the Boltzmann constant ($k_B = 1.38 \cdot 10^{-23}$ J/K) and the cell temperature T_c, and the electron charge ($q_e = 1.6 \cdot 10^{-19}$ C).

The photovoltaic current can be estimated starting from equations (4-1) and (4-2) in the following way:

$$I_{ph} = I_0 \cdot \left(e^{\left(\frac{V_{oc}}{V_t \cdot n \cdot N_S} \right)} - 1 \right) + \frac{V_{oc}}{R_{sh}} \tag{4-6}$$

Moreover, three additional quantities are calculated to evaluate the initial values of the other parameters according to the following equations:

$$X_{sc} = e^{\left(\frac{R_S \cdot I_{SC}}{V_t \cdot n \cdot N_s}\right)} \tag{4-7}$$

$$X_{oc} = e^{\left(\frac{V_{oc}}{V_t \cdot n \cdot N_s}\right)} \tag{4-8}$$

$$X_M = e^{\left(\frac{V_M + R_S \cdot I_M}{V_t \cdot n \cdot N_s}\right)} \tag{4-9}$$

The saturation current I_0 and the shunt resistance R_{sh} can be estimated with the iterative process presented in [57] by the following equations:

$$I_0 = \frac{I_{sc} \cdot (V_M - V_{oc}) + V_{oc} \cdot I_M}{V_M \cdot (X_{oc} - X_{sc}) - V_{oc} \cdot (X_M - X_{sc})} \tag{4-10}$$

$$R_{sh} = \frac{V_{oc} \cdot (X_M - X_{sc}) - V_M \cdot (X_{oc} - X_{sc})}{I_{sc} \cdot (X_M - X_{oc}) + I_M \cdot (X_{oc} - X_{sc})} \tag{4-11}$$

The series resistance is analytically computed at each iteration ($R_{s,cal}$) and it is compared with the R_s value. At the beginning of the procedure, this quantity is null, and it is increased with a step of 10^{-5} after each iteration. The iterative process stops when the deviation between these two values is sufficiently low. The analytical equation to evaluate this parameter can be derived from (4-5):

$$R_{s,cal} = \frac{V_M}{I_M} - \frac{1}{\left(\frac{I_0}{n \cdot N_s \cdot V_M} \cdot X_M + \frac{1}{R_{sh}}\right)} \tag{4-12}$$

At this stage, the parameter n is supposed constant and equal to 1.5. This assumption is valid because the n value, generally, ranges between 1 and 2 for the SDM.

Numerical extraction of parameters

As previously stated, many numerical approaches address the problem of parameters extraction for PV modules. In this thesis work, two different methods (the Levenberg Marquardt algorithm and a combination of the Simulated Annealing and of the Nelder Mead techniques) are implemented, and their results are compared in terms of accuracy and computational effort. These algorithms use different forms of the transcendental equation describing the *I-V* curve as a function of the five parameters for the single diode model. In particular, the Levenberg

Marquardt algorithm solves the explicit form of the transcendental equation using the Lambert W-function. This approximation increases the efficiency of the algorithm, i.e., the number of iterations required to find the solution is reduced, as well as the computational cost. The explicit equation solved by LM is the following:

$$I = -\frac{V}{R_s+R_{sh}} - \frac{W\left(R_s \cdot I_0 \cdot R_{sh} e^{\left(\frac{R_{sh} \cdot \left(R_s \cdot I_{ph} + R_s \cdot I_0 + V\right)}{n \cdot V_{th} \cdot (R_s + R_{sh})}\right)}\right) n \cdot V_{th}}{R_s} + \frac{R_{sh} \cdot \left(I_0 + I_{ph}\right)}{R_s+R_{sh}} \qquad (4\text{-}13)$$

where $W(z)$ is the Lambert W function of the element z such as $z = W(z) \cdot e^{W(z)}$.

On the contrary, the SM/NM method solves the implicit formulation of the transcendental equation, as described in Section I. However, both the algorithms determine the set of parameters by minimizing a proper objective function F, which is computed as the following current difference:

$$F(\theta) = \sum_{i=1}^{N}\left(I_{i,exp} - I_{i,mod}\left(V_{i,exp}, \theta\right)\right)^2 \qquad (4\text{-}14)$$

where θ is the generic set of parameters (I_{ph}, I_0, n, R_s, R_{sh}), $I_{i,exp}$ is the current value for the ith point of the I-V curve from experiments, and $I_{i,mod}$ is the corresponding current evaluated by the model using the parameters set θ. Finally, a tolerance of 10^{-30} and a minimum number of iterations of 1000 (LM) and 12000 (SA/NM) are set to guarantee the convergence of the algorithms. The latter parameter is different according to the adopted technique because, despite the LM algorithm is able to identify the solution in a shorter number of iterations, the computational cost of each iteration is higher than the SA/NM.

The performance of the algorithms is estimated by calculating two indicators: the Normalized Root Mean Square Error (*NRMSE*) of each *I-V* curve estimated using the parameters, and the error at the Maximum Power Point (MPP).

The first indicator is defined as follows:

$$NRMSE = \frac{\sqrt{\frac{\sum_{i=1}^{N}\left(I_{i,mod} - I_{i,exp}\right)^2}{N}}}{\frac{\sum_{i=1}^{N} I_{i,exp}}{N}} \cdot 100 \qquad (4\text{-}15)$$

On the contrary, the error in the MPP computes the percentage deviation between the maximum power from the model ($P_{M,mod}$) and from experiments ($P_{M,exp}$).

4.3 Step #3 - Nonlinear regressions

This step of the analysis aims to identify the dependence of each parameter on irradiance and temperature. Some equations are presented in literature: however, despite their structure is qualitatively known, the values of some coefficients in the equations are not provided. In this work, equations from [12] are selected and the adopted GUI performs nonlinear optimizations to fit experimental data. In Figure 4-7, the section of the GUI dedicated to this step is shown. This part of the software permits to select the dataset of parameters to process. Moreover, data may be filtered by selecting restricted irradiance and cell temperature ranges.
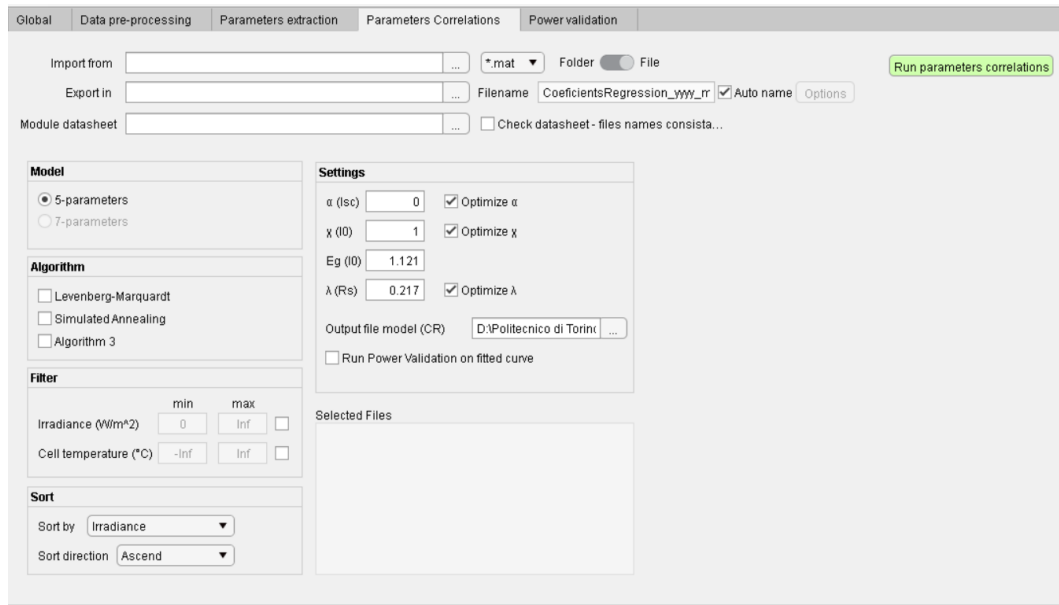
Figure 4-7: Section of the GUI dedicated to nonlinear regression step.

4.3.1 Photogenerated current

The photogenerated current I_{ph} has a proportional dependence on irradiance G and a linear dependence on temperature T_c according to [12]:

$$I_{ph} = \mathbf{\textcolor{green}{I_{ph,STC}}} \cdot \left[1 + \alpha \cdot \left(T_c - T_{c,STC}\right)\right] \cdot \frac{G}{G_{STC}} \qquad (4\text{-}16)$$

where $I_{ph,STC}$ is the coefficient to be optimized, being the photogenerated current at STC conditions. The temperature coefficient α may be optimized as well or the value from the manufacturer datasheet may be assumed. In this thesis, the value provided by the manufacturer is assumed.

5.3.2 Reverse saturation current

The reverse saturation current I_0 has a cubic proportionality and exponential behaviour with respect to the temperature and it is affected by the energy gap of PV technology. It depends on temperature and the quantities $E_g(T_c)$ and $E_{g,STC}$ are the energy gaps evaluated at temperature T_c, and at STC conditions, respectively [12]. Generally, the latter corresponds to $1.121 \cdot q_e$ J for Si cells:

$$I_0 = I_{0,STC} \cdot \left(\frac{T_c}{T_{c,STC}}\right)^3 \cdot \exp\left(\left(\frac{E_{g,STC}}{T_{STC}} - \frac{E_g(T_c)}{T_c}\right) \cdot \frac{1}{k_B}\right)$$

$$\text{With } E_g(T_c) = E_{g,STC} \cdot \left(1 - 0{,}0002677 \cdot \left(T_c - T_{c,STC}\right)\right) \qquad \text{(4-17)}$$

4.3.3 Diode ideality factor

In literature, the dependence of the diode ideality factor on temperature and irradiance is not unique and, in most of cases, constant values of n are considered. In this work, a linear proportionality with the two weather parameters is supposed:

$$n = a + b \cdot G + c \cdot T_c \qquad \text{(4-18)}$$

where the optimization coefficients are a (adimensional), b (expressed in m^2/W) and c (expressed in 1/K).

4.3.4 Series resistance

The series resistance is proportional to temperature and has a logarithmic dependence on irradiance:

$$R_s = R_{s,STC} \cdot \frac{T_c}{T_{c,STC}} \cdot \left(1 - \lambda \cdot \log\left(\frac{G}{G_{STC}}\right)\right) \qquad \text{(4-19)}$$

The series resistance at STC conditions is optimized ($R_{s,STC}$), as well as an adimensional coefficient quantifying the dependence on irradiance (λ).

4.3.5 Shunt resistance

The shunt resistance is inversely proportional to irradiance only and the optimization coefficient is the shunt resistance at STC conditions $R_{sh,STC}$:

$$R_{sh} = \mathbf{R_{sh,STC}} \cdot \frac{G_{STC}}{G} \tag{4-20}$$

The quality of the nonlinear regressions for the different parameters is quantified by evaluating their *NRMSE*. This quantity (*NRMSE*$_X$) is calculated for the five parameters in the following way:

$$NRMSE_X = \frac{\sqrt{\frac{\sum_{i=1}^{N}(X_{eq} - X_{exp})^2}{N}}}{\frac{\sum_{i=1}^{N} X_{exp}}{N}} \cdot 100 \tag{4-21}$$

where X_{exp} is the generic parameter numerically determined from experiments, X_{eq} is the generic parameter estimated in the same weather condition using the optimized equations, and N is the number of measurements.

4.4 Step #4 - Power and energy estimation

The fourth step of the procedure consists of using the optimized equations to evaluate, for each weather condition (irradiance and temperature) from the experimental campaign, the maximum PV power and the generated energy in the campaign. These quantities are compared with the experimental data and with the prediction by the most common model used in literature, the Osterwald Model (OM) [58,59]. This model permits to assess the PV power in the maximum power point starting from the knowledge of the rated PV power P_{STC} and the temperature coefficient for power γ:

$$P_M = P_{STC} \cdot \frac{G}{G_{STC}} \cdot \left(1 + \frac{\gamma}{100} \cdot \left(T_c - T_{c,STC}\right)\right) \tag{4-22}$$

The effectiveness of the power estimation is quantified by evaluating two *NRMSEs*: one between the experimental power and the predictions by the optimized equations, and the other between experimental power and OM power:

$$NRMSE_P = \frac{\sqrt{\frac{\Sigma_{i=1}^{N}\left(P_{i,mod}-P_{i,exp}\right)^2}{N}}}{\frac{\Sigma_{i=1}^{N}P_{i,exp}}{N}} \cdot 100 \qquad (4\text{-}23)$$

where $P_{i,exp}$ is the power from experiments, while $P_{i,mod}$ is the power predicted by the optimized equations or OM in the same weather condition, and N is the number of measurements. Moreover, the energy generated during the experimental campaign is assessed by assuming the power constant during a time interval of 1 min. The deviations between the measurements and the predictions by the models are calculated as follows:

$$Err_E = \frac{E_{exp}-E_{mod}}{E_{exp}} \cdot 100 \qquad (4\text{-}24)$$

where E_{exp} is the experimental energy and E_{mod} is the energy computed by the optimized equations or OM. The section of the GUI performing this step is shown in Figure 4-8.
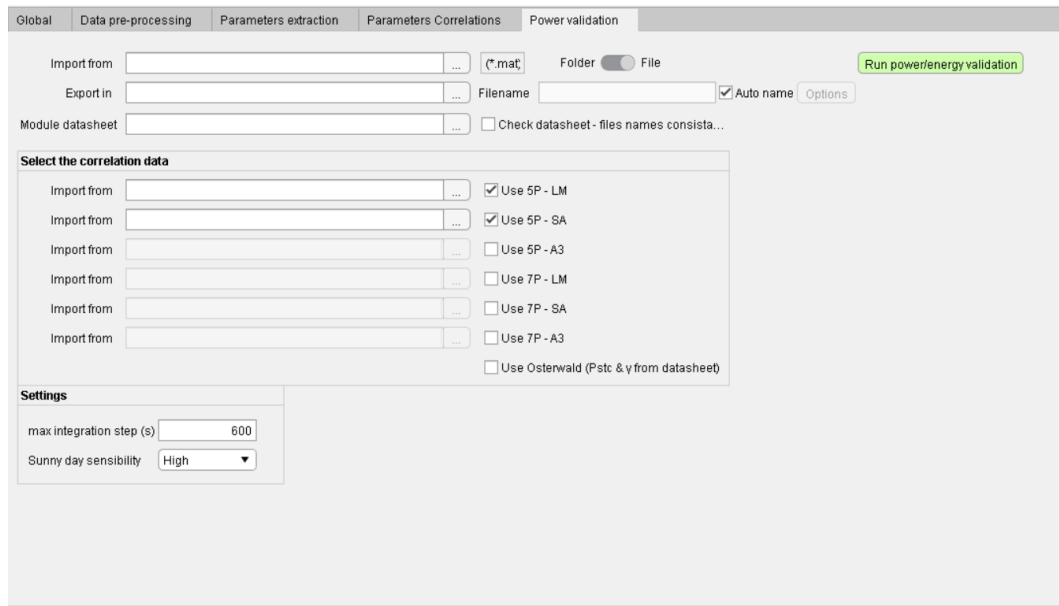
Figure 4-8: Section of the GUI dedicated to power and energy estimation.

Chapter 5

PV Modules under Test

PV modules with the most diffused technologies were subject to experimental campaigns with different duration and measurement systems. This activity has been performed in collaboration with the University of Jaén. PV modules from #1 to #3 were tested in Jaén (Spain), while the others (#4 - #7) were tested at Politecnico di Torino (Turin, Italy). PV generators measured in Spain (images in Figure 5-1) were calibrated before the start of the experimental campaign by the laboratory of the Centro de Investigaciones Energéticas, MedioAmbientales y Tecnológicas (CIEMAT) in Madrid (Spain), and their *I-V* curves in STC conditions were investigated in order to verify their state of health.

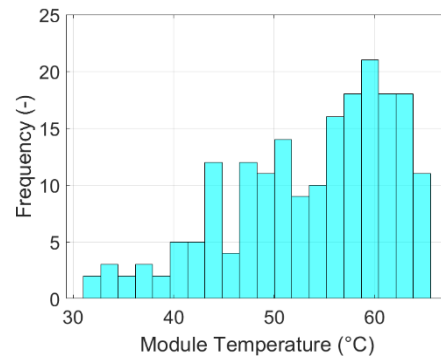Module #1   Module #2   Module #3

Figure 5-1: Images of the PV modules tested in Spain in visible light.

The specifications of these modules are presented in Table 1.

Table 1: Electrical specifications of the modules tested in Spain

Module ID	#1	#2	#3
Manufacturer	Kyocera	Luxor	Sharp
PV technology	p-Si	m-Si	m-Si
P_{nom}	135 W	100 W	245 W
η_{STC}	13.5 %	15.5 %	14.9 %
V_{oc}	22.1 V	21.6 V	37.5 V
I_{sc}	8.37 A	5.87 A	8.73 A
α	0.06 %/K	0.05 %/K	0.05 %/K
β	-0.36 %/K	-0.35 %/K	-0.347 %/K
Power Tolerance	(-5%, +5%)	(0, +5%)	(-5%, +10%)

The power deviations with respect to the manufacturer declaration were in the range including the manufacturer tolerance (Table 2). Moreover, the *I-V* curves did not present noticeable issues.

Table 2: Power deviations with respect to manufacturer specifications (modules tested in Spain)

Module ID	#1	#2	#3
Power Deviation	+4.52%	-0.82%	-0.65%

On the contrary, PV modules from #4 to #7 were tested in Italy. Similarly to the other generators, the power deviations with respect to the manufacturer data and their *I-V* curve were investigated to exclude the presence of faults or defects in the modules. For this reason, they were tested outdoor with the calibrated measurement

system described in Section 4.1 and subject to an EL test in a dark laboratory. The specifications of these modules are listed in Table 3.

Table 3: Electrical specifications of the modules tested in Italy

Module ID	#4	#5	#6	#7
Manufacturer	JA Solar	LG	JA Solar	REC
PV technology	m-Si	m-Si	p-Si	p-Si
P_{nom}	310 W	370 W	280 W	285 W
η_{STC}	19 %	21.4 %	17.1 %	17.1 %
V_{oc}	40.3 V	42.8 V	38.65 V	38.6 V
I_{sc}	9.91 A	10.82 A	9.37 A	9.66 A
α	0.06 %/K	0.04 %/K	0.058 %/K	0.066 %/K
β	-0.3 %/K	-0.24 %/K	-0.33 %/K	-0.3 %/K
Power Tolerance	(0, +5W)	(0, +3%)	(0, +5W)	(0, +5W)

The power deviations with respect to manufacturer declaration are in the range including the manufacturer tolerance and the uncertainty of the measurement system (Table 4).

Table 4: Power deviations with respect to manufacturer specifications (modules tested in Italy)

Module ID	#4	#5	#6	#7
Power Deviation	-3.10%	-2.60%	-3.40%	-4.40%

Regarding the EL images (Figure 5-2), no noticeable issues are detected. In the picture of module #7, some black signs can be noticed but they do not impact on energy production according to the *I-V* curve tracing.

| Module #4 | Module #5 | Module #6 | Module #7 |

(a)

(b)
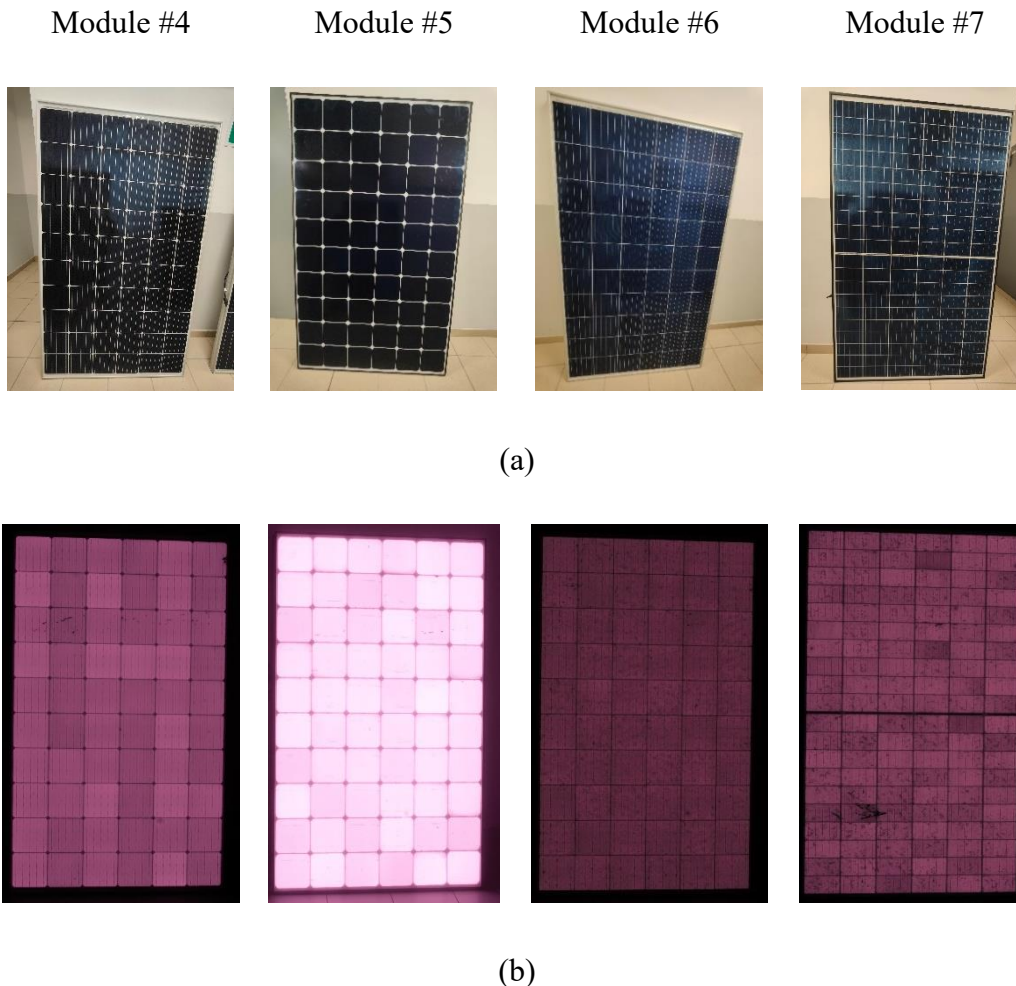
Figure 5-2: Images of the PV modules tested in Italy in visible light (a) and under EL test (b).

5.1 Experimental campaign in Spain

In Figure 5-3, the distribution of irradiance (yellow bars) and module temperature (blue bars) for the modules tested in Spain (#1 - #3) are presented. This experimental campaign was carried out in 2021 from April to June, measuring a total of 196, 198, and 87 *I-V* curves for modules #1 - #3, respectively. The campaign was conducted to measure the PV modules in a wide range of irradiance and cell temperature (from 100 to 1000 W/m^2 and from 25 to 70 °C, respectively).
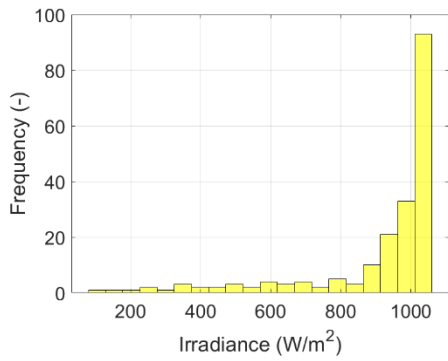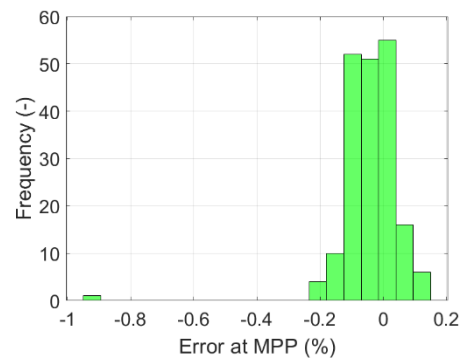
Module #1
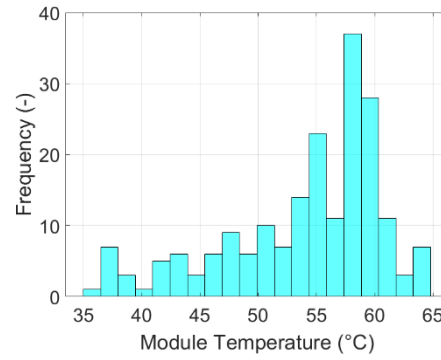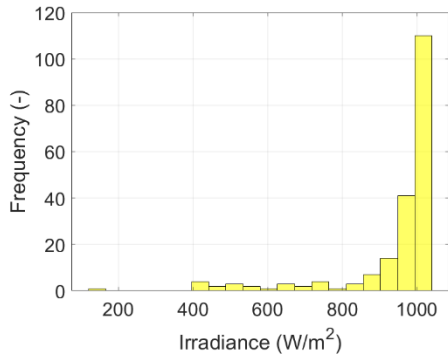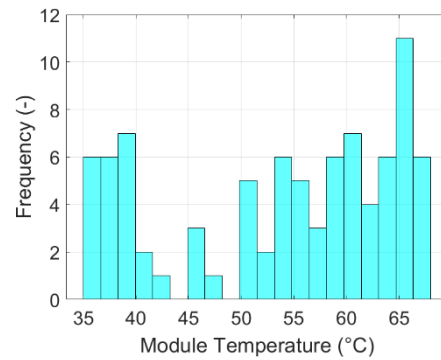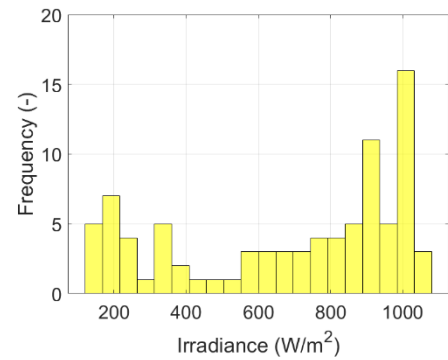
Module #2

Module #3

Figure 5-3: Irradiance and module temperature distribution for modules tested in Spain.

Most of acquisitions was performed above 800 W/m^2 due to the mechanical sun tracking system. Nevertheless, the number of measurements at lower irradiance are sufficient to obtain results valid for the irradiance range 400 W/m^2−1000 W/m^2.

5.2 Experimental campaign in Italy

In Figure 5-4, the distribution of irradiance (yellow bars) and module temperature (blue bars) for the modules tested in Italy (#4 - #7) are reported. This experimental campaign was carried out in 2021 from February to June, measuring a total of 86, 65, 109 and 114 *I-V* curves for modules #4 - #7, respectively. PV modules were measured in a wide range of irradiance and cell temperature (from 100 to 1000 W/m^2 and from 25 to 60 °C, respectively). Comparing the data with the Spanish campaign, the shape of each *I-V* curve was checked after the acquisition to exclude measurements affected by mismatch or other issues before being stored.
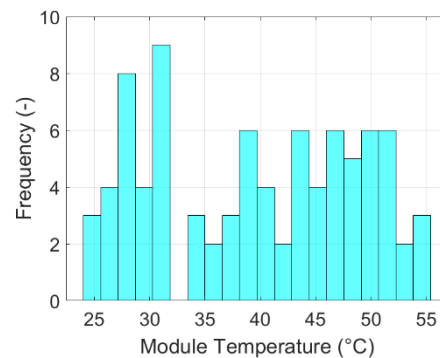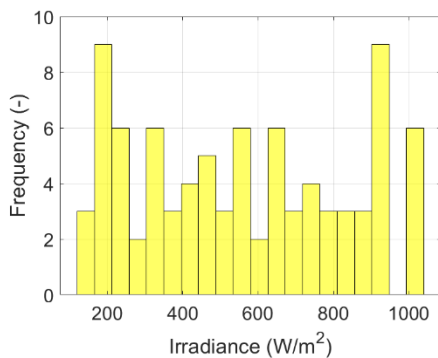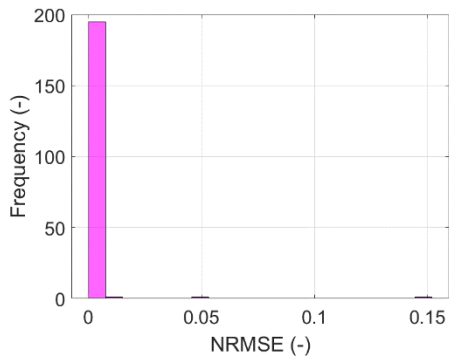

Module #4
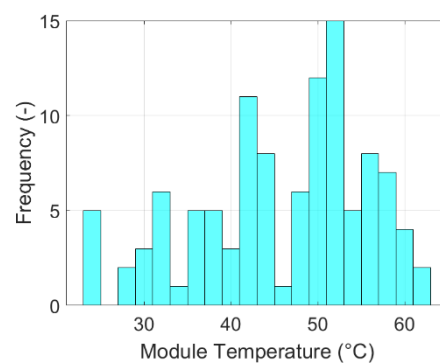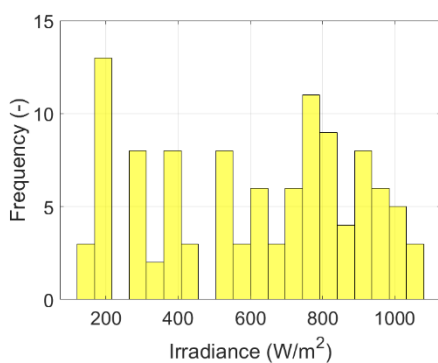
Module #5
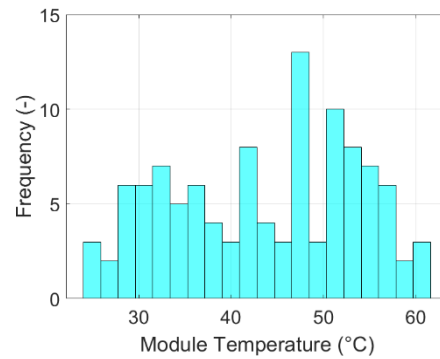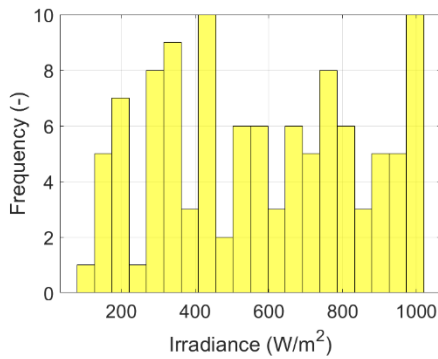
Module #6
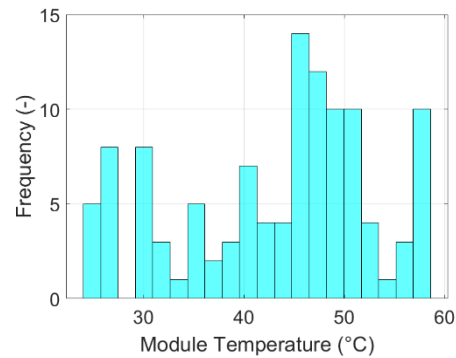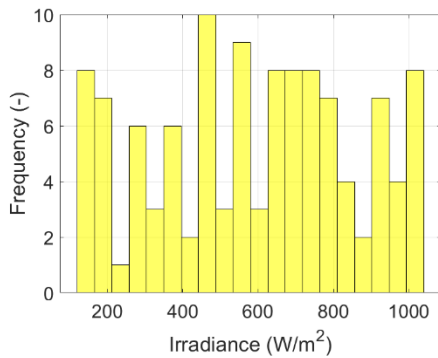
Module #7

Figure 5-4: Irradiance and module temperature distribution for modules tested in Italy.
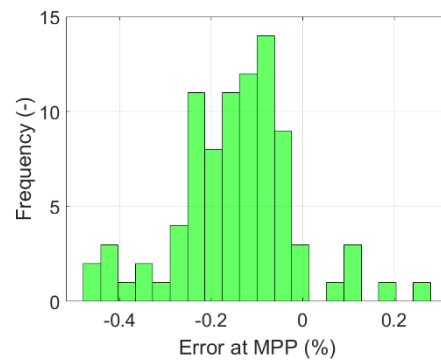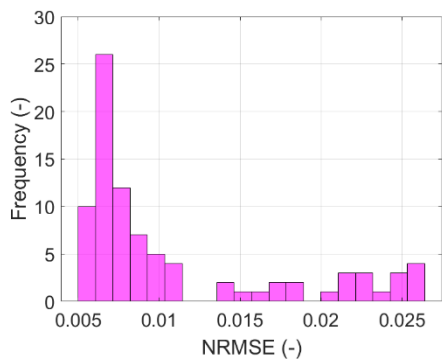
5.3 Parameters extraction for modules tested in Spain

The extraction of the equivalent circuit parameters was performed using two optimization methods. The first method was based on the Levenberg Marquardt algorithm, while the second one was based on a combination of two algorithms, the Nelder Mead and the Simulated Annealing algorithms. From the comparison between the two methods, the second (NM/SA) is the best because its computational cost is lower and the NRMSEs are lower than the LM method. Thus, the results of this method are reported only. This section presents the main results of the parameters extraction for the modules tested in Spain (#1 – #3). Figure 5-5 presents the distribution charts of the *NRMSE* and the error at the maximum power point for the *I-V* curves traced using the five parameters of the equivalent circuit.
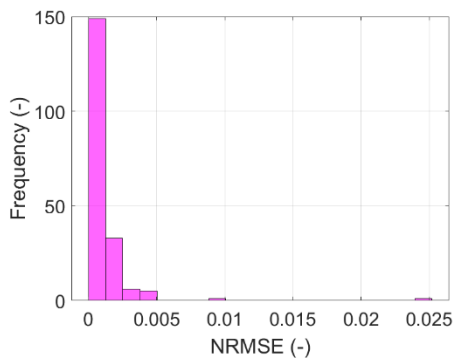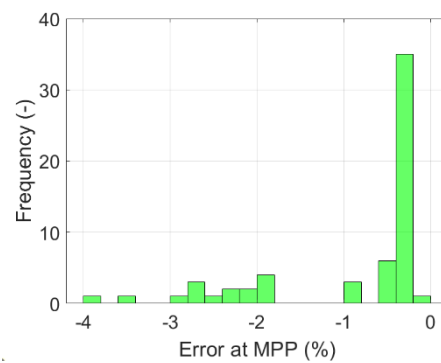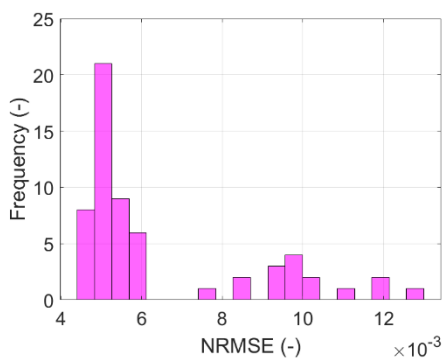
Module #1
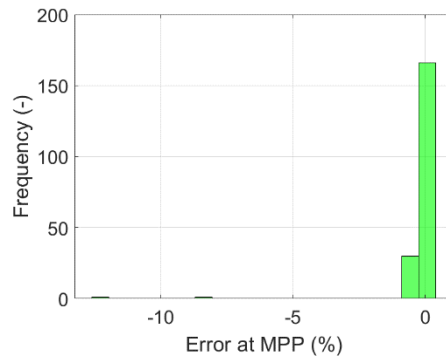
Module #2

Module #3

Figure 5-5: NRMSE and error at MPP distribution for modules tested in Spain.
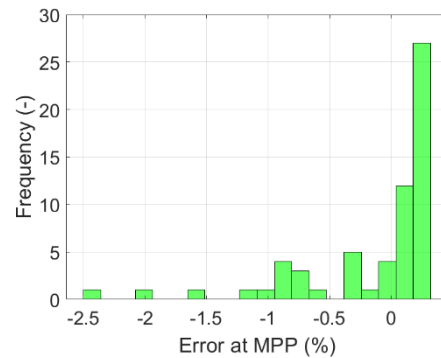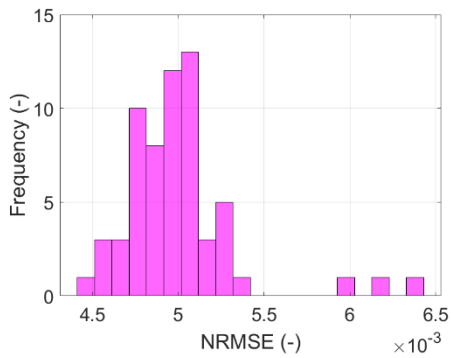
The charts show that the numerical extraction properly performed, obtaining most of NRMSEs < 10^{-2} and most of the errors at the MPP < 0.5%.

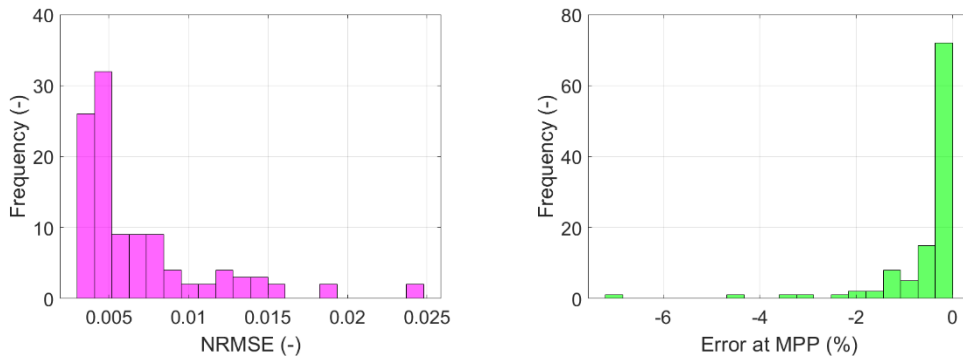## 5.4 Parameters extraction for modules tested in Italy

This section presents the main results of the parameters extraction for the modules tested in Turin (#4 – 7#). Figure 5-6 presents the distribution charts of the NRMSE and the error at the maximum power point for the *I-V* curves traced using the five parameters of the equivalent circuit.
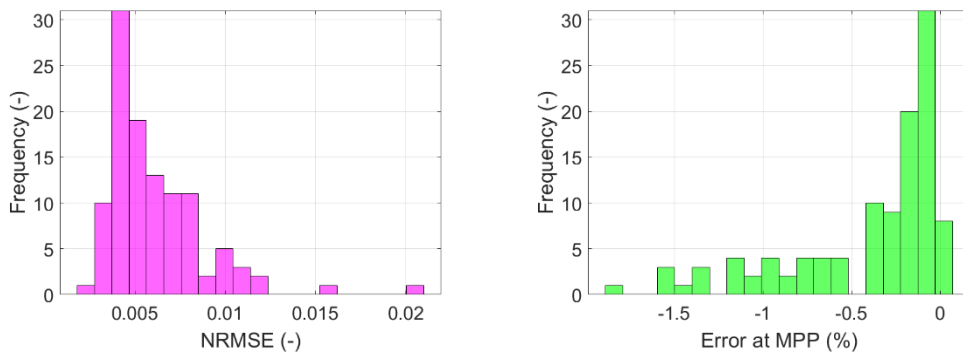

Module #4

Module #5

Module #6

Module #7

Figure 5-6: NRMSE and error at MPP distribution for modules tested in Turin.

The charts show that the numerical extraction properly performed, obtaining most of *NRMSEs* < 10^{-2} and most of the errors at the MPP < 1%. Moreover, the *NMRSEs* obtained in Italy are lower with respect to the modules tested in Spain.

Chapter 6

Results

The results of the tested PV modules will be presented in this chapter. Firstly, the results of the nonlinear regressions will be presented, as well as the optimized equations describing the dependence of each parameter on irradiance and module temperature. As previously described, some parameters are affected by one of the two quantities only (the reverse saturation current by temperature, and the shunt resistance by irradiance). The figures used to describe the dependence of the other three parameters are 2D graphs in which both independent variables (irradiance and module temperature) vary. In the appendix, the 3D plots for the equivalent circuit's parameters depending on irradiance and temperature both are reported for one PV module. The red dots of the figures in this chapter are the parameters numerically determined from experiments, while the blue curves present the parameters estimated using the optimized equations in the whole irradiance and temperature range. The dependence of photogenerated current with respect to irradiance is stronger than temperature: thus, the figure describing its dependence on irradiance is presented only. In numerical extractions, the shunt resistance tends to be unrealistic, and, in literature, many models deal with four parameters only, excluding this parameter. In addition, its influence in the *I-V* equation is almost negligible [60]. In this work, in case of unrealistic values, R_{sh} is assumed constant and equal to its mean value. In this situation, the figure describing its evolution with respect to irradiance is omitted. Moreover, the results regarding the energy estimation step and the comparison with the experimental data, as well as with the Osterwald model, are commented. Finally, the last section reports a future application of this work in the context of automatic fault detection in PV systems.

6.1 Experimental data and fitting equations for the 5 parameters of module #1

This subsection presents the optimized equations describing each parameter as a function of irradiance and temperature for module #1.

6.1.1 Photogenerated current

The dependence of the photogenerated current on irradiance is presented in Figure 6-1, while its optimized equation is the following:

$$I_{ph} = \mathbf{8.64} \cdot \left[1 + \alpha \cdot \left(T_c - T_{c,STC}\right)\right] \cdot \frac{G}{G_{STC}}$$

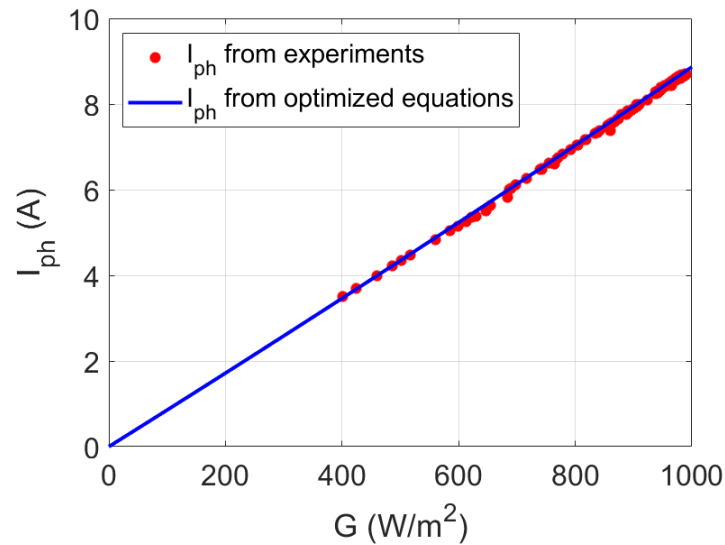

Figure 6-1: I_{ph} as a function of irradiance for module #1.

6.1.2 Reverse saturation current

The dependence of the reverse saturation current on temperature is presented in Figure 6-2, while its optimized equation is the following:

$$I_0 = \mathbf{8.90 \cdot 10^{-9}} \cdot \left(\frac{T_c}{T_{c,STC}}\right)^3 \cdot \exp\left(\left(\frac{E_{g,STC}}{T_{STC}} - \frac{E_g(T_c)}{T_c}\right) \cdot \frac{1}{k_B}\right)$$
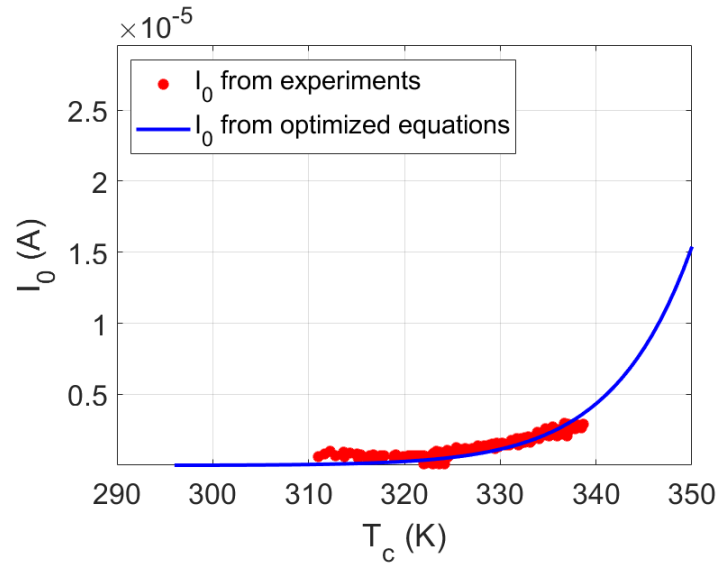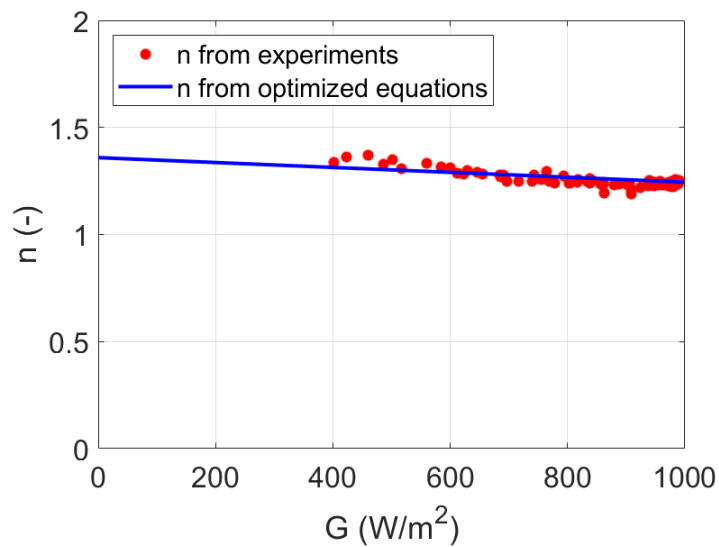
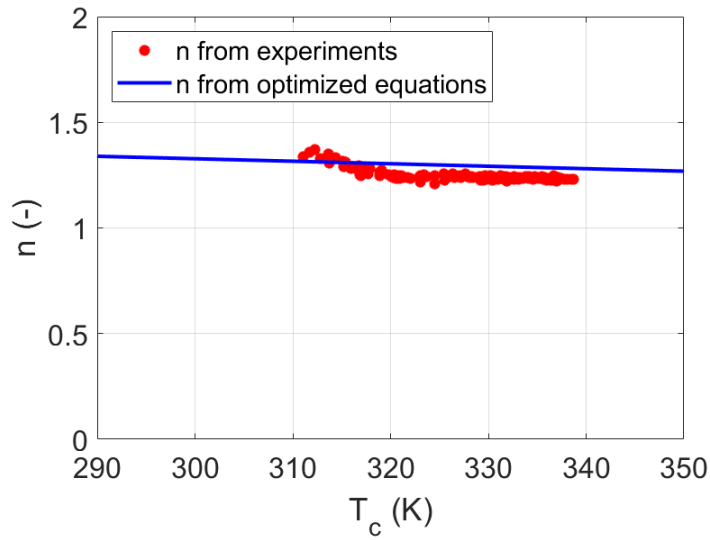Figure 6-2: I_0 as a function of temperature for module #1.

6.1.3 Diode ideality factor

The dependence of the diode ideality factor on irradiance and temperature is presented in Figure 6-3, while its optimized equation is the following:

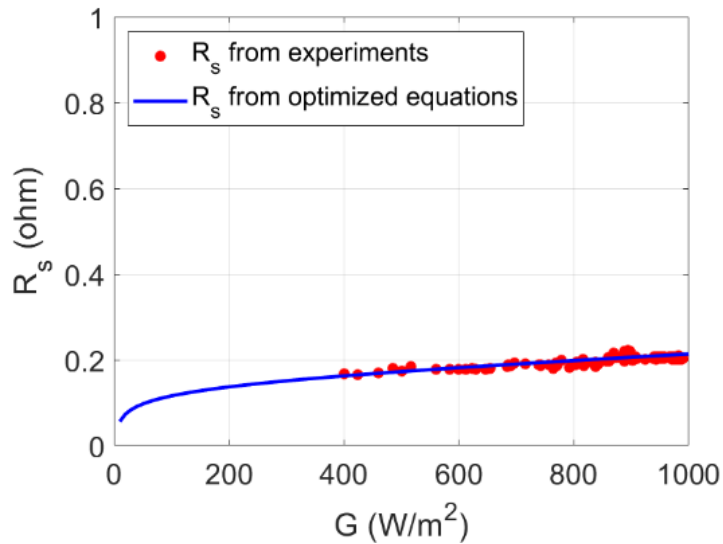$$n = \mathbf{0.80 - 2.57 \cdot 10^{-4}} \cdot G + \mathbf{2.03 \cdot 10^{-3}} \cdot T_c$$

(a)

(b)

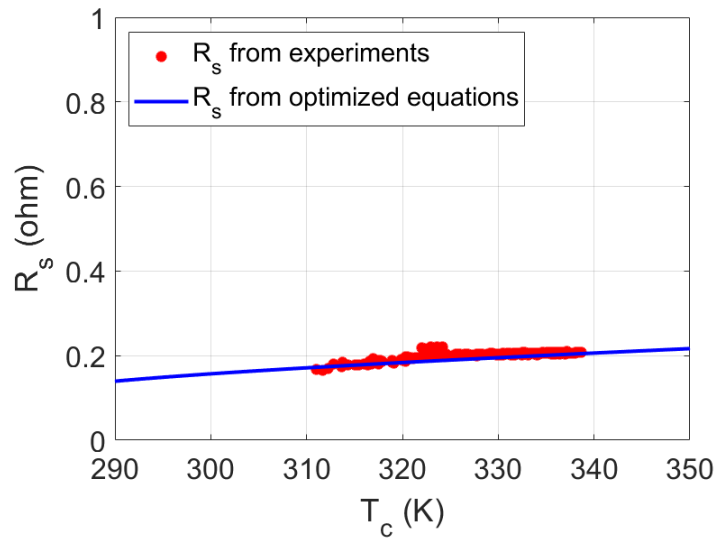Figure 6-3: *n* as a function of irradiance (a) and temperature (b) for module #1.

6.1.4 Series resistance

The dependence of the series resistance on irradiance and temperature is presented in Figure 6-4, while its optimized equation is the following:

$$R_s = \mathbf{0.19} \cdot \frac{T_c}{T_{c,STC}} \cdot \left(1 + \mathbf{0.15} \cdot \log\left(\frac{G}{G_{STC}}\right)\right)$$
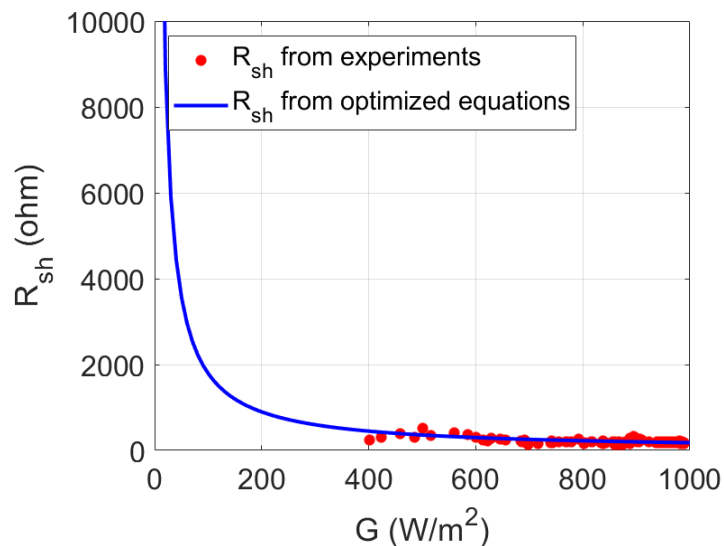

(a)

(b)

Figure 6-4: R_s as a function irradiance (a) and temperature (b) for module #1.

6.1.5 Shunt resistance

The dependence of the shunt resistance on irradiance is presented in Figure 6-5, while its optimized equation is the following:

$$R_{sh} = \mathbf{179.3} \cdot \frac{G_{STC}}{G}$$

Figure 6-5: R_{sh} as a function irradiance for module #1.

6.2 Experimental data and fitting equations for the 5 parameters of module #2

This subsection presents the optimized equations describing each parameter as a function of irradiance and temperature for module #2.

6.2.1 Photogenerated current

The dependence of the photogenerated current on irradiance is presented in Figure 6-6, while its optimized equation is the following:

$$I_{ph} = \mathbf{5.74} \cdot \left[1 + \alpha \cdot \left(T_c - T_{c,STC}\right)\right] \cdot \frac{G}{G_{STC}}$$
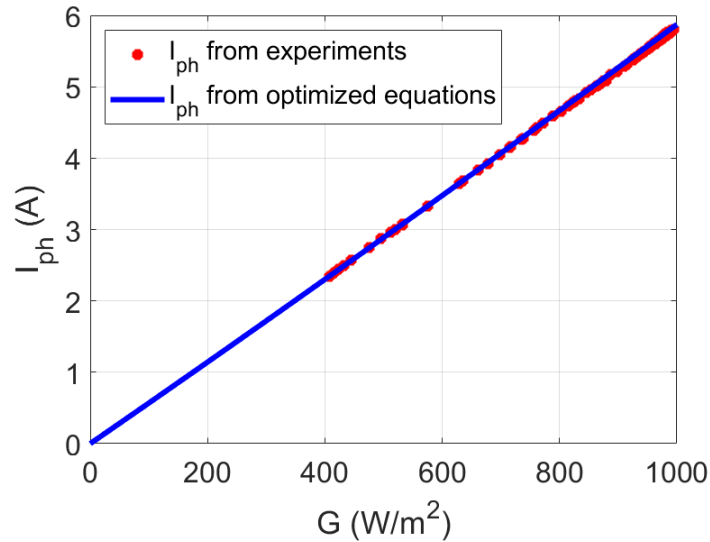

Figure 6-6: I_{ph} as a function of irradiance for module #2.

6.2.2 Reverse saturation current

The dependence of the reverse saturation current on temperature is presented in Figure 6-7, while its optimized equation is the following:

$$I_0 = \mathbf{1.52 \cdot 10^{-9}} \cdot \left(\frac{T_c}{T_{c,STC}}\right)^3 \cdot \exp\left(\left(\frac{E_{g,STC}}{T_{STC}} - \frac{E_g(T_c)}{T_c}\right) \cdot \frac{1}{k_B}\right)$$
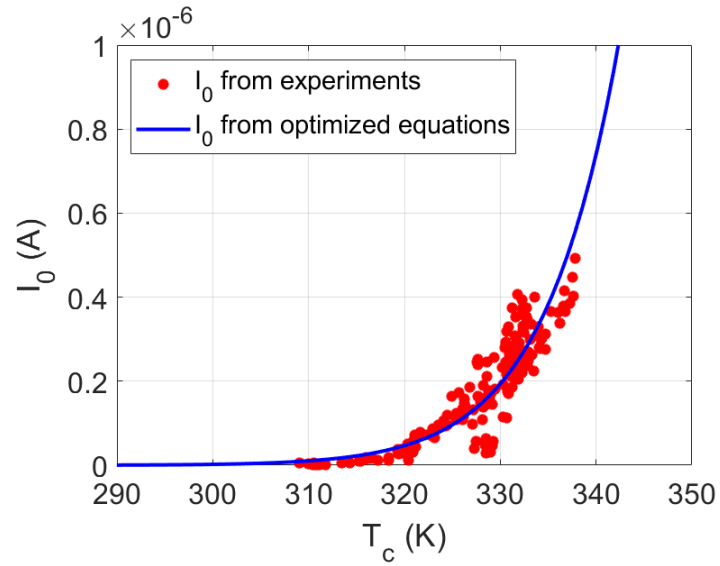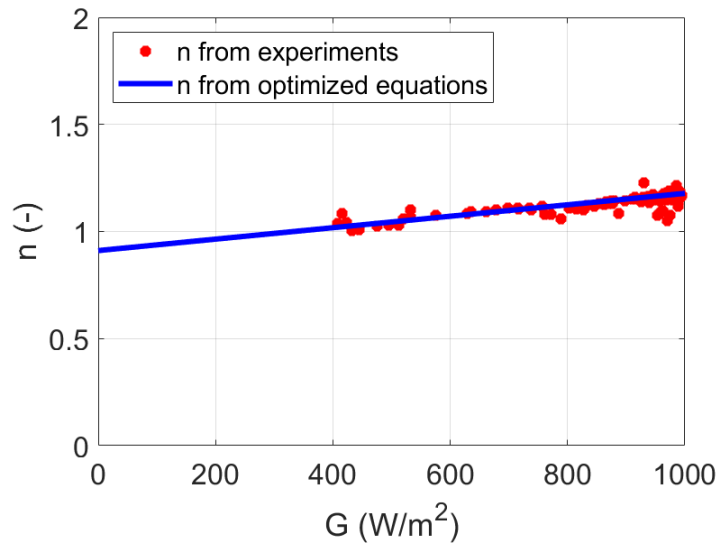
Figure 6-7: I_0 as a function of temperature for module #2.

6.2.3 Diode ideality factor

The dependence of the diode ideality factor on irradiance and temperature is presented in Figure 6-8, while its optimized equation is the following:

$$n = \mathbf{0.58} + \mathbf{1.82 \cdot 10^{-4}} \cdot G + \mathbf{1.22 \cdot 10^{-3}} \cdot T_c$$

(a)
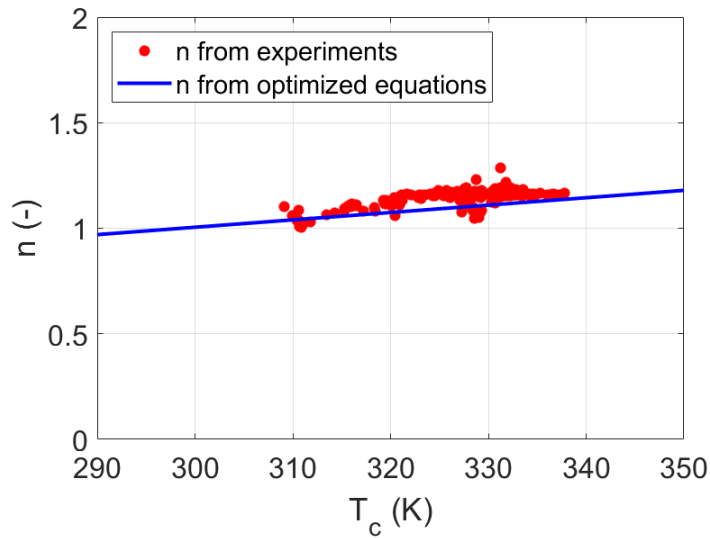
(b)

Figure 6-8: *n* as a function of irradiance (a) and temperature (b) for module #2.

6.2.4 Series resistance

The dependence of the series resistance on irradiance and temperature is presented in Figure 6-9, while its optimized equation is the following:

$$R_s = 0.36 \cdot \frac{T_C}{T_{c,STC}} \cdot \left(1 - 0.12 \cdot \log\left(\frac{G}{G_{STC}}\right)\right)$$

(a)

(b)

Figure 6-9: R_s as a function irradiance (a) and temperature (b) for module #2.

6.2.5 Shunt resistance

The evolution of the shunt resistance with respect to irradiance is dispersed: thus, it is assumed constant and equal to its mean value (5090 Ω).

6.3 Experimental data and fitting equations for the 5 parameters of module #3

This subsection presents the optimized equations describing each parameter as a function of irradiance and temperature for module #3.

6.3.1 Photogenerated current

The dependence of the photogenerated current on irradiance is presented in Figure 6-10, while its optimized equation is the following:

$$I_{ph} = \mathbf{8.55} \cdot \left[1 + \alpha \cdot \left(T_c - T_{c,STC}\right)\right] \cdot \frac{G}{G_{STC}}$$
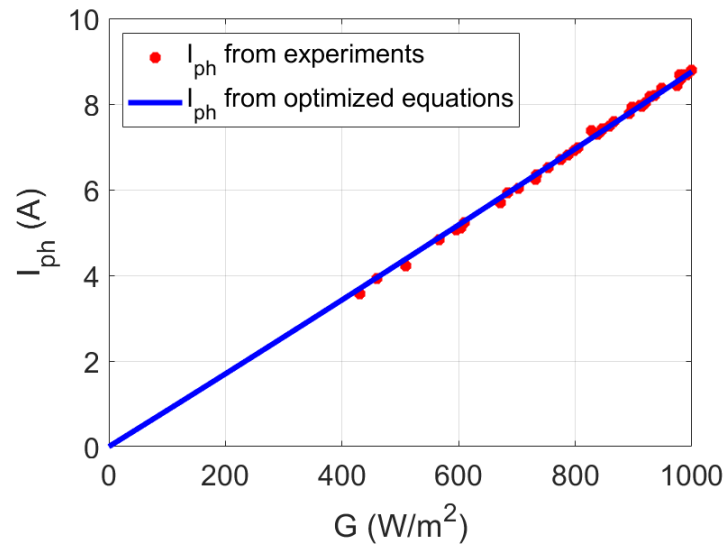
Figure 6-10: I_{ph} as a function of irradiance for module #3.

6.3.2 Reverse saturation current

The dependence of the reverse saturation current on temperature is presented in Figure 6-11, while its optimized equation is the following:

$$I_0 = \mathbf{2.08 \cdot 10^{-8}} \cdot \left(\frac{T_c}{T_{c,STC}}\right)^3 \cdot \exp\left(\left(\frac{E_{g,STC}}{T_{STC}} - \frac{E_g(T_c)}{T_c}\right) \cdot \frac{1}{k_B}\right)$$
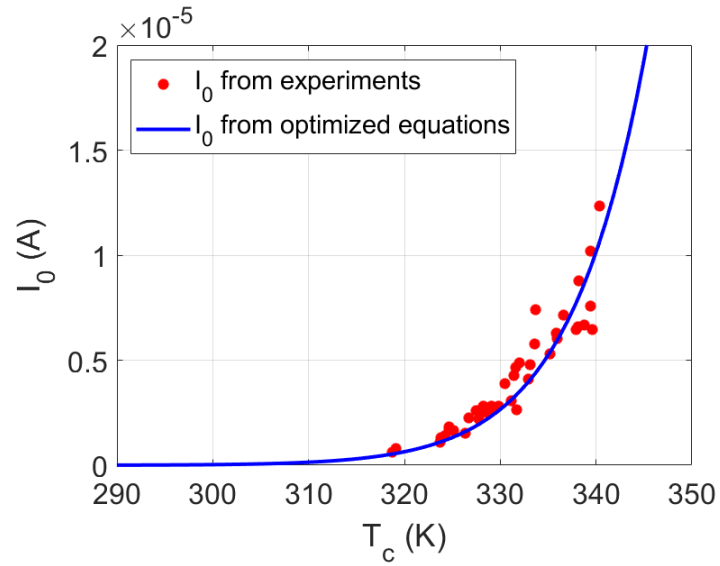
Figure 6-11: I_0 as a function of temperature for module #3.

6.3.3 Diode ideality factor

The dependence of the diode ideality factor on irradiance and temperature is presented in Figure 6-12, while its optimized equation is the following:

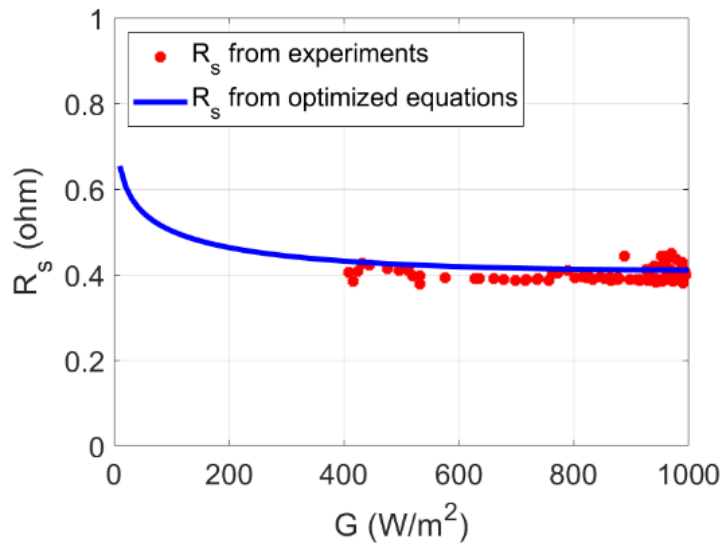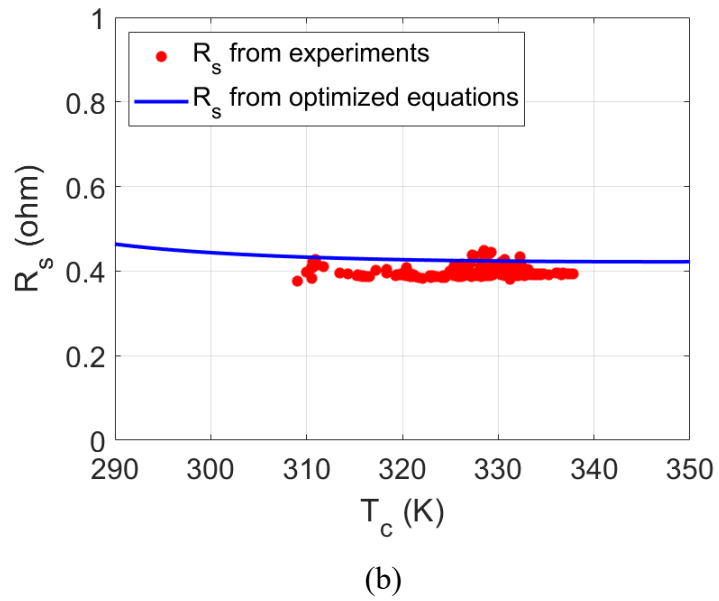$$n = 1.14 + 5.42 \cdot 10^{-5} \cdot G + 3.74 \cdot 10^{-4} \cdot T_c$$

(a)

(b)

Figure 6-12: *n* as a function of irradiance (a) and temperature (b) for module #3.

6.3.4 Series resistance

The dependence of the series resistance on irradiance and temperature is presented in Figure 6-13, while its optimized equation is the following:

$$R_S = 0.30 \cdot \frac{T_c}{T_{c,STC}} \cdot \left(1 - 0.04 \cdot \log\left(\frac{G}{G_{STC}}\right)\right)$$

(a)

(b)
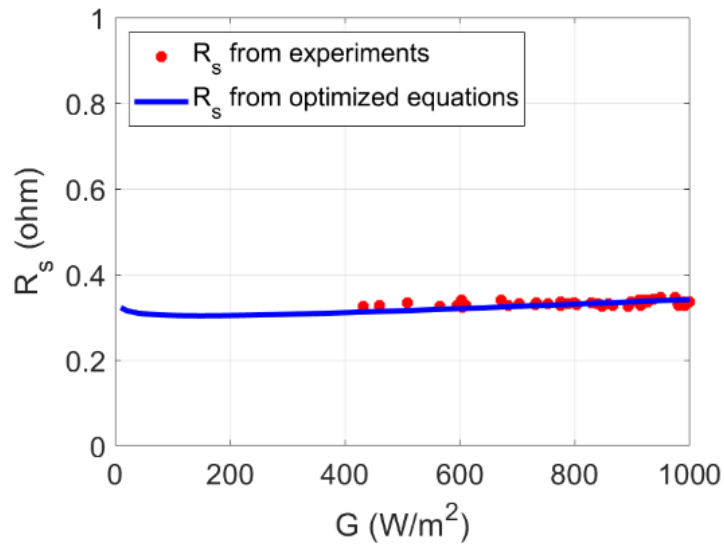
Figure 6-13: R_s as a function irradiance (a) and temperature (b) for module #3.

6.3.5 Shunt resistance

The evolution of the shunt resistance with respect to irradiance is dispersed: thus, it is assumed constant and equal to its mean value (1000 Ω).

6.4 Experimental data and fitting equations for the 5 parameters of module #4

This subsection presents the optimized equations describing each parameter as a function of irradiance and temperature for module #4.

6.4.1 Photogenerated current

The dependence of the photogenerated current on irradiance is presented in Figure 6-14, while its optimized equation is the following:

$$I_{ph} = \mathbf{10.08} \cdot \left[1 + \alpha \cdot \left(T_c - T_{c,STC}\right)\right] \cdot \frac{G}{G_{STC}}$$
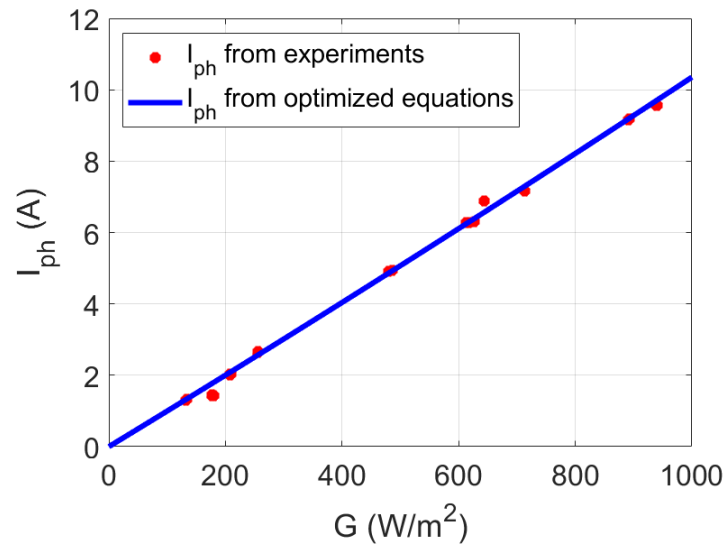
Figure 6-14: I_{ph} as a function of irradiance for module #4.

6.4.2 Reverse saturation current

The dependence of the reverse saturation current on temperature is presented in Figure 6-15, while its optimized equation is the following:

$$I_0 = \mathbf{1.10 \cdot 10^{-9}} \cdot \left(\frac{T_c}{T_{c,STC}}\right)^3 \cdot \exp\left(\left(\frac{E_{g,STC}}{T_{STC}} - \frac{E_g(T_c)}{T_c}\right) \cdot \frac{1}{k_B}\right)$$
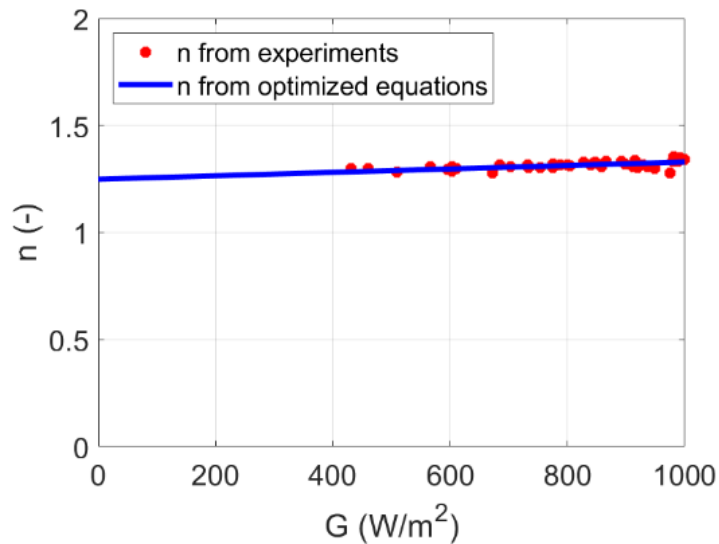
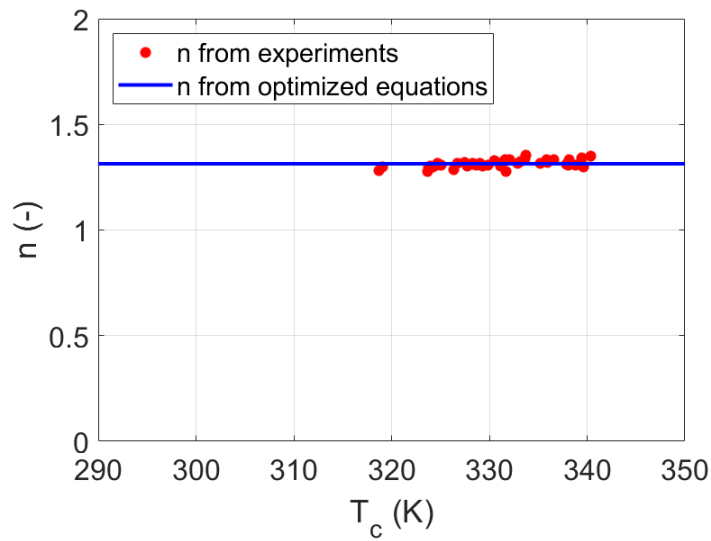Figure 6-15: I_0 as a function of temperature for module #4.

6.4.3 Diode ideality factor

The dependence of the diode ideality factor on irradiance and temperature is presented in Figure 6-16, while its optimized equation is the following:

$$n = \mathbf{1.30} + \mathbf{4.23 \cdot 10^{-5}} \cdot G - \mathbf{6.10 \cdot 10^{-4}} \cdot T_c$$

(a)

(b)

Figure 6-16: *n* as a function of irradiance (a) and temperature (b) for module #4.

6.4.4 Series resistance

The dependence of the series resistance on irradiance and temperature is presented in Figure 6-17, while its optimized equation is the following:

$$R_S = 0.30 \cdot \frac{T_c}{T_{c,STC}} \cdot \left(1 + 0.49 \cdot \log\left(\frac{G}{G_{STC}}\right)\right)$$
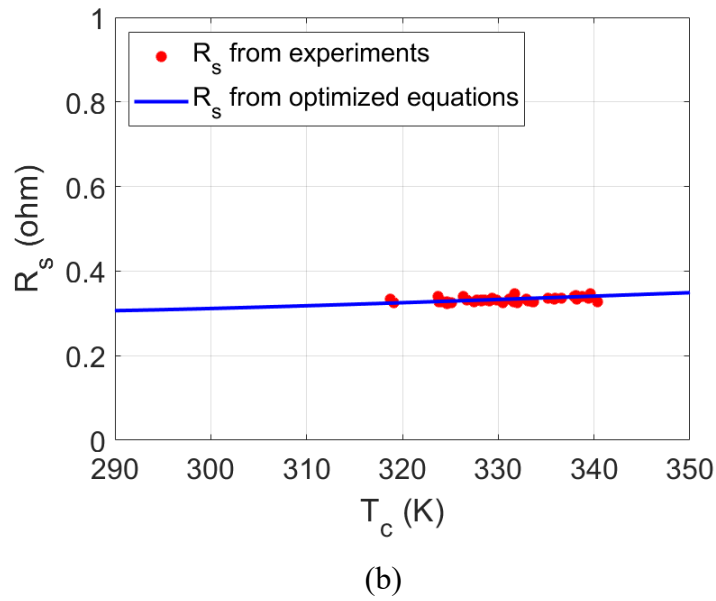

(a)

(b)

Figure 6-17: R_s as a function irradiance (a) and temperature (b) for module #4.

6.4.5 Shunt resistance

The evolution of the shunt resistance with respect to irradiance is dispersed: thus, it is assumed constant and equal to its mean value (1000 Ω).

6.5 Experimental data and fitting equations for the 5 parameters of module #5

This subsection presents the optimized equations describing each parameter as a function of irradiance and temperature for module #5.

6.5.1 Photogenerated current

The dependence of the photogenerated current on irradiance is presented in Figure 6-18, while its optimized equation is the following:

$$I_{ph} = \mathbf{10.47} \cdot \left[1 + \alpha \cdot \left(T_c - T_{c,STC}\right)\right] \cdot \frac{G}{G_{STC}}$$

Figure 6-18: I_{ph} as a function of irradiance for module #5.

6.5.2 Reverse saturation current

The dependence of the reverse saturation current on temperature is presented in Figure 6-19, while its optimized equation is the following:

$$I_0 = \mathbf{4.17 \cdot 10^{-8}} \cdot \left(\frac{T_c}{T_{c,STC}}\right)^3 \cdot \exp\left(\left(\frac{E_{g,STC}}{T_{STC}} - \frac{E_g(T_c)}{T_c}\right) \cdot \frac{1}{k_B}\right)$$
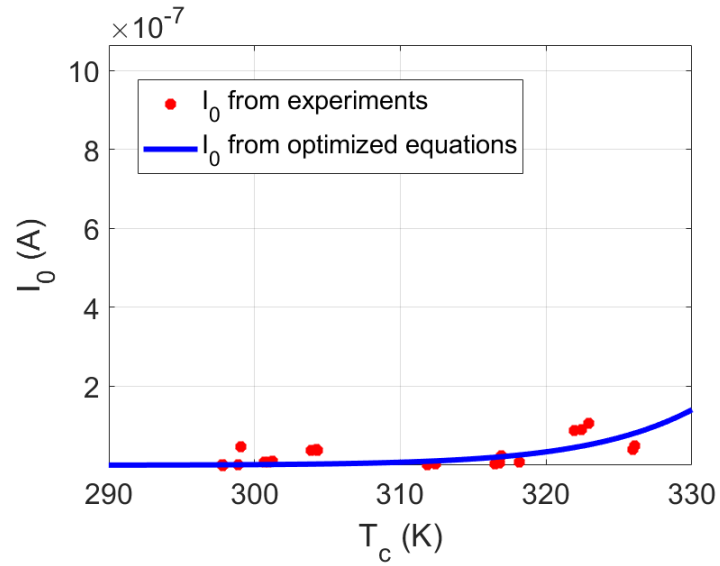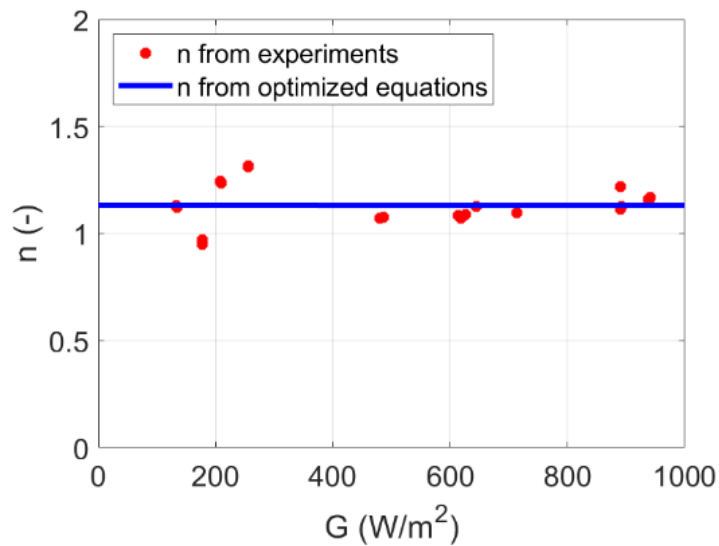
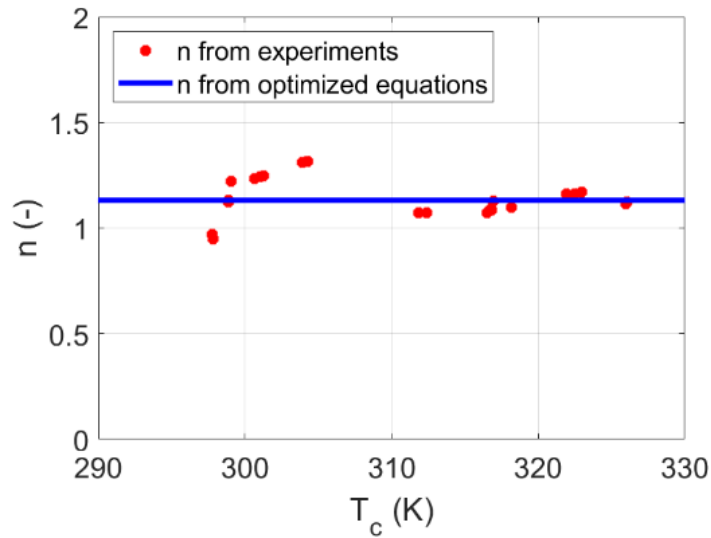Figure 6-19: I_0 as a function of temperature for module #5.

6.5.3 Diode ideality factor

The dependence of the diode ideality factor on irradiance and temperature is presented in Figure 6-20, while its optimized equation is the following:

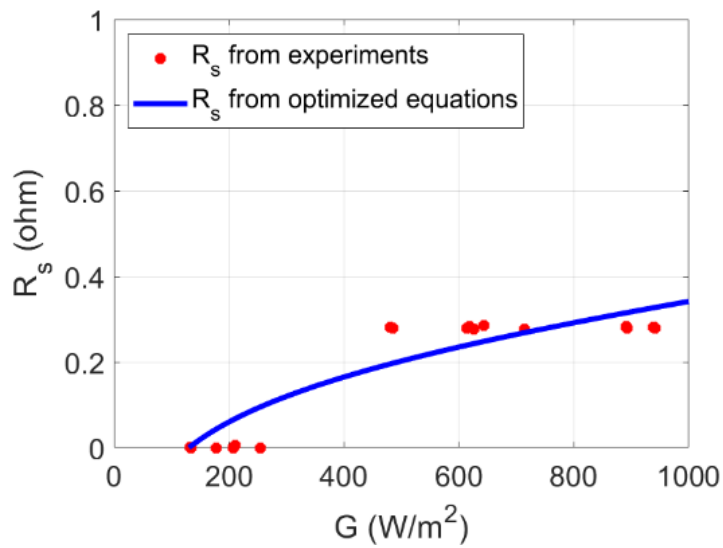$$n = 2.48 + 7.37 \cdot 10^{-4} \cdot G - 4.62 \cdot 10^{-3} \cdot T_c$$

(a)

(b)

Figure 6-20: *n* as a function of irradiance (a) and temperature (b) for module #5.

6.5.4 Series resistance

The dependence of the series resistance on irradiance and temperature is presented in Figure 6-21, while its optimized equation is the following:

$$R_s = \mathbf{0.0037} \cdot \frac{T_c}{T_{c,STC}} \cdot \left(1 - \mathbf{17.19} \cdot \log\left(\frac{G}{G_{STC}}\right)\right)$$

(a)

(b)

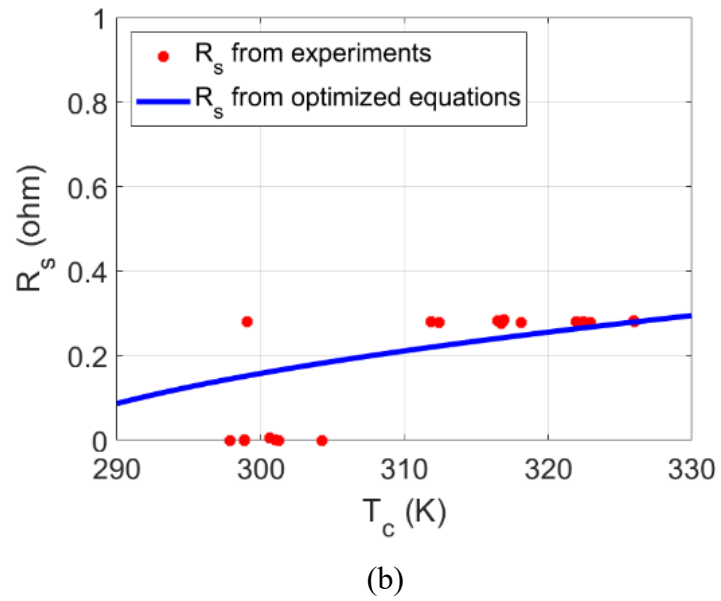Figure 6-21: R_s as a function irradiance (a) and temperature (b) for module #5.

6.5.5 Shunt resistance

The dependence of the shunt resistance on irradiance is presented in Figure 6-22, while its optimized equation is the following:

$$R_{sh} = 112.1 \cdot \frac{G_{STC}}{G}$$
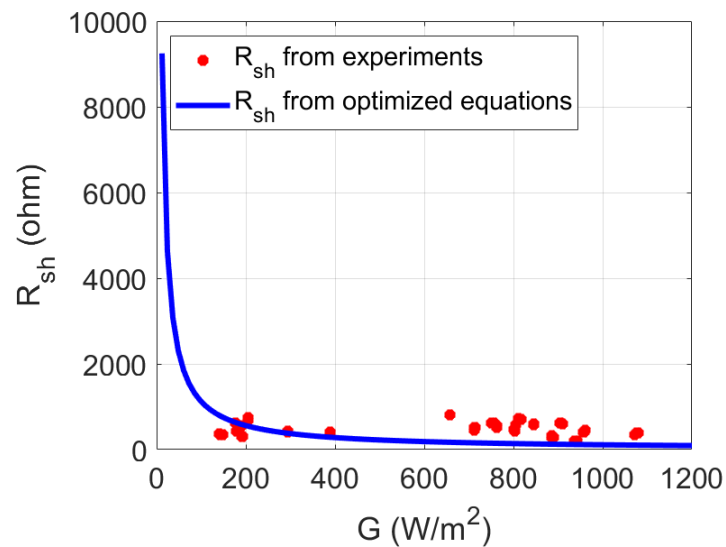
Figure 6-22: R_{sh} as a function irradiance for module #5.

6.6 Experimental data and fitting equations for the 5 parameters of module #6

This subsection presents the optimized equations describing each parameter as a function of irradiance and temperature for module #6.

6.6.1 Photogenerated current

The dependence of the photogenerated current on irradiance is presented in Figure 6-23, while its optimized equation is the following:

$$I_{ph} = 9.11 \cdot \left[1 + \alpha \cdot \left(T_c - T_{c,STC}\right)\right] \cdot \frac{G}{G_{STC}}$$
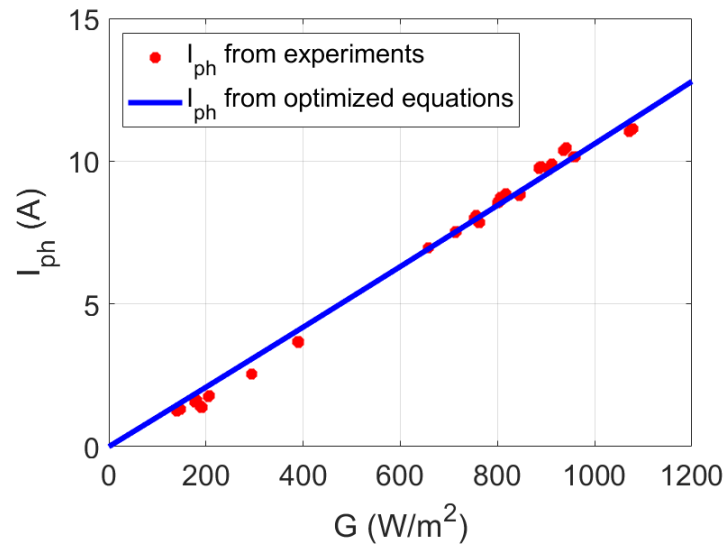

Figure 6-23: I_{ph} as a function of irradiance for module #6.

6.6.2 Reverse saturation current

The dependence of the reverse saturation current on temperature is presented in Figure 6-24, while its optimized equation is the following:

$$I_0 = 1.97 \cdot 10^{-9} \cdot \left(\frac{T_c}{T_{c,STC}}\right)^3 \cdot \exp\left(\left(\frac{E_{g,STC}}{T_{STC}} - \frac{E_g(T_c)}{T_c}\right) \cdot \frac{1}{k_B}\right)$$
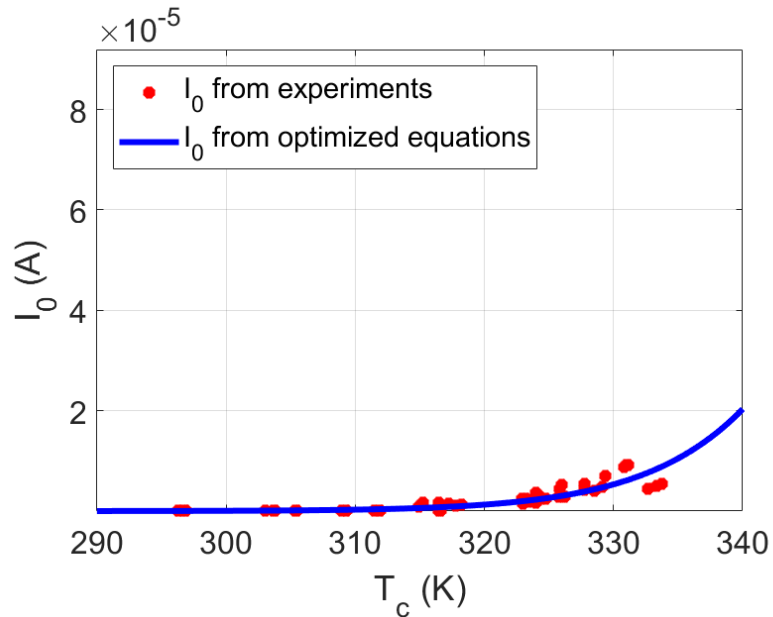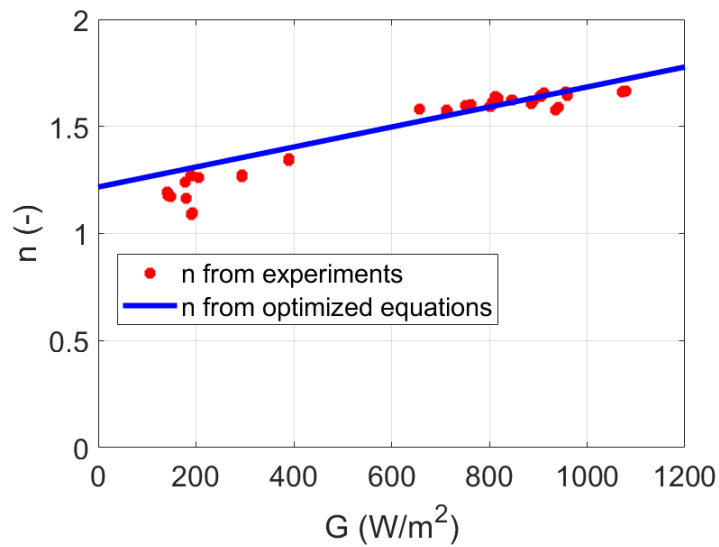
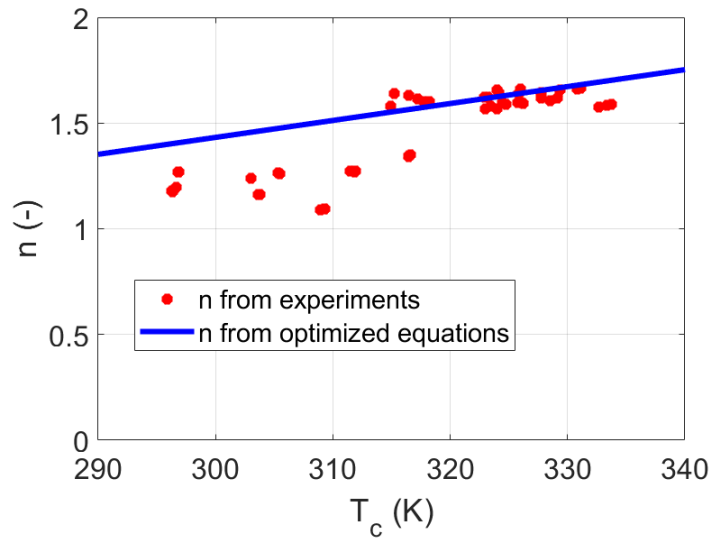Figure 6-24: I_0 as a function of temperature for module #6.

6.6.3 Diode ideality factor

The dependence of the diode ideality factor on irradiance and temperature is presented in Figure 6-25, while its optimized equation is the following:

$$n = \mathbf{1.49} + \mathbf{1.13 \cdot 10^{-4}} \cdot G - \mathbf{1.39 \cdot 10^{-3}} \cdot T_c$$
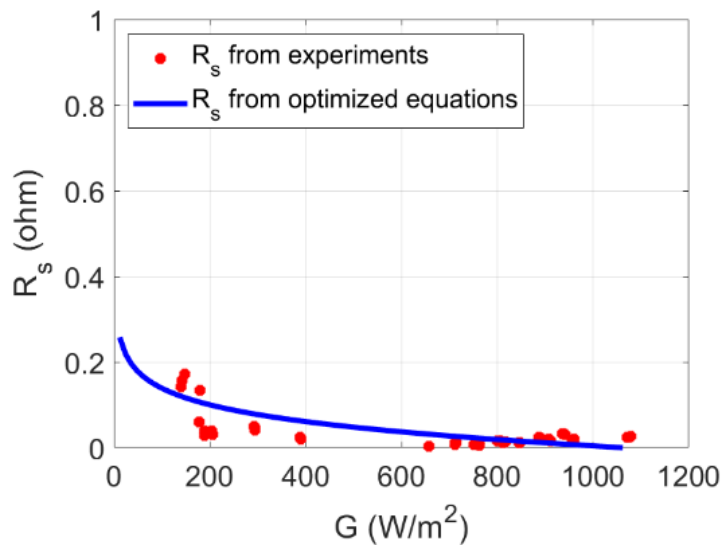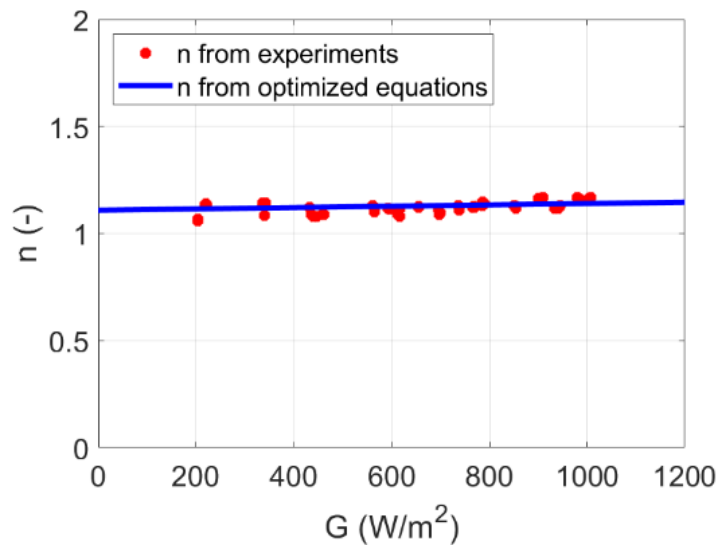

(a)
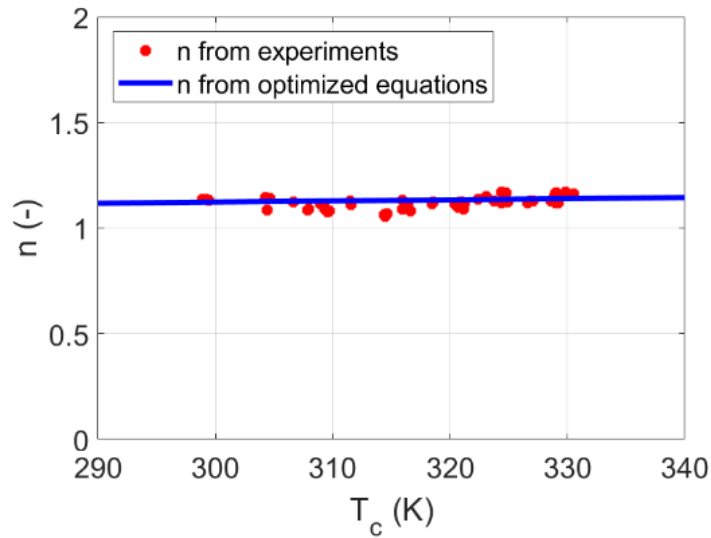
(b)

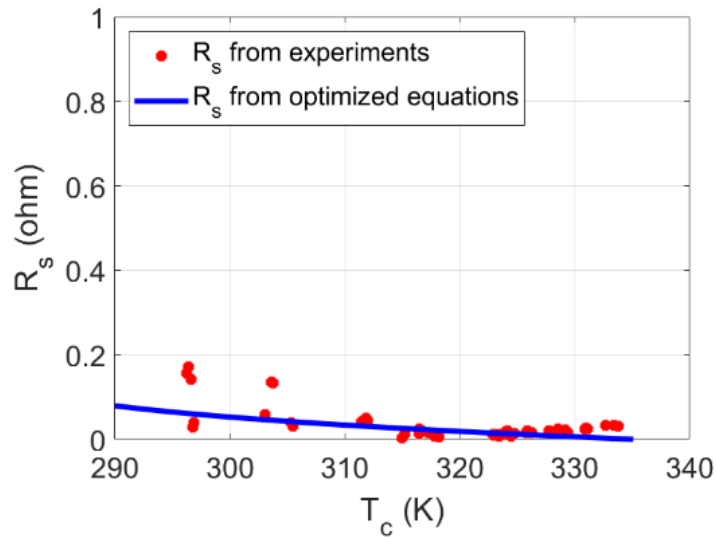Figure 6-25: *n* as a function of irradiance (a) and temperature (b) for module #6.

6.6.4 Series resistance

The dependence of the series resistance on irradiance and temperature is presented in Figure 6-26, while its optimized equation is the following:

$$R_S = 0.22 \cdot \frac{T_c}{T_{c,STC}} \cdot \left(1 - 0.07 \cdot \log\left(\frac{G}{G_{STC}}\right)\right)$$


(a)
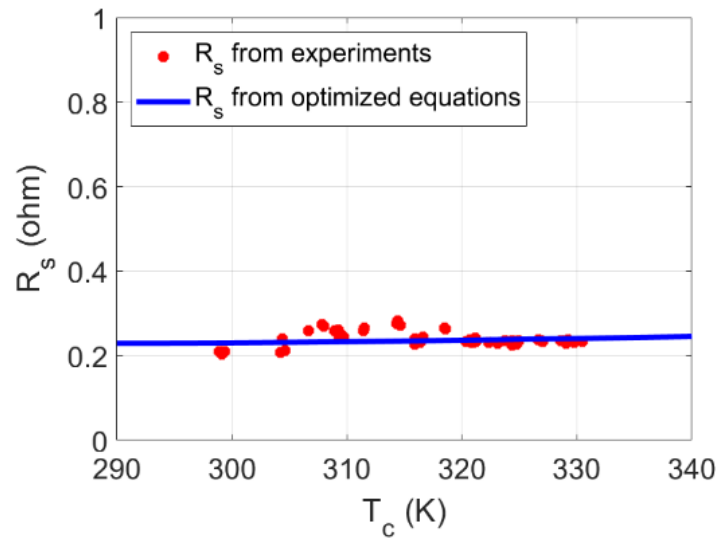
(b)

Figure 6-26: R_s as a function irradiance (a) and temperature (b) for module #6.

6.6.5 Shunt resistance

The dependence of the shunt resistance on irradiance is presented in Figure 6-27, while its optimized equation is the following:

$$R_{sh} = \mathbf{1032\ ohm}$$
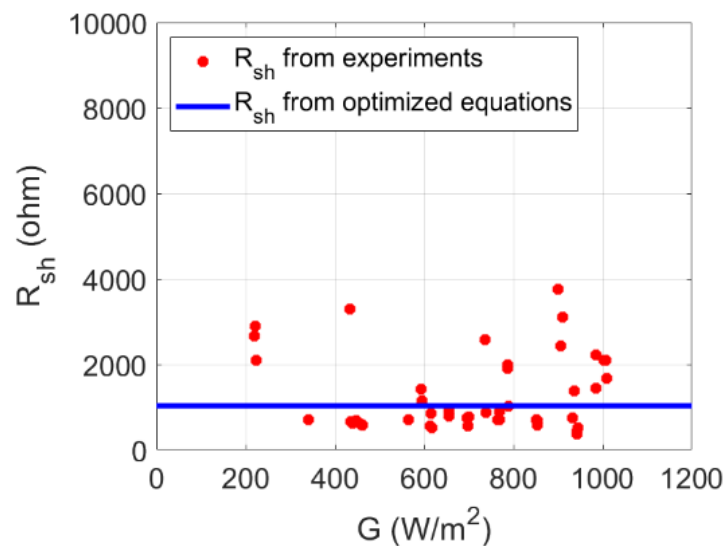
Figure 6-27: R_{sh} as a function irradiance for module #6.

6.7 Experimental data and fitting equations for the 5 parameters of module #7

This subsection presents the optimized equations describing each parameter as a function of irradiance and temperature for module #7.

6.7.1 Photogenerated current

The dependence of the photogenerated current on irradiance is presented in Figure 6-28, while its optimized equation is the following:

$$I_{ph} = 9.42 \cdot \left[1 + \alpha \cdot \left(T_c - T_{c,STC}\right)\right] \cdot \frac{G}{G_{STC}}$$
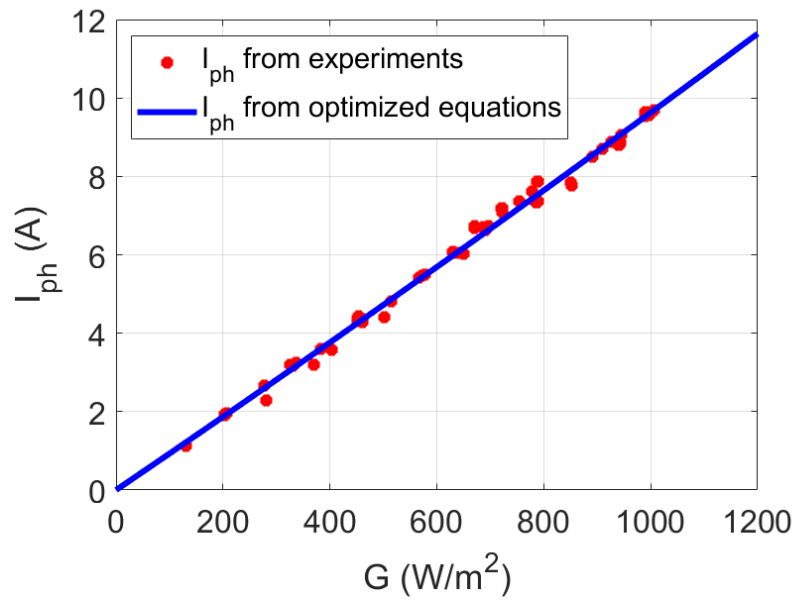
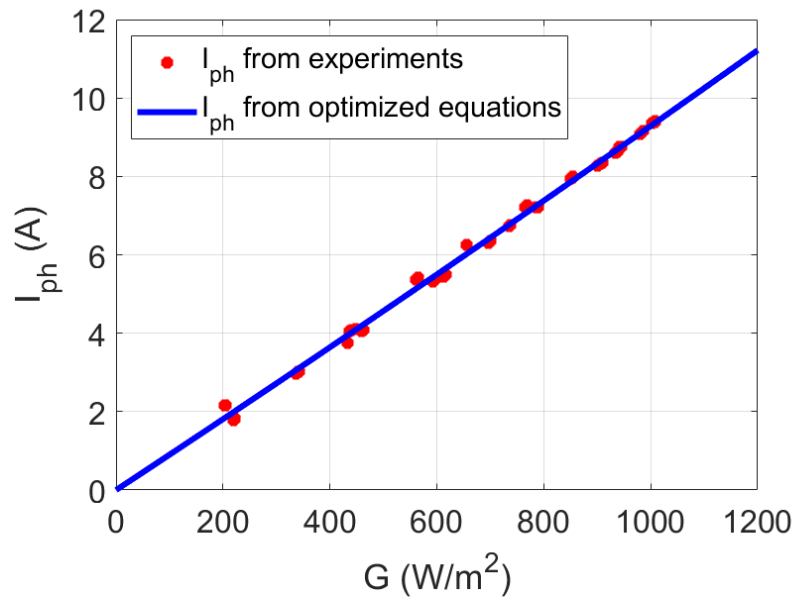Figure 6-28: I_{ph} as a function of irradiance for module #7.

6.7.2 Reverse saturation current

The dependence of the reverse saturation current on temperature is presented in Figure 6-29, while its optimized equation is the following:

$$I_0 = 4.08 \cdot 10^{-9} \cdot \left(\frac{T_c}{T_{c,STC}}\right)^3 \cdot \exp\left(\left(\frac{E_{g,STC}}{T_{STC}} - \frac{E_g(T_c)}{T_c}\right) \cdot \frac{1}{k_B}\right)$$
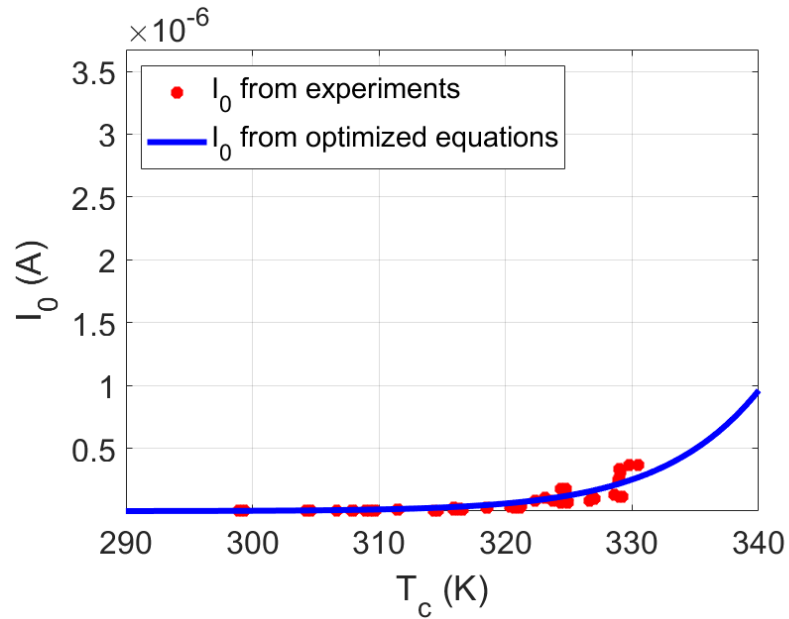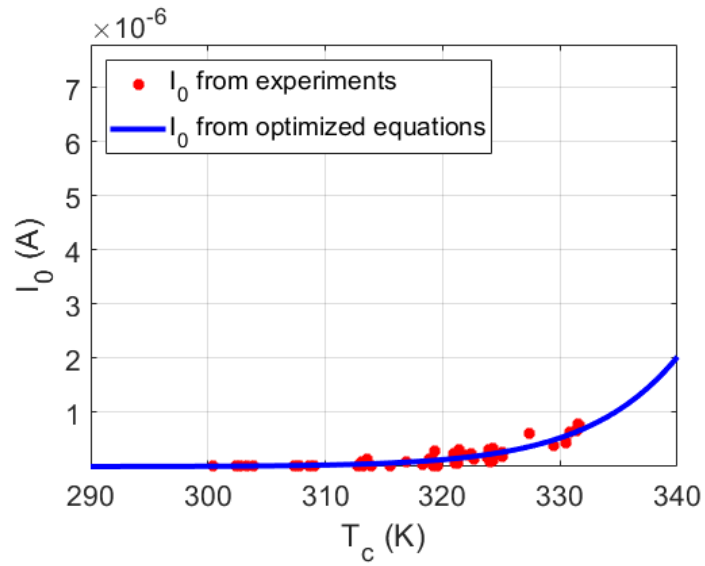
Figure 6-29: I_0 as a function of temperature for module #7.

6.7.3 Diode ideality factor

The dependence of the diode ideality factor on irradiance and temperature is presented in Figure 6-30, while its optimized equation is the following:

$$n = \textcolor{green}{0.58}$$
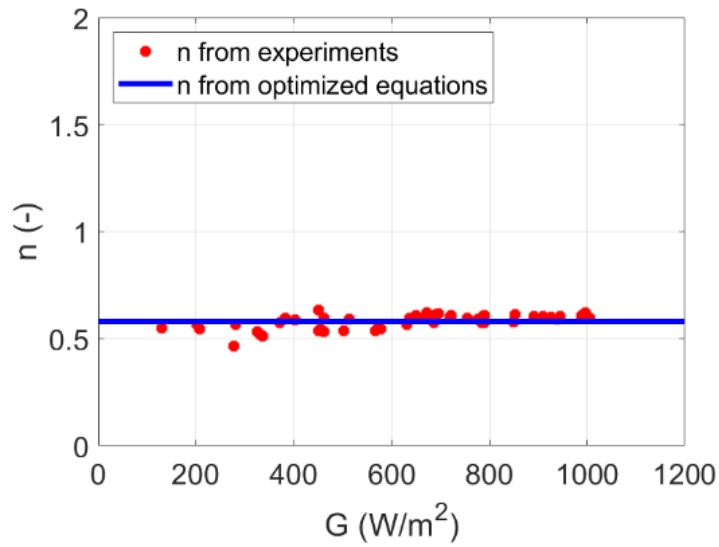
(a)
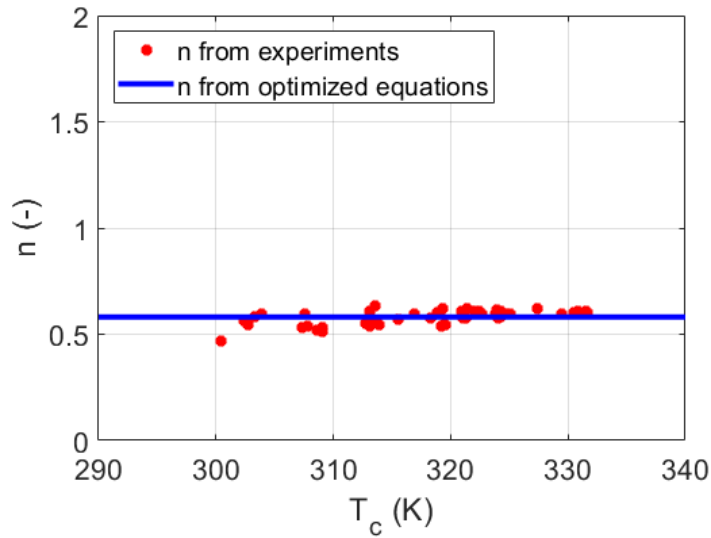
(b)

Figure 6-30: *n* as a function of irradiance (a) and temperature (b) for module #7.

6.7.4 Series resistance

The dependence of the series resistance on irradiance and temperature is presented in Figure 6-31, while its optimized equation is the following:

$$R_s = 0.16 \cdot \frac{T_c}{T_{c,STC}} \cdot \left(1 - 0.29 \cdot \log\left(\frac{G}{G_{STC}}\right)\right)$$

(a)

(b)

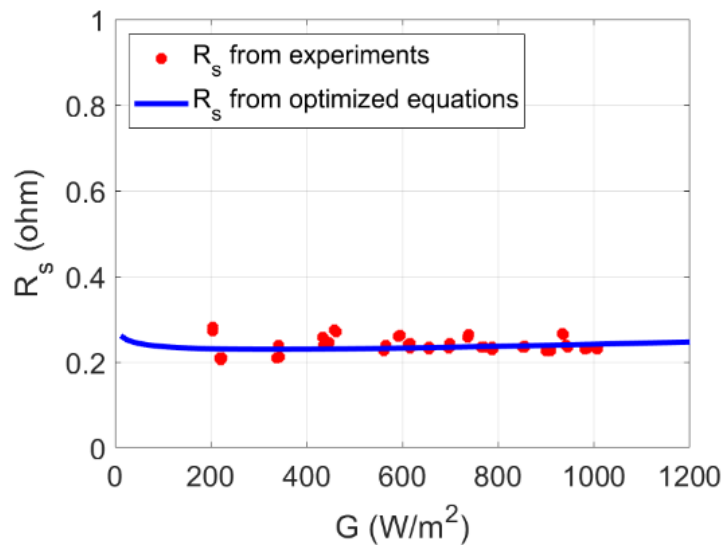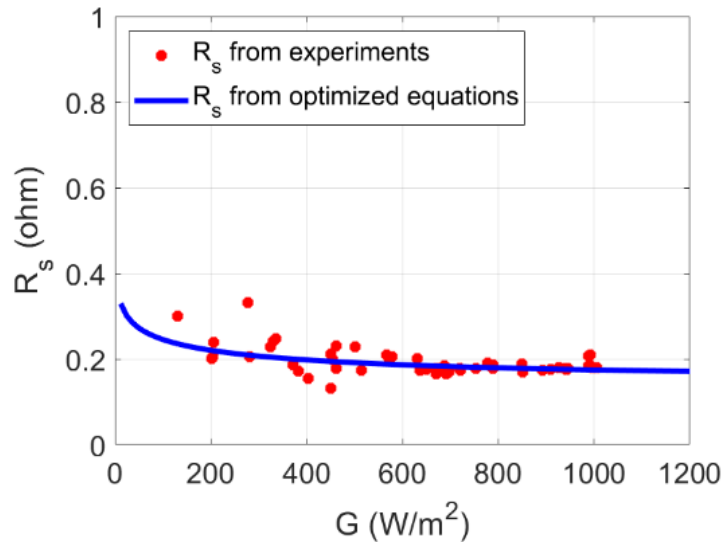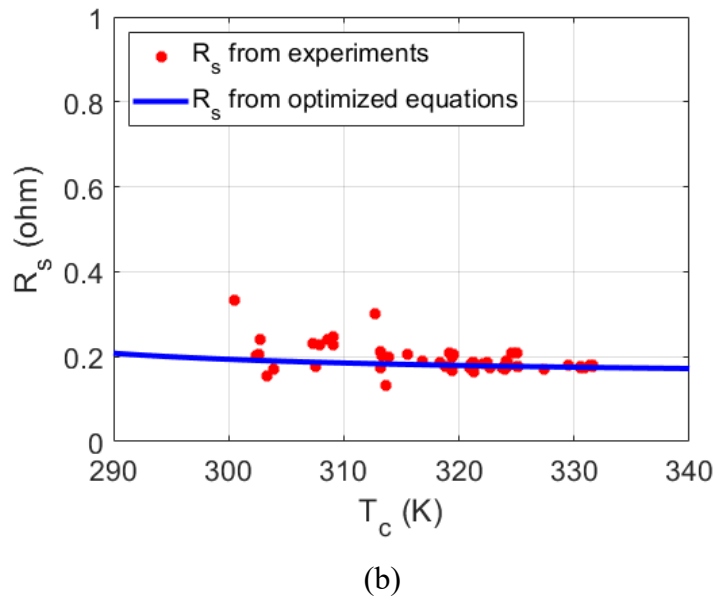Figure 6-31: R_s as a function irradiance (a) and temperature (b) for module #7.

6.7.5 Shunt resistance

The dependence of the shunt resistance on irradiance is presented in Figure 6-32, while its optimized equation is the following:

$$R_{sh} = \mathbf{348\ ohm}$$
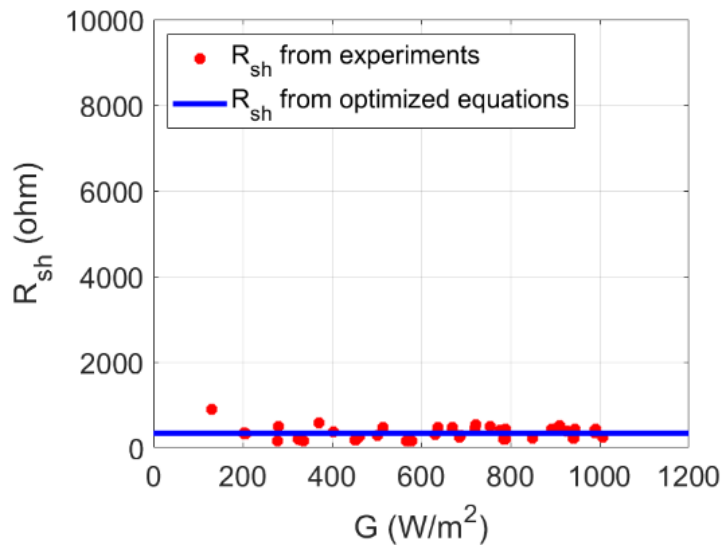
Figure 6-32: R_{sh} as a function irradiance for module #7.

6.8 Power and energy estimation

The results for power estimation as function of irradiance are presented in Figure 6-33. The experimental data are the green dots, while the blue and the red curves refer to the power profiles evaluated with the optimized equations and with the Osterwald model, respectively.
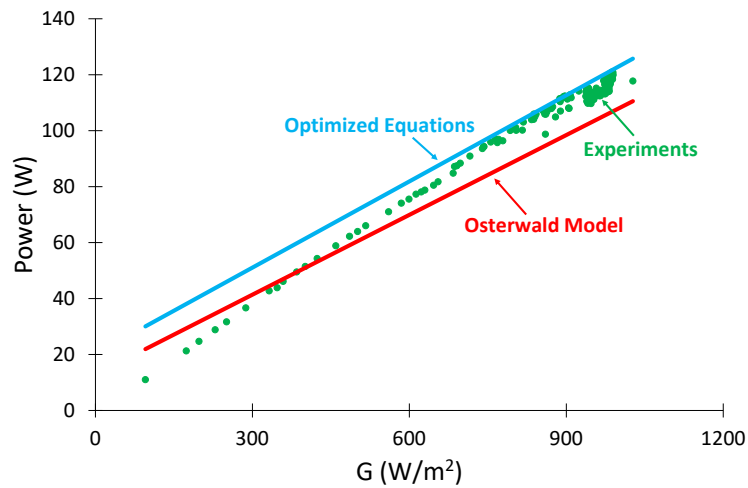
Module #1
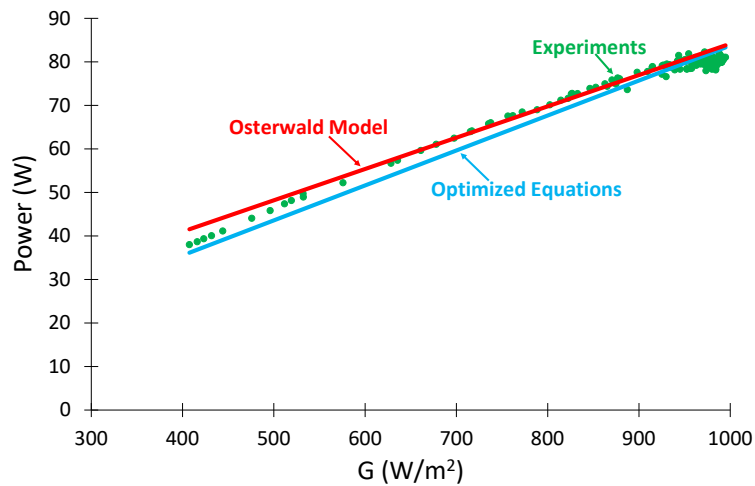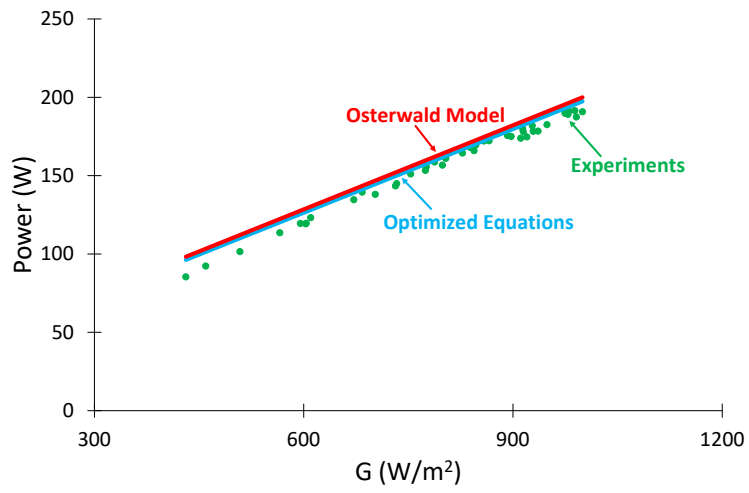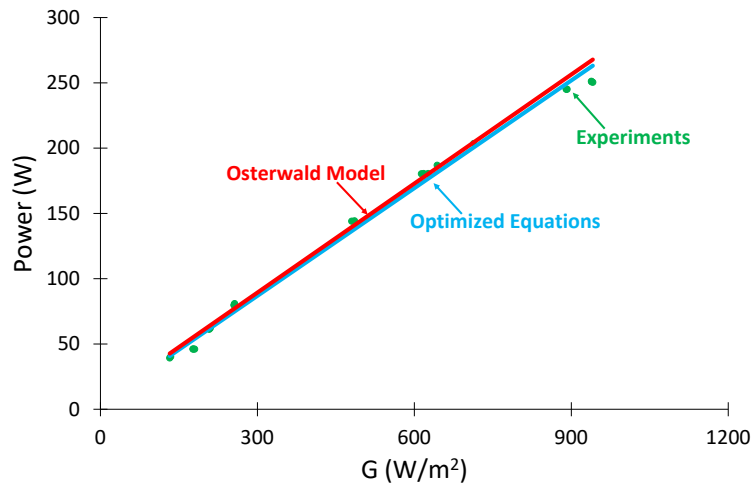
Module #2

Module #3

Module #4
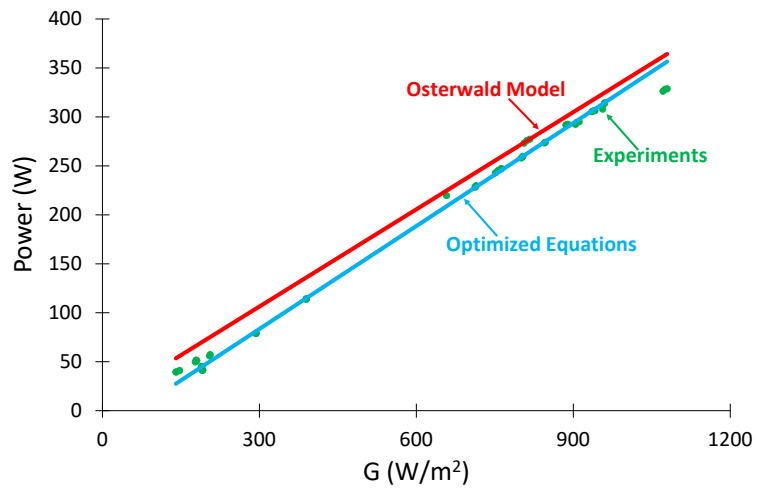
Module #5
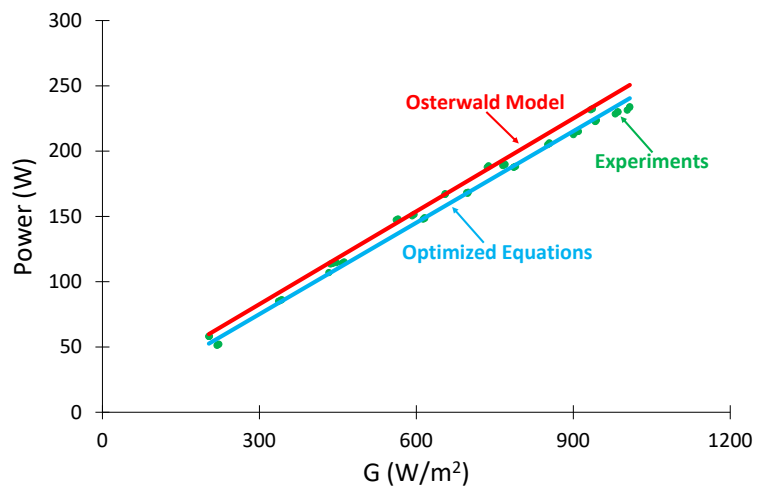
Module #6
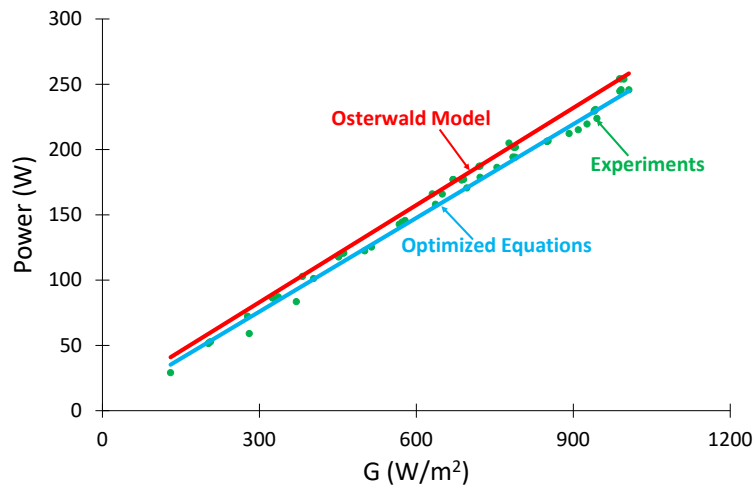
Module #7

Figure 6-33: Power predictions by the models vs experimental data.

The results show that the optimized equations perform better than the Osterwald model for each module under test. In particular, for modules #1 and #2, the Osterwald model is better at low irradiance, while the predictions by the optimized equations are closer to the experimental data at high irradiance. For the other modules, the optimized equations perform better at any irradiance condition. Figure 6-34 presents the values of the $NRMSE_P$ evaluated with the optimized equations (blue bars) and with the Osterwald model (purple bars).

Regarding the $NRMSE_P$, Figure 6-35 presents the percentage improvement of the optimized equations with respect to the Osterwald model. It is in the range ≈5% − ≈50%, and the highest improvements occur for p-Si modules. The experimental campaign for modules #1−#3 consists of hundreds of measurements, representing a good approximation of the weather conditions occurring in a typical year in Spain. On the contrary, the experimental campaign carried out for the other modules in Italy consists of a lower number of acquired *I- V* curves. Thus, the effectiveness of the method may be lower when applied to a typical year in Italy. However, in Figure 6-36, the distribution of irradiance and temperature for a typical year in Turin (Italy) is shown. In this case, the PV modules are supposed with azimuth = 0 ° (South orientation) and inclination of 25 °. The figure shows that the shape of the histograms is similar to the shape of the distributions related to the experimental

campaigns. Thus, the effectiveness of the method is expected to be maintained with wider datasets also.
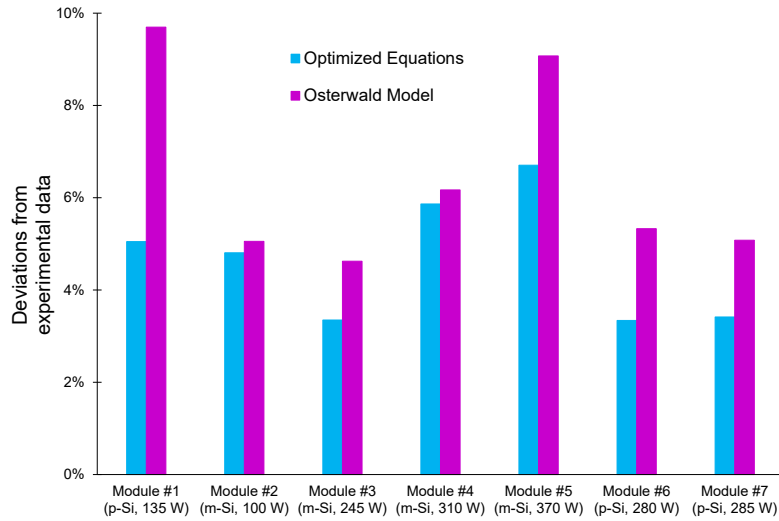
Figure 6-34: *NRMSE* for power prediction.
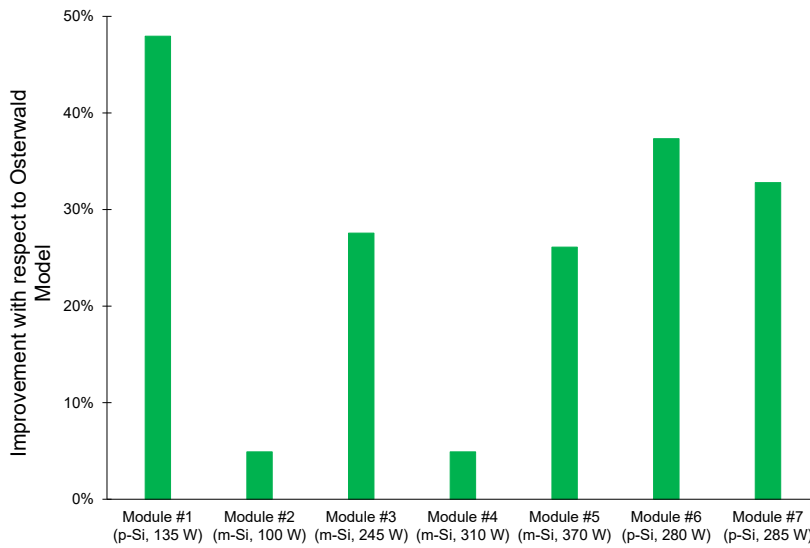
Figure 6-35: Improvement of the optimized equations with respect to the Osterwald model.
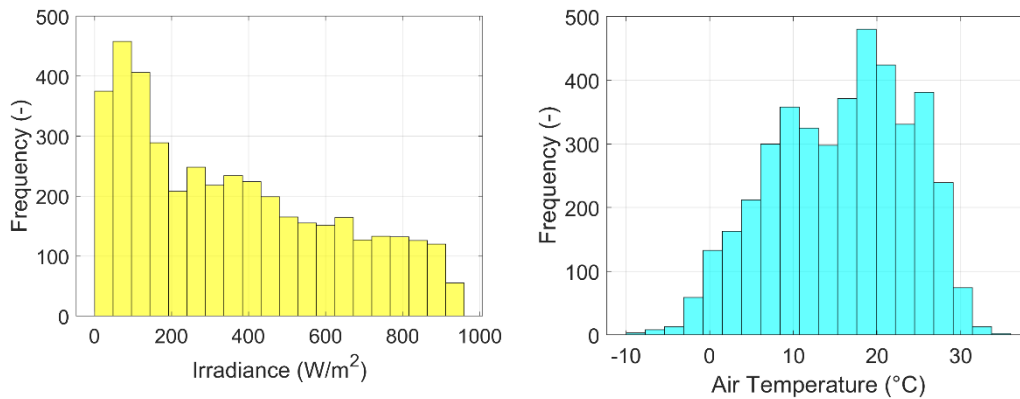
Figure 6-36: Yearly irradiance and air temperature distribution in Turin (Italy).

The energy generated in the campaign is evaluated by supposing the power to be constant in a time interval of 1 min. The results of energy prediction are summarized in Figure 6-37 and Figure 6-38. The optimized equations outperform better the Osterwald model, providing significantly lower deviations with respect to the experimental data: actually, according to the equations, the error on energy prediction is in the range -0.19% − 4.32%. On the contrary, the errors by Osterwald range between 9.02% and 8.28%. Figure 6-38 reports the percentage improvements by the equations with respect to Osterwald, between ≈35% and ≈100%, confirming the effectiveness of the technique.
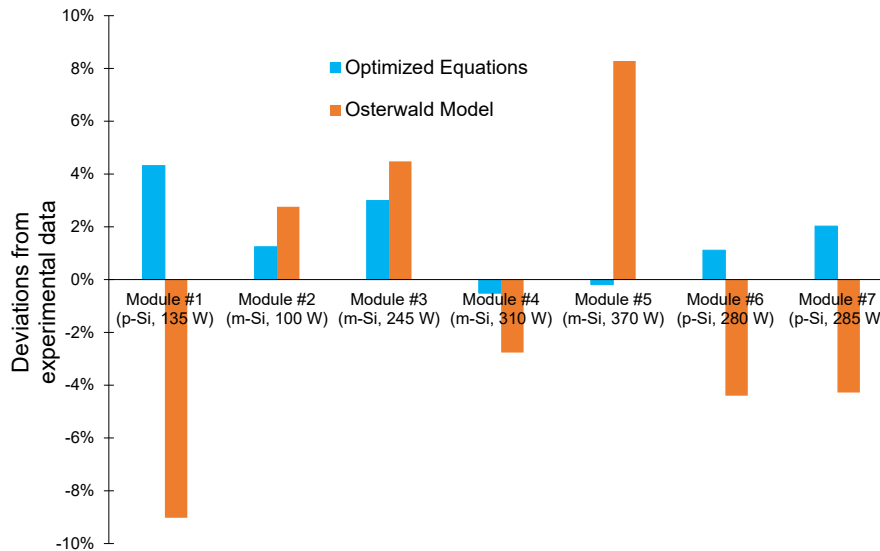
Figure 6-37: Deviation on energy prediction with respect to experiments.
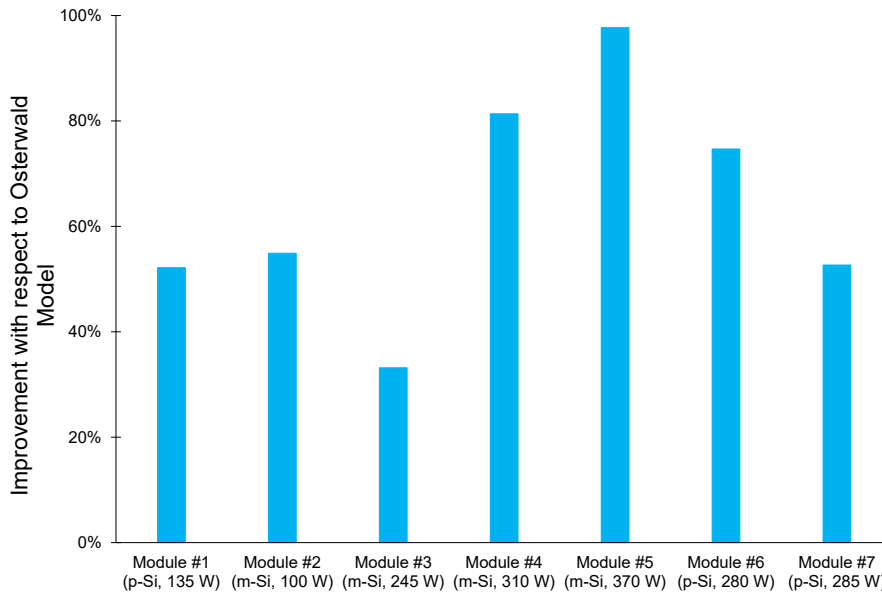
Figure 6-38: Improvement of the optimized equations on energy prediction with respect to Osterwald model.

6.9 Comments

A summary of the results presented in this chapter is reported in Table 5 and the following considerations can be done. Regarding the reverse saturation current, the value of the optimized parameter is similar for all the modules, being in the range $\approx 10^{-9}$ - $\approx 10^{-8}$ A. Regarding the parameter n, the extracted values are between 1 and 2, except for module #7 (n $\approx$0 .6), and this may be due to the different connection of PV cells. Actually, this module has a different behaviour because its cells are half ones: this solution is adopted to reduce the losses in case of mismatch. Regarding the two resistances, since the modules under test have a different number of cells, the corresponding resistances at cell level ($R_{s,cell}$ and $R_{sh,cell}$) are evaluated to compare these parameters obtained for the different modules. Except for PV module #5, the series resistance $R_{s,cell}$ is in the range ≈ 1 - ≈ 10 mΩ, being generally lower for the p-Si technology (blue columns in Table 5) compared to the m-Si one (green columns). PV module #5 has the lowest $R_{s,cell}$ (0.0061 mΩ): this may be due to the location of the electrical contacts in the module. Indeed, it is an all-back contact generator having the busbars and the fingers on its rear side; module #2 has the highest $R_{s,cell}$ ($\approx$10 mΩ). The value of $R_{sh,cell}$ is more dispersed with respect to the other parameters but, as mentioned at the beginning of this chapter, its influence in the transcendental equation is almost negligible. In addition, a worse match between the parameters predicted by the model and the experimental ones can be

observed for PV modules #4 and #5. This may be due to their high efficiency technology: module #4 has a Passivated Emitter and Rear Contact (PERC) technology, while module #5 is an all-back contact generator. These technologies are noticeably more efficient than the other modules under analysis, but wider datasets with hundreds or thousands of measurements may be required to improve the match with the model. Additional considerations will be presented regarding the range of the parameters.

Table 5: Summary of the parameters for the PV modules under test at STC

Module ID	#1	#2	#3	#4	#5	#6	#7
PV technology	p-Si	m-Si	m-Si	m-Si	m-Si	p-Si	p-Si
P_{nom} **(W)**	135	100	245	310	370	280	285
I_0 **(A)**	$8.90 \cdot 10^{-9}$	$1.52 \cdot 10^{-9}$	$2.08 \cdot 10^{-8}$	$1.10 \cdot 10^{-9}$	$4.17 \cdot 10^{-8}$	$1.97 \cdot 10^{-9}$	$4.08 \cdot 10^{-9}$
$R_{s,cell}$ **(mΩ)**	5.16	9.90	4.95	4.94	0.061	3.62	1.31
$R_{sh,cell}$ **(Ω)**	4.98	141.4	16.67	16.67	1.87	17.2	2.9

In Table 6, the range of parameters extracted from experiments is presented for each module under test. Regarding the reverse saturation current, the oldest modules (#1 - #3) present the highest values of this parameter, while the other modules have lower I_0. The behaviour of n is similar for all the modules, being in the range 0.5 – 1.7. Moreover, modules #1 - #3 have higher R_s with respect to the others: however, except for module #5, R_s is almost constant or increases with temperature. This parameter is the sum of two contributions: an ohmic resistance, due to the so-called ribbon (copper tin alloy) connections, and a resistive term due to the semiconductor. The ohmic term has a positive temperature coefficient because it increases with temperature, while the semiconductor term has a negative temperature coefficient (decreases with temperature). For the modules under test, the prevailing resistance is the ohmic one since it increases with temperature. On the contrary, for module #5, R_s decreases with temperature: in such condition, the semiconductor term prevails. This is due to the particular technology of the module (all-back contact), which minimizes the ohmic resistance. Finally, a first indication

about the range for realistic parameters can be provided: actually, experimental data with the following parameters values may be unrealistic or belonging to defective/faulty modules:

- $I_0 > 10\ \mu A$;

- $n < 2$;

- $R_{s,cell} > 10\ m\Omega$ (newer modules) or $R_{s,cell} > 30\ m\Omega$ (older modules).

Table 6: Summary of the parameters ranges for the PV modules under test

Module ID	#1	#2	#3	#4	#5	#6	#7
PV technology	p-Si	m-Si	m-Si	m-Si	m-Si	p-Si	p-Si
P_{nom} **(W)**	135	100	245	310	370	280	285
I_0 **(A)**	$9.73 \cdot 10^{-8} - 2.96 \cdot 10^{-6}$	$1.55 \cdot 10^{-9} - 1.14 \cdot 10^{-6}$	$6.37 \cdot 10^{-7} - 1.23 \cdot 10^{-5}$	$7.44 \cdot 10^{-10} - 1.06 \cdot 10^{-7}$	$1.49 \cdot 10^{-10} - 9.20 \cdot 10^{-6}$	$2.20 \cdot 10^{-9} - 3.67 \cdot 10^{-7}$	$1.40 \cdot 10^{-9} - 7.80 \cdot 10^{-7}$
n **(-)**	1.09 – 1.37	1.23- 1.37	1.28- 1.35	0.74 – 1.31	1.09 – 1.66	1.06 – 1.17	0.47 - 0.63
$R_{s,cell}$ **(mΩ)**	4.60 – 6.20	10.50 – 23.10	5.40 – 5.80	4.6 – 7.7	0.053 – 4	3.40 – 4.70	2.20 – 5.50

6.10 Future application for fault detection

In the future, the present analysis will be furtherly improved in the following way. First, other new PV modules from different technology will be analysed according to the proposed methodology to determine an average behaviour for the generators of the same PV technology. The goal will consist of testing a few tens of other modules. Moreover, the results gained from the analysis will be used to develop an algorithm performing a real time automatic detection of defects in PV plants. The target of the research activity will be the diagnosis analysis of Multi-MW PV plants, including thousands of installed modules. However, at a first stage,

the proposed technique will be validated on PV arrays with rated power up to a few kW. In this context, the automatic detection of defects will be performed by the inverters. Actually, DC/AC converters permit to extract the maximum power by PV generators and trace their *I-V* curve. Starting from these experimental data, the inverters will determine the parameters set of a selected equivalent circuit. At a first stage, the single diode model will be considered, obtaining the experimental parameters set $(I_{ph}, I_0, n, R_s, R_{sh})_{exp}$. On the other side, the inverters will use the optimized equations to estimate the parameters set in same weather conditions. Since the coefficients of the optimized equations refer to PV modules without defects or other issues, these parameters will be used as "reference parameters". The inverters will compare these reference parameters with the experimental parameters set: in case of high deviations among the corresponding quantities, it will be very likely for PV generators to have defects or failures. In such a condition, a notification will be immediately sent to the PV operator, and the part of the PV field having these issues will be identified as well. Then, conventional diagnosis techniques will be adopted on this part of the system. On the contrary, in case of low deviations between the experimental and the reference parameters, no diagnosis methods will be performed. This procedure will lead to two advantages. First, the failures occurring in the plant will cause lower energy losses with respect to current situation. The Mean Down Time (*MDT*) is the average time between a device failure and its restoration to normal operation [61]. This quantity is the sum of different terms and one of these is the delay due to failure notification [62]. This procedure aims to minimize this quantity, providing lower values of *MDT*. In Figure 6-39, the different contributions of the *MDT* are shown.
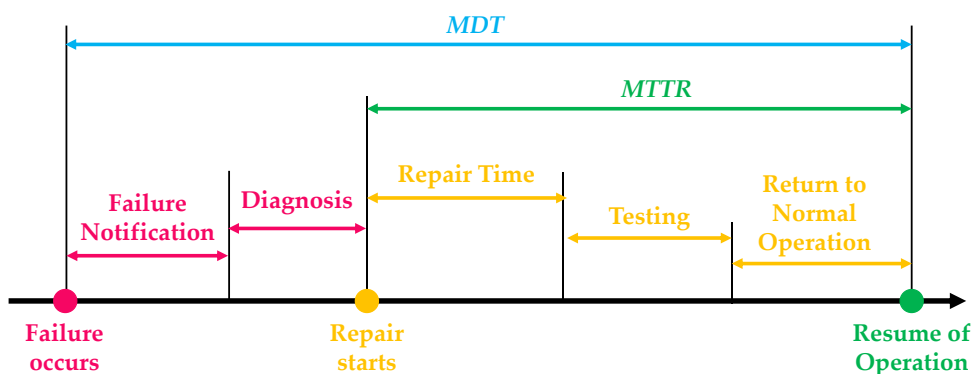
Figure 6-39: Mean down time and mean time to repair of a generic component.

As a consequence, the energy lost during the restoration of PV generators will be minimized as well. The second advantage is economical since the economic cost

due to the maintenance of the system will be minimized as well. This innovative diagnosis technique will not require additional sensors or equipment to identify the faulty arrays. Such parts of the plant will be tested with conventional diagnosis methods (electroluminescence and infrared thermography) to confirm the results of the proposed technique. However, the conventional tests will be performed in the faulty PV arrays only, reducing the overall cost of the tests. Finally, the PV plant under analysis will benefit the higher accuracy of energy prediction with respect to the most common models in literature, i.e., the Osterwald model. The flowchart of this procedure is presented in Figure 6-40 (in green, the contribution by this research activity). In this context, the next research task will consist in identifying a proper tolerance for each parameter to consider values outside this range as defective ones.
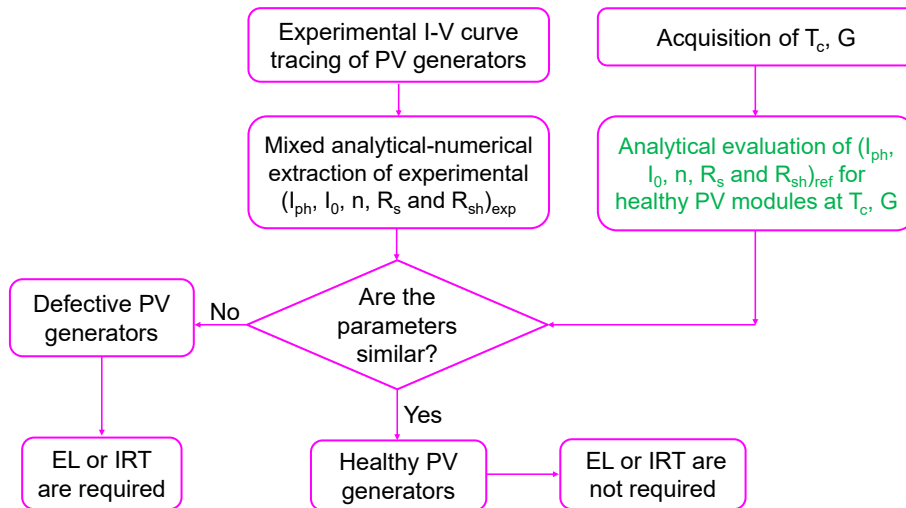
Figure 6-40: Flowchart of the automatic fault detection procedure.

Chapter 7

Conclusions

The knowledge of the equivalent circuit's parameters is fundamental to deeply study and simulate the operation of PV generators in any weather condition. In literature, many papers propose methods to extract these parameters from measurements. However, they refer to specific weather conditions, and the dependence of the parameters on irradiance and temperature is not investigated. Despite a few papers propose some equations to quantify this dependence on weather conditions, some of their coefficients are unknown. Therefore, this information cannot be used to predict the PV energy starting from the knowledge of the equivalent circuit's parameters.

This thesis work proposes an innovative technique to assess the generated energy by PV modules starting from the knowledge of their equivalent circuit parameters. The model consists in four steps, and it is applied to seven PV modules with different technology (p-Si, m-Si, high efficiency m-Si), and rated power (between 100 W and 370 W). In 2021, two experimental campaigns were carried out for these modules: one at Politecnico di Torino (Turin, Italy) and one at the Universidad de Jaèn (Jaén, Spain). The PV modules were tested under a wide range of irradiance (at least 600 W/m^2 of width up to 1000 W/m^2) and module temperature (range of at least 30 °C width up to 65 °C). The sets of parameters of the Single Diode Model (SDM) were determined for each experimental *I-V* curve using two optimization techniques: the Levenberg-Marquardt and a combination of the Simulated Annealing and Nelder Mead (SA/NM) algorithms. The best results in terms of Normalized Root Mean Square Error (*NRMSE*) of the *I-V* curves, and

computational costs are obtained for the SA/NM method. In particular, most of the *NRMSE* for the *I-V* curves estimated by the model was $< 10^{-2}$, and most of the deviation of the maximum power with respect to the experiments was in the range -0.5 %−+0.5 %. The information from the parameters extraction step was used to quantify the dependence of each parameter on weather conditions. Actually, starting from known equations in literature, the experimental parameters were used to optimize the values of their coefficients. Then, PV power generated during the experimental campaign was estimated according to these optimized equations and with the Osterwald model. The deviations with respect to the measurements were quantified by evaluating the corresponding *NRMSE*: the improvement of the optimized equations with respect to the Osterwald model was noticeable, being in the range $\approx 5\% - \approx 50\%$ for all the modules under test. The *NRMSE* with the optimized equations was in the range ≈3 %−≈7 %. In addition, the optimized equations outperformed the Osterwald model regarding the energy prediction as well. PV energy was calculated by assuming the produced power to be constant in a time interval of 1 min, and deviations from experimental data were in the range ≈ -0.5 %−≈ 4 %. Finally, the improvement with respect to the Osterwald model is clear, ranging between ≈ 30 %−≈ 100 %.

In a future work, the proposed model will be applied to other PV modules with wider experimental campaigns. The goal of the work will be the development of an automatic system for fault purposes. This system will be implemented in the inverters, which will perform in real time the following operations. First, they will extract the parameters of an equivalent circuit from the measured *I-V* curves of PV generators. Then, they will compare these parameters with reference values that will be estimated for each weather condition (irradiance and temperature) using the optimized equations. These values will correspond to healthy PV generators without defects or failures. In case of high deviations between these data, a notification will be sent to a PV operator and conventional diagnosis methods (electroluminescence test, infrared thermography and *I-V* curve tracing) will be performed. Such automatic system will lead to lower energy losses by the PV array in case of failures or faults, and economic savings with respect to current conventional diagnosis techniques.

References

1. Di Leo, P.; Spertino, F.; Fichera, S.; Malgaroli, G.; Ratclif, A. Improvement of Self-Sufficiency for an Innovative Nearly Zero Energy Building by Photovoltaic Generators. In Proceedings of the 2019 IEEE Milan PowerTech, PowerTech 2019; 2019.

2. Ciocia, A.; Amato, A.; Di Leo, P.; Fichera, S.; Malgaroli, G.; Spertino, F.; Tzanova, S. Self-Consumption and Self-Sufficiency in Photovoltaic Systems: Effect of Grid Limitation and Storage Installation. *Energies (Basel)* **2021**, *14*, doi:10.3390/en14061591.

3. Spertino, F.; Ciocia, A.; Di Leo, P.; Fichera, S.; Malgaroli, G.; Ratclif, A. Toward the Complete Self-Sufficiency of an NZEBs Microgrid by Photovoltaic Generators and Heat Pumps: Methods and Applications. *IEEE Transactions on Industry Applications* **2019**, *55*, 7028–7040, doi:10.1109/TIA.2019.2914418.

4. Bahrami, M.; Gavagsaz-Ghoachani, R.; Zandi, M.; Phattanasak, M.; Maranzanaa, G.; Nahid-Mobarakeh, B.; Pierfederici, S.; Meibody-Tabar, F. Hybrid Maximum Power Point Tracking Algorithm with Improved Dynamic Performance. *Renewable Energy* **2019**, *130*, 982–991, doi:https://doi.org/10.1016/j.renene.2018.07.020.

5. Harrag, A.; Messalti, S. Extraction of Solar Cell Parameters Using Genetic Algorithm. In Proceedings of the 2015 4th International Conference on Electrical Engineering (ICEE); 2015; pp. 1–5.

6. Lappalainen, K.; Valkealahti, S. Effects of PV Array Layout, Electrical Configuration and Geographic Orientation on Mismatch Losses Caused by Moving Clouds. *Solar Energy* **2017**, *144*, 548–555, doi:https://doi.org/10.1016/j.solener.2017.01.066.

7. Spertino, F.; Ciocia, A.; Di Leo, P.; Tommasini, R.; Berardone, I.; Corrado, M.; Infuso, A.; Paggi, M. A Power and Energy Procedure in Operating Photovoltaic Systems to Quantify the Losses According to the Causes.

Solar Energy **2015**, *118*, 313–326, doi:https://doi.org/10.1016/j.solener.2015.05.033.

8. Mohapatra, A.; Nayak, B.; Das, P.; Mohanty, K.B. A Review on MPPT Techniques of PV System under Partial Shading Condition. *Renewable and Sustainable Energy Reviews* **2017**, *80*, 854–867, doi:https://doi.org/10.1016/j.rser.2017.05.083.

9. Ahmad, J.; Spertino, F.; Ciocia, A.; Di Leo, P. A Maximum Power Point Tracker for Module Integrated PV Systems under Rapidly Changing Irradiance Conditions. In Proceedings of the 2015 International Conference on Smart Grid and Clean Energy Technologies (ICSGCE); 2015; pp. 7–11.

10. Spertino, F.; Malgaroli, G.; Amato, A.; Qureshi, A.E.M.; Ciocia, A.; Siddiqi, H. An Innovative Technique for Energy Assessment of a Highly Efficient Photovoltaic Module. *Solar 2022, Vol. 2, Pages 321-333* **2022**, *2*, 321–333, doi:10.3390/SOLAR2020018.

11. ACCENT Available online: http://klimat.czn.uj.edu.pl/enid/0,59a8eb73686f7774797065092d097072696e74/Climate_Change_classes_ss/ss_Energy_from_the_Sun_6ev.html (accessed on 29 May 2022).

12. Tossa, A.K.; Soro, Y.M.; Azoumah, Y.; Yamegueu, D. A New Approach to Estimate the Performance and Energy Productivity of Photovoltaic Modules in Real Operating Conditions. *Solar Energy* **2014**, *110*, 543–560, doi:https://doi.org/10.1016/j.solener.2014.09.043.

13. Hara, S. Parameter Extraction of Single-Diode Model from Module Datasheet Information Using Temperature Coefficients. *IEEE Journal of Photovoltaics* **2021**, *11*, 213–218, doi:10.1109/JPHOTOV.2020.3035116.

14. Khan, F.; Singh, S.N.; Husain, M. Effect of Illumination Intensity on Cell Parameters of a Silicon Solar Cell. *Solar Energy Materials and Solar Cells* **2010**, *94*, 1473–1476, doi:10.1016/J.SOLMAT.2010.03.018.

15. Most Efficient Solar Panels 2022 — Clean Energy Reviews Available online: https://www.cleanenergyreviews.info/blog/most-efficient-solar-panels (accessed on 29 May 2022).

16. Kebir, S.T.; Haddadi, M.; Ait-Cheikh, M.S. An Overview of Solar Cells Parameters Extraction Methods. In Proceedings of the 2015 3rd International Conference on Control, Engineering Information Technology (CEIT); 2015; pp. 1–7.

17. Nassar-eddine, I.; Obbadi, A.; Errami, Y.; el fajri, A.; Agunaou, M. Parameter Estimation of Photovoltaic Modules Using Iterative Method and the Lambert W Function: A Comparative Study. *Energy Conversion and Management* **2016**, *119*, 37–48, doi:https://doi.org/10.1016/j.enconman.2016.04.030.

18. Awadallah, M.A.; Venkatesh, B. Estimation of PV Module Parameters from Datasheet Information Using Optimization Techniques. In Proceedings of the 2015 IEEE International Conference on Industrial Technology (ICIT); 2015; pp. 2777–2782.

19. Rhouma, M.B.H.; Gastli, A. An Extraction Method for the Parameters of the Solar Cell Single-Diode-Model. In Proceedings of the 2018 2nd European Conference on Electrical Engineering and Computer Science (EECS); 2018; pp. 433–437.

20. Ishaque, K.; Salam, Z.; Taheri, H.; Shamsudin, A. Parameter Extraction of Photovoltaic Cell Using Differential Evolution Method. In Proceedings of the 2011 IEEE Applied Power Electronics Colloquium (IAPEC); 2011; pp. 10–15.

21. Muhsen, D.H.; Ghazali, A.B.; Khatib, T.; Abed, I.A. A Comparative Study of Evolutionary Algorithms and Adapting Control Parameters for Estimating the Parameters of a Single-Diode Photovoltaic Module's Model. *Renewable Energy* **2016**, *96*, 377–389, doi:https://doi.org/10.1016/j.renene.2016.04.072.

22. Khare, A.; Rangnekar, S. A Review of Particle Swarm Optimization and Its Applications in Solar Photovoltaic System. *Applied Soft Computing* **2013**, *13*, 2997–3006, doi:https://doi.org/10.1016/j.asoc.2012.11.033.

23. Jadli, U.; Thakur, P.; Shukla, R.D. A New Parameter Estimation Method of Solar Photovoltaic. *IEEE Journal of Photovoltaics* **2018**, *8*, 239–247, doi:10.1109/JPHOTOV.2017.2767602.

24. Oudira, H.; Mezache, A.; Chouder, A. Solar Cell Parameters Extraction of Photovoltaic Module Using NeIder-Mead Optimization. In Proceedings of the 2018 IEEE 5th International Congress on Information Science and Technology (CiSt); 2018; pp. 455–459.

25. Reza, M.N.; Mominuzzaman, S.M. Extraction of Equivalent Circuit Parameters for CNT Incorporated Perovskite Solar Cells Using Newton-Raphson Method. In Proceedings of the 2018 10th International Conference on Electrical and Computer Engineering (ICECE); 2018; pp. 101–104.

26. Kumar, M.; Shiva Krishna Rao K, D. v Modelling and Parameter Estimation of Solar Cell Using Genetic Algorithm. In Proceedings of the 2019 International Conference on Intelligent Computing and Control Systems (ICCS); 2019; pp. 383–387.

27. Merchaoui, M.; Sakly, A.; Mimouni, M.F. Particle Swarm Optimisation with Adaptive Mutation Strategy for Photovoltaic Solar Cell/Module Parameter Extraction. *Energy Conversion and Management* **2018**, *175*, 151–163, doi:https://doi.org/10.1016/j.enconman.2018.08.081.

28. Morrison, D.R.; Jacobson, S.H.; Sauppe, J.J.; Sewell, E.C. Branch-and-Bound Algorithms: A Survey of Recent Advances in Searching, Branching, and Pruning. *Discrete Optimization* **2016**, *19*, 79–102, doi:https://doi.org/10.1016/j.disopt.2016.01.005.

29. Iterative Improvement for Domain-Specific Problems. In *Algorithms*; pp. 433–434.

30. Ahmed, Z.E.; Saeed, R.A.; Mukherjee, A.; Ghorpade, S.N. 10 - Energy Optimization in Low-Power Wide Area Networks by Using Heuristic Techniques. In *LPWAN Technologies for IoT and M2M Applications*; Chaudhari, B.S., Zennaro, M., Eds.; Academic Press, 2020; pp. 199–223 ISBN 978-0-12-818880-4.

31. Wang, K. Computational Intelligence in Agile Manufacturing Engineering. In *Agile Manufacturing: The 21st Century Competitive Strategy*; Gunasekaran, A., Ed.; Elsevier Science Ltd: Oxford, 2001; pp. 297–315 ISBN 978-0-08-043567-1.

32. Marinaki, M.; Marinakis, Y.; Zopounidis, C. Honey Bees Mating Optimization Algorithm for Financial Classification Problems. *Applied Soft Computing* **2010**, *10*, 806–812, doi:https://doi.org/10.1016/j.asoc.2009.09.010.

33. LI, T.; WANG, Z. Application of Plant Growth Simulation Algorithm on Solving Facility Location Problem. *Systems Engineering - Theory & Practice* **2008**, *28*, 107–115, doi:https://doi.org/10.1016/S1874-8651(10)60025-7.

34. LEVENBERG, K. A METHOD FOR THE SOLUTION OF CERTAIN NON-LINEAR PROBLEMS IN LEAST SQUARES. *Quarterly of Applied Mathematics* **1944**, *2*, 164–168.

35. Marquardt, D.W. An Algorithm for Least-Squares Estimation of Nonlinear Parameters. *Journal of the Society for Industrial and Applied Mathematics* **1963**, *11*, 431–441.

36. Constales, D.; Yablonsky, G.S.; D'hooge, D.R.; Thybaut, J.W.; Marin, G.B. Chapter 9 - Experimental Data Analysis: Data Processing and Regression. In *Advanced Data Analysis & Modelling in Chemical Engineering*; Constales, D., Yablonsky, G.S., D'hooge, D.R., Thybaut, J.W., Marin, G.B., Eds.; Elsevier: Amsterdam, 2017; pp. 285–306 ISBN 978-0-444-59485-3.

37. Aleksendrić, D.; Carlone, P. 5 - Composite Materials – Modelling, Prediction and Optimization. In *Soft Computing in the Design and Manufacturing of Composite Materials*; Aleksendrić, D., Carlone, P., Eds.; Woodhead Publishing: Oxford, 2015; pp. 61–289 ISBN 978-1-78242-179-5.

38. Nelder, J.A.; Mead, R. A Simplex Method for Function Minimization. *The Computer Journal* **1965**, *7*, 308–313, doi:10.1093/comjnl/7.4.308.

39. Forcey, S.; Hamerlinck, G.; Keefe, L.; Sands, W. Chapter 10 - The Minimum Evolution Problem in Phylogenetics: Polytopes, Linear Programming, and Interpretation. In *Algebraic and Combinatorial Computational Biology*; Robeva, R., Macauley, M., Eds.; MSE/Mathematics in Science and Engineering; Academic Press, 2019; pp. 319–349 ISBN 978-0-12-814066-6.

40. Spertino, F.; Ahmad, J.; Ciocia, A.; Di Leo, P.; Murtaza, A.F.; Chiaberge, M. Capacitor Charging Method for I–V Curve Tracer and MPPT in Photovoltaic Systems. *Solar Energy* **2015**, *119*, 461–473, doi:https://doi.org/10.1016/j.solener.2015.06.032.

41. Drabczyk, K.; Kulesza-Matlak, G.; Drygała, A.; Szindler, M.; Lipiński, M. Electroluminescence Imaging for Determining the Influence of Metallization Parameters for Solar Cell Metal Contacts. *Solar Energy* **2016**, *126*, 14–21, doi:10.1016/J.SOLENER.2015.12.029.

42. Deitsch, S.; Christlein, V.; Berger, S.; Buerhop-Lutz, C.; Maier, A.; Gallwitz, F.; Riess, C. Automatic Classification of Defective Photovoltaic Module Cells in Electroluminescence Images. *Solar Energy* **2019**, *185*, 455–468, doi:10.1016/J.SOLENER.2019.02.067.

43. Rajput, A.S.; Ho, J.W.; Zhang, Y.; Nalluri, S.; Aberle, A.G. Quantitative Estimation of Electrical Performance Parameters of Individual Solar Cells in Silicon Photovoltaic Modules Using Electroluminescence Imaging. *Solar Energy* **2018**, *173*, 201–208, doi:10.1016/J.SOLENER.2018.07.046.

44. Tang, W.; Yang, Q.; Hu, X.; Yan, W. Convolution Neural Network Based Polycrystalline Silicon Photovoltaic Cell Linear Defect Diagnosis Using Electroluminescence Images. *Expert Systems with Applications* **2022**, *202*, 117087, doi:10.1016/J.ESWA.2022.117087.

45. Tang, W.; Yang, Q.; Xiong, K.; Yan, W. Deep Learning Based Automatic Defect Identification of Photovoltaic Module Using Electroluminescence Images. *Solar Energy* **2020**, *201*, 453–460, doi:10.1016/J.SOLENER.2020.03.049.

46. Weber, T.; Albert, A.; Ferretti, N.; Roericht, M.; Krauter, S.; Grunow, P. ELECTROLUMINESCENCE INVESTIGATION ON THIN FILM MODULES.; May 2011.

47. Ciocia, A.; Carullo, A.; Di Leo, P.; Malgaroli, G.; Spertino, F. Realization and Use of an IR Camera for Laboratory and On-Field Electroluminescence Inspections of Silicon Photovoltaic Modules. In Proceedings of the 2019 IEEE 46th Photovoltaic Specialists Conference (PVSC); 2019; pp. 2734–2739.

48. Spertino, F.; Ciocia, A.; Corona, F.; Di Leo, P.; Papandrea, F. An Experimental Procedure to Check the Performance Degradation On-Site in Grid-Connected Photovoltaic Systems. In Proceedings of the 2014 IEEE 40th Photovoltaic Specialist Conference (PVSC); 2014; pp. 2600–2604.

49. Chaibi, Y.; Salhi, M.; El-jouni, A.; Essadki, A. A New Method to Extract the Equivalent Circuit Parameters of a Photovoltaic Panel. *Solar Energy* **2018**, *163*, 376–386, doi:10.1016/J.SOLENER.2018.02.017.

50. Abbassi, A.; ben Mehrez, R.; Touaiti, B.; Abualigah, L.; Touti, E. Parameterization of Photovoltaic Solar Cell Double-Diode Model Based on Improved Arithmetic Optimization Algorithm. *Optik (Stuttg)* **2022**, *253*, 168600, doi:10.1016/J.IJLEO.2022.168600.

51. Kumar, C.; Magdalin Mary, D. A Novel Chaotic-Driven Tuna Swarm Optimizer with Newton-Raphson Method for Parameter Identification of Three-Diode Equivalent Circuit Model of Solar Photovoltaic Cells/Modules. *Optik (Stuttg)* **2022**, 169379, doi:10.1016/J.IJLEO.2022.169379.

52. Chaibi, Y.; Allouhi, A.; Malvoni, M.; Salhi, M.; Saadani, R. Solar Irradiance and Temperature Influence on the Photovoltaic Cell Equivalent-Circuit Models. *Solar Energy* **2019**, *188*, 1102–1110, doi:10.1016/J.SOLENER.2019.07.005.

53. Sesa, E.; Vaughan, B.; Feron, K.; Bilen, C.; Zhou, X.; Belcher, W.; Dastoor, P. A Building-Block Approach to the Development of an Equivalent Circuit Model for Organic Photovoltaic Cells. *Organic Electronics* **2018**, *58*, 207–215, doi:10.1016/J.ORGEL.2018.04.019.

54. Lineykin, S.; Averbukh, M.; Kuperman, A. An Improved Approach to Extract the Single-Diode Equivalent Circuit Parameters of a Photovoltaic Cell/Panel. *Renewable and Sustainable Energy Reviews* **2014**, *30*, 282–289, doi:10.1016/J.RSER.2013.10.015.

55. Salhi, S.; Queen, N.M. A Hybrid Algorithm for Identifying Global and Local Minima When Optimizing Functions with Many Minima. *European Journal of Operational Research* **2004**, *155*, 51–67, doi:10.1016/S0377-2217(02)00871-8.

56. Abdel-Basset, M.; Mohamed, R.; AbdelAziz, N.M.; Abouhawwash, M. HWOA: A Hybrid Whale Optimization Algorithm with a Novel Local Minima Avoidance Method for Multi-Level Thresholding Color Image Segmentation. *Expert Systems with Applications* **2022**, *190*, 116145, doi:10.1016/J.ESWA.2021.116145.

57. Majdoul, R.; Abdelmounim, E.; Aboulfatah, M.; Touati, A.W.; Moutabir, A.; Abouloifa, A. Combined Analytical and Numerical Approach to Determine the Four Parameters of the Photovoltaic Cells Models. In Proceedings of the 2015 International Conference on Electrical and Information Technologies (ICEIT); 2015; pp. 263–268.

58. Campanelli, M.B.; Osterwald, C.R. Effective Irradiance Ratios to Improve <italic>I–V</Italic> Curve Measurements and Diode Modeling Over a Range of Temperature and Spectral and Total Irradiance. *IEEE Journal of Photovoltaics* **2016**, *6*, 48–55, doi:10.1109/JPHOTOV.2015.2489866.

59. Evans, D.L. Simplified Method for Predicting Photovoltaic Array Output. *Solar Energy* **1981**, *27*, 555–560, doi:10.1016/0038-092X(81)90051-7.

60. Khezzar, R.; Zereg, M.; Khezzar, A. Comparative Study of Mathematical Methods for Parameters Calculation of Current-Voltage Characteristic of Photovoltaic Module. In Proceedings of the 2009 International Conference on Electrical and Electronics Engineering - ELECO 2009; 2009; pp. I-24-I–28.

61. Baschel, S.; Koubli, E.; Roy, J.; Gottschalg, R. Impact of Component Reliability on Large Scale Photovoltaic Systems' Performance. *Energies (Basel)* **2018**, *11*, doi:10.3390/en11061579.

62. Spertino, F.; Amato, A.; Casali, G.; Ciocia, A.; Malgaroli, G. Reliability Analysis and Repair Activity for the Components of 350 KW Inverters in a Large Scale Grid-Connected Photovoltaic System. *Electronics (Basel)* **2021**, *10*, doi:10.3390/electronics10050564.

Appendix

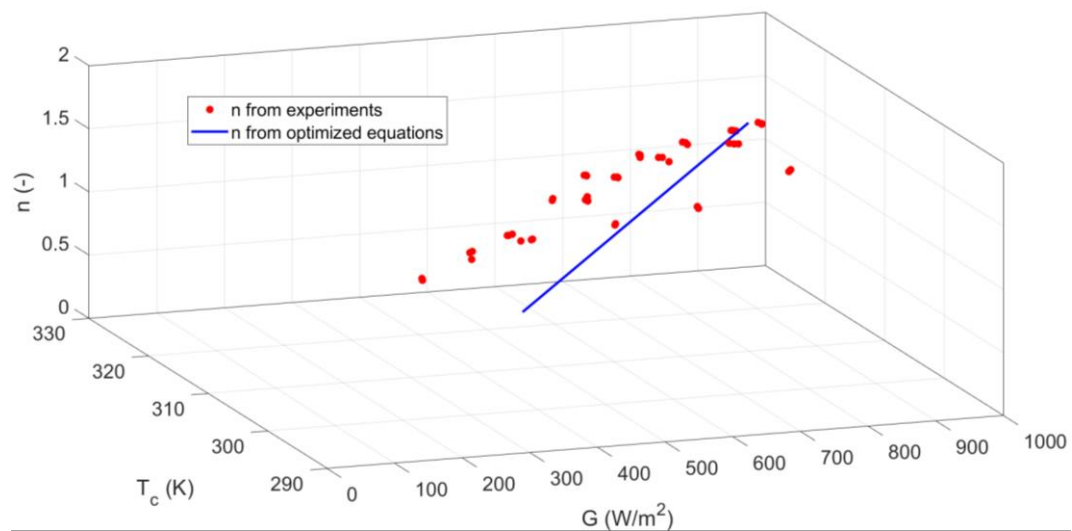*3D plots for PV module #4*
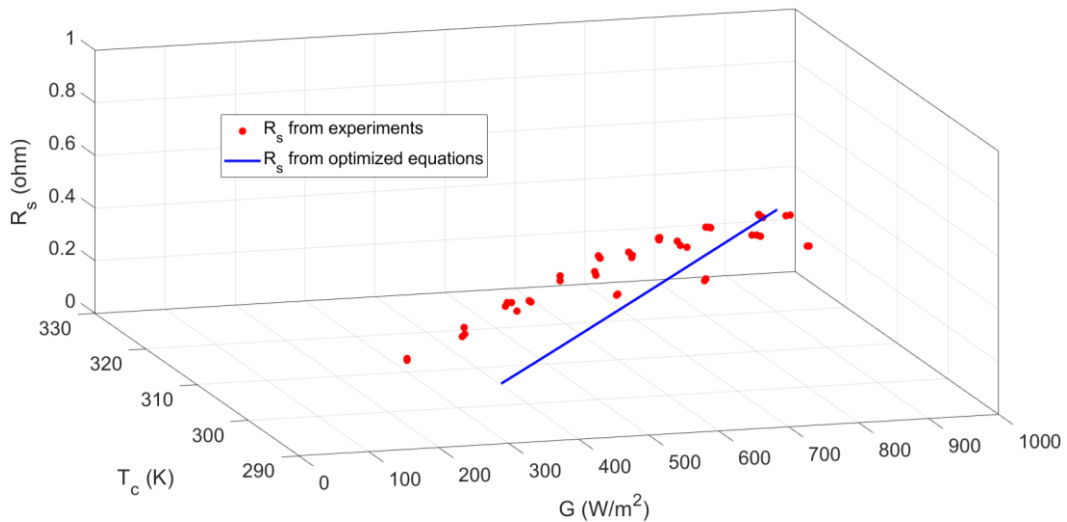
In this section, the 3D plots for the equivalent circuit's parameters depending on irradiance and temperature both (photogenerated current I_{ph}, diode ideality factor n, and series resistance R_s) are reported for PV module #4.
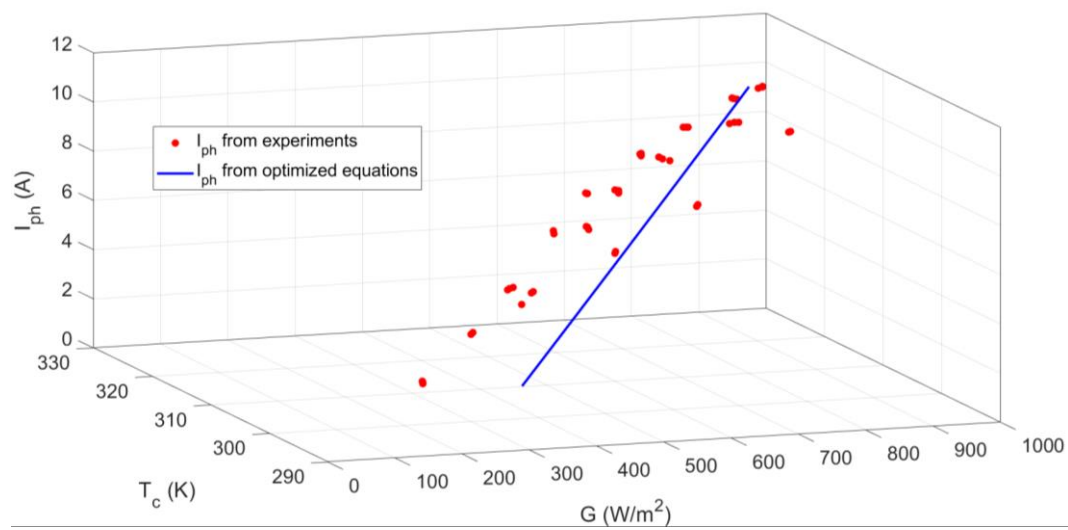
I_{ph} as a function of irradiance and temperature for module #4.

n as a function of irradiance and temperature for module #4.

*R*_s as a function of irradiance and temperature for module #4.

List of publications co-authored by the Ph D candidate during the PhD program in chronological order

- Spertino, F.; Ciocia, A.; Di Leo, P.; Malgaroli, G.; Russo, A. A Smart Battery Management System for Photovoltaic Plants in Households Based on Raw Production Forecast. Green Energy Advances 2018, doi:10.5772/INTECHOPEN.80562.
- Spertino, F.; Chicco, G.; Ciocia, A.; Malgaroli, G.; Mazza, A.; Russo, A. Harmonic Distortion and Unbalance Analysis in Multi-Inverter Photovoltaic Systems. *SPEEDAM 2018 - Proceedings: International Symposium on Power Electronics, Electrical Drives, Automation and Motion* **2018**, 1031–1036, doi:10.1109/SPEEDAM.2018.8445358.
- Spertino, F.; Fichera, S.; Ciocia, A.; Malgaroli, G.; Di Leo, P.; Ratclif, A. Toward the Complete Self-Sufficiency of an NZEBS Microgrid by Photovoltaic Generators and Heat Pumps: Methods and Applications. *IEEE Transactions on Industry Applications* **2019**, *55*, 7028–7040, doi:10.1109/TIA.2019.2914418.
- Ciocia, A.; Carullo, A.; Di Leo, P.; Malgaroli, G.; Spertino, F. Realization and Use of an IR Camera for Laboratory and On-Field Electroluminescence Inspections of Silicon Photovoltaic Modules. In Proceedings of the 2019 IEEE 46th Photovoltaic Specialists Conference (PVSC); 2019; pp. 2734–2739.
- Di Leo, P; Spertino, F.; Fichera, S.; Malgaroli, G.; Ratclif, A. Improvement of Self-Sufficiency for an Innovative Nearly Zero

Energy Building by Photovoltaic Generators. In Proceedings of the 2019 IEEE Milan PowerTech, PowerTech 2019; 2019.

- Spertino, F.; Chiodo, E.; Ciocia, A.; Malgaroli, G.; Ratclif, A. Maintenance Activity, Reliability Analysis and Related Energy Losses in Five Operating Photovoltaic Plants. *Proceedings - 2019 IEEE International Conference on Environment and Electrical Engineering and 2019 IEEE Industrial and Commercial Power Systems Europe, EEEIC/I and CPS Europe 2019* **2019**, doi:10.1109/EEEIC.2019.8783240.

- Ciocia, A.; Malgaroli, G.; Spedicato, A.; Spertino, F.; Andrei, H.; Boicea, V.A. Quality Check during Manufacturing of Custom Photovoltaic Modules with Back-Contact Cells. *2019 54th International Universities Power Engineering Conference, UPEC 2019 - Proceedings* **2019**, doi:10.1109/UPEC.2019.8893478.

- Bizzarri, F.; Nitti, S.; Malgaroli, G. The Use of Drones in the Maintenance of Photovoltaic Fields. *E3S Web of Conferences* **2019**, *119*, 00021, doi:10.1051/E3SCONF/201911900021.

- Carullo, A.; Ciocia, A.; Di Leo, P.; Giordano, F.; Malgaroli, G.; Peraga, L.; Spertino, F.; Vallan, A. Comparison of Correction Methods of Wind Speed for Performance Evaluation of Wind Turbines. In Proceedings of the Proceedings of 24th IMEKO TC4 International Symposium 22nd International Workshop on ADC and DAC Modelling and Testing; Palermo, Italy, September 2020.

- Ciocia, A.; Di Leo, P.; Fichera, S.; Giordano, F.; Malgaroli, G.; Spertino, F. A Novel Procedure to Adjust the Equivalent Circuit Parameters of Photovoltaic Modules under Shading. *2020 International Symposium on Power Electronics, Electrical Drives, Automation and Motion, SPEEDAM 2020* **2020**, 711–715, doi:10.1109/SPEEDAM48782.2020.9161878.

- Ciocia, A.; Di Leo, P.; Malgaroli, G.; Spertino, F. Subhour Simulation of a Microgrid of All-Electric NZEBs Based on Italian Market Rules. *Proceedings - 2020 IEEE International Conference on Environment and Electrical Engineering and 2020 IEEE Industrial and Commercial Power Systems Europe, EEEIC / I and CPS Europe 2020* **2020**, doi:10.1109/EEEIC/ICPSEUROPE49358.2020.9160517.

- Ciocia, A.; Di Leo, P.; Malgaroli, G.; Russo, A.; Spertino, F.; Tzanova, S. Innovative Teaching on Photovoltaic Generation. *11th National Conference with International Participation,*

ELECTRONICA 2020 – Proceedings **2020**, doi:10.1109/ELECTRONICA50406.2020.9305110.

- Ciocia, A.; Di Leo, P.; Fichera, S.; Malgaroli, G.; Russo, A.; Spertino, F.; Tzanova, S.; Dalanbayar, B. Innovative Laboratories for Teaching on Photovoltaic Generation in Higher Education. *2020 29th International Scientific Conference Electronics, ET 2020 - Proceedings* **2020**, doi:10.1109/ET50336.2020.9238310.

- Amato, A.; Heiba, B.; Spertino, F.; Malgaroli, G.; Ciocia, A.; Yahya, A.M.; Mahmoud, A.K. An Innovative Method to Evaluate the Real Performance of Wind Turbines With Respect to the Manufacturer Power Curve: Case Study from Mauritania. *21st IEEE International Conference on Environment and Electrical Engineering and 2021 5th IEEE Industrial and Commercial Power System Europe, EEEIC / I and CPS Europe 2021 - Proceedings* **2021**, doi:10.1109/EEEIC/ICPSEUROPE51590.2021.9584790.

- Astolfi, D.; Malgaroli, G.; Spertino, F.; Amato, A.; Lombardi, A.; Terzi, L. Long Term Wind Turbine Performance Analysis Through SCADA Data: A Case Study. *6th International Forum on Research and Technology for Society and Industry, RTSI 2021 - Proceedings* **2021**, 7–12, doi:10.1109/RTSI50628.2021.9597326.

- Spertino, F.; Chiodo, E.; Ciocia, A.; Malgaroli, G.; Ratclif, A. Maintenance Activity, Reliability, Availability, and Related Energy Losses in Ten Operating Photovoltaic Systems up to 1.8 MW. *IEEE Transactions on Industry Applications* **2021**, *57*, 83–93, doi:10.1109/TIA.2020.3031547.

- Ciocia, A.; Amato, A.; Di Leo, P.; Fichera, S.; Malgaroli, G.; Spertino, F.; Tzanova, S. Self-Consumption and Self-Sufficiency in Photovoltaic Systems: Effect of Grid Limitation and Storage Installation. *Energies (Basel)* **2021**, *14*, doi:10.3390/en14061591.

- Spertino, F.; Amato, A.; Casali, G.; Ciocia, A.; Malgaroli, G. Reliability Analysis and Repair Activity for the Components of 350 KW Inverters in a Large Scale Grid-Connected Photovoltaic System. *Electronics (Basel)* **2021**, *10*, doi:10.3390/electronics10050564.

- Carullo, A.; Ciocia, A.; Malgaroli, G.; Spertino, F. An Innovative Correction Method of Wind Speed for Efficiency Evaluation of Wind Turbines. *ACTA IMEKO* **2021**, *10*, 46–53, doi:10.21014/ACTA_IMEKO.V10I2.1037.

- Antonetto, G.; Morciano, M.; Alberghini, M.; Malgaroli, G.; Ciocia, A.; Bergamasco, L.; Spertino, F.; Fasano, M. Synergistic Freshwater and Electricity Production Using Passive Membrane Distillation and Waste Heat Recovered from Camouflaged Photovoltaic Modules. *Journal of Cleaner Production* **2021**, *318*, 128464, doi:10.1016/J.JCLEPRO.2021.128464.
- Spertino, F.; Malgaroli, G.; Amato, A.; Qureshi, A.E.M.; Ciocia, A.; Siddiqi, H. An Innovative Technique for Energy Assessment of a Highly Efficient Photovoltaic Module. Solar 2022, Vol. 2, Pages 321-333 2022, 2, 321–333, doi:10.3390/SOLAR2020018.